8-23-2016

Synthesis and Optimization of Mesoporous Materials Using Sol-gel Based Inverse Micelle Method for Catalysis and Adsorption

Ting Jiang
tingjiangche@gmail.com

ABSTRACT

Synthesis and Optimization of Mesoporous Materials Using Sol-gel Based Inverse Micelle Method for Catalysis and Adsorption

Ting Jiang, PhD

University of Connecticut, 2016

Mesoporous materials have been widely used in redesigning commercially important processes for environmental and economic considerations. They have demonstrated great advantages in providing well-controlled surface area, pore size and volume, and nanocrystalline walls. Compared with microporous materials, they present improvement in molecular mass transfer, thus allowing larger reactant molecules involved in the reaction systems. This study focuses on the synthesis of University of Connecticut (UCT) mesoporous materials by the state-of-the-art sol-gel based inversed micelle method. Modification and optimization of the catalyst structural properties, such as surface area, pore size and volume, crystallinity, and phase were achieved by tuning the synthesis conditions, such as heating rate, calcination temperature and atmosphere, and dopant amount. The synthesized mesoporous materials have been applied as catalysts, catalyst supports, and adsorbents in several catalysis and adsorption processes. Particularly, (1) mesoporous iron oxides of different phases were synthesized as Fenton catalysts in orange II degradation in the presence of oxidant H_2O_2 at a neutral pH under visible light; (2) magnetic mesoporous iron oxide supports were developed for synthesizing magnetically recyclable palladium incorporated catalysts in nitrobenzene hydrogenation under mild conditions; (3) mesoporous aluminosilicates were fabricated and optimized as effective adsorbents for siloxane removal from biogas derived from anaerobic digestion of sludge. Overall, the mesoporous materials have satisfied the specific

purposes of different projects involved in this study, with adjustable structure, excellent catalytic activity/adsorption capacity, and good recyclability and stability.

Doctor of Philosophy Dissertation

Synthesis and Optimization of Mesoporous Materials Using Sol-gel Based Inverse Micelle Method for Catalysis and Adsorption

Ting Jiang

B.Sc, Dalian University of Technology, 2011

A Dissertation

Submitted in Partial Fulfillment of the

Requirements for the Degree of

Doctor of Philosophy

at the

University of Connecticut

2016

APPROVAL PAGE

Doctor of Philosophy Dissertation

Synthesis and Optimization of Mesoporous Materials Using Sol-gel Based Inverse Micelle Method for Catalysis and Adsorption

Presented by

Ting Jiang, B.S.

Major Advisor _____
Steven L. Suib

Associate Advisor _____
Yu Lei

Associate Advisor _____
Mu-Ping Nieh

Associate Advisor _____
Luyi Sun

Associate Advisor _____
Kelly A. Burke

University of Connecticut
2016

Dedicated to my husband, Shoucheng Du

ACKNOWLEDGMENTS

First of all, I would like to thank my parents for their strong support so that I can pursue a PhD degree in the U.S. Moreover, I would like to give a million thanks to my husband, Shoucheng Du, who always stands behind me, and supports me whenever I need help. Furthermore, I would like to show my greatest appreciation to Dr. Steven Suib who offered me the opportunity to study at UConn and pursue my PhD degree in a research field that I am interested in. I also want to thank him for guiding me in research with suggestions and encouragement. I'm so glad to see the growth of myself on the way towards a good researcher under his guidance. I would like to thank Dr. Steven O. Hay, Dr. Yu Lei, Dr. Mu-ping Nieh, Dr. Luyi Sun, and Dr. Kelly Burke for not only serving on the defense committee but also having provided me with lots of help in research. I'm grateful to the senior students, Dr. Aparna Iyer and Dr. Altug Poyraz, for their patient discussions and answering my questions during my first year in the group. I also want to thank Dr. Yashan Zhang, Dr. Zhu Luo, Wei Zhong, Tahereh Jafari, Junkai He as well as other group members for help in daily life and collaboration in research. Thanks to the technicians and the analytical lab staff in Department of Chemistry and Institute of Material Science for the technical support and training on the instruments. With the help of everyone mentioned, I had a wonderful and fruitful experience at UConn.

This work is supported by U.S. Department of Energy and Fraunhofer U.S.A.

TABLE OF CONTENTS

LIST OF FIGURES

LIST OF TABLES

1. INTRODUCTION

1.1 Mesoporous materials

Porous materials have been intensively studied with regard to technical applications as catalysts, catalyst supports, and adsorbents. According to the IUPAC definition, porous materials are divided into three categories: microporous (pore size <2 nm), mesoporous (2–50 nm), and macroporous (>50 nm) materials [1]. The schematic diagram, electron microscopy images, and typical applications of microporous, mesoporous, and macroporous materials are shown in Figure 1. Microporous materials, such as zeolites, have been widely used in chemical industry. However, the application of microporous materials is limited by the small pore size of the material. The mesoporous materials, such as MCM-41 and SBA-15 have huge surface areas (normally ≥1000 m^2/g), large pore sizes (2 nm ≤ size ≤ 20 nm), and ordered arrays of cylindrical mesopores with very regular pore morphology. The large surface areas of these materials increase the probability that a reactant molecule in solution/gas phase contacts the catalyst surface and reacts. The large pore size and ordered pore morphology allow the relatively large reactant/product molecules to diffuse into/out of the pores. Moreover, the mesoporous materials are thermally and chemically stable, which is preferred by industrial applications.

The advantages of mesoporous materials are summarized as follows:

(a) Mesoporous materials have highly ordered and controllable size which enable the size-selective adsorption of small molecules but the size-exclusion of larger molecules, providing molecular weight cutoff in sample enrichment [1].

(b) Mesoporous materials have high surface areas and large pore volumes which provide sufficient capacity for the adsorption of reactants.

(c) The framework of mesoporous materials can be various oxides, including silica, alumina, or transition metal oxides [2]. The transition metal oxides are particularly important among non-silica mesoporous materials because they possess d-shell electrons confined to nanosized walls, redox active internal surfaces, and connected pore network [3].

(d) Mesoporous materials are thermally stable, chemically stable, biocompatibility and have low toxicity.

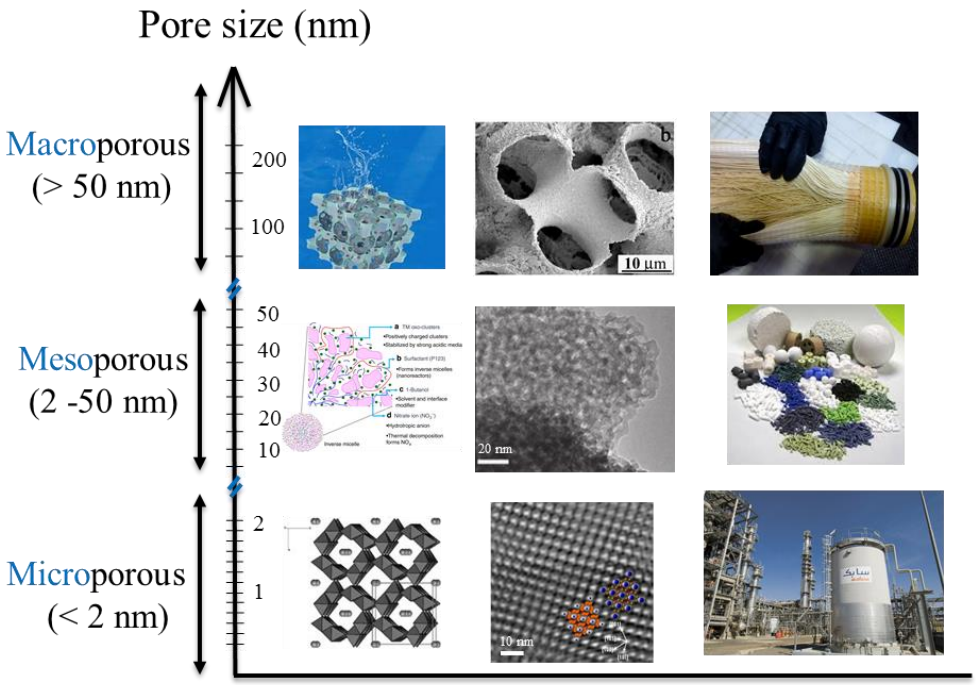

Figure 1: Schematic diagram, electron microscopy images, and applications of microporous, mesoporous and macroporous materials. (Reprinted by permission from Macmillan Publishers Ltd: Nature Communication (ref [3]), copyright (2013); reprinted by permission from Nature Publishing Group (ref [4]), copyright (2015); reprinted with permission from ref [5], copyright (2008) American Chemical Society; reprinted with permission from ref [6], copyright (2015) American Chemical Society; reproduced from ref [7] with permission of The Royal Society of Chemistry.)

1.2 General synthesis approaches of mesoporous materials

Recently mesoporous transition metal oxides have attracted a lot of attention because they have *d*-shell electrons and reactive redox internal surface. Generally, the approaches to synthesize mesoporous transition metal oxide can be classified into two methods: the hard template method and the soft template method. In the hard template method, mesoporous silica based materials, such as MCM-41, MCM-48, SBA-15, SBA-16, KIT-6, FDU-12, are used as templates. The fabrication process includes reinforced crystallization, post-synthesis solid-solid conversion, and/or nanocasting [8]. The inorganic precursor is firstly filled in the pores of the hard template, and then it is converted to inorganic solid network. After the network is formed, the hard template is removed. The obtained material is actually a replica of the hard template. The disadvantage of the hard template method is that the template is difficult to remove. In the soft template method, surfactants are used as templates. This fabrication process is an evaporation induced self-assembly process. The inorganic precursor and the surfactant are firstly mixed, forming a wet gel in the solvent. Then a mesoporous network is formed from the inorganic precursor. After that, the surfactant is removed by calcination or solvent extraction.

1.3 Sol-gel process

The sol-gel process is generally classified as a soft template method. During the sol-gel process, an oxide network is formed through poly-condensation of inorganic precursors in the liquid. Depending on the synthesis procedure, the morphology of the material synthesized by sol-gel process varies (Figure 2). In this study, powder form (dense ceramic) mesoporous materials were synthesized through the steps of hydrolysis, condensation, gelation, evaporation and heating. Usually in the sol-gel process, micelles, which have hydrophobic tails of surfactants inside and

hydrophilic tails of surfactants outside, are formed in water medium, usually resulting in metal oxide materials of amorphous wall structure and disordered pore system. In order to obtain crystalline wall and monomodal pore size distribution, inverse micelles, which have hydrophobic tails of surfactants outside and hydrophilic tails of surfactants inside and form in organic solvent medium, were adopted in this study. Explanations of reasons of using inverse micelles in the sol-gel process are explained in details in Section 1.4.

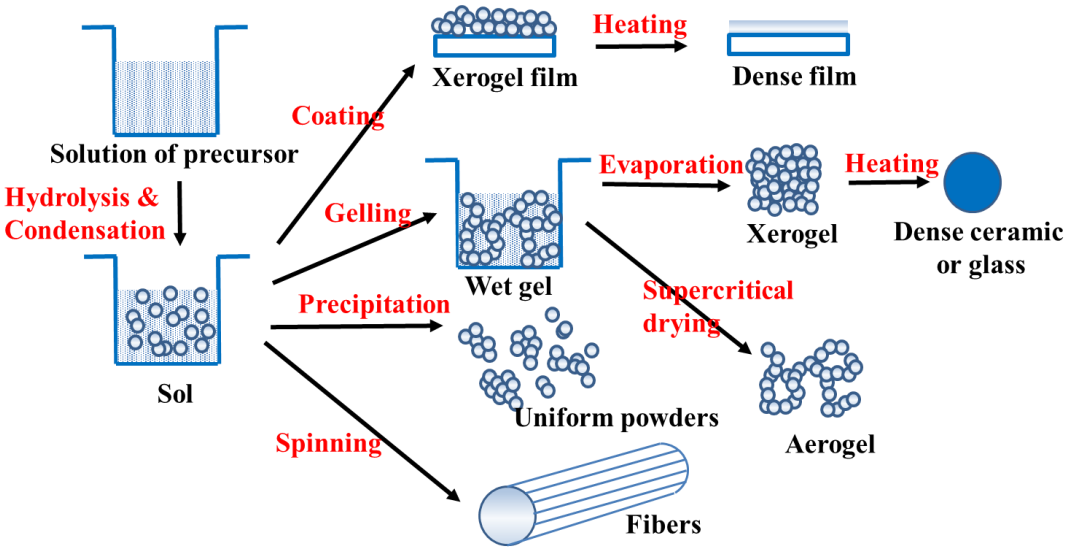

Figure 2: Various steps in the sol-gel process to control the final morphology of materials. (Reproduced from book Metal Oxide Nanoparticles in Organic Solvents: Synthesis, Formation, chapter 2 Aqueous and Nonaqueous Sol-Gel Chemistry, 2009, page 10, with permission of Springer" (ref [9])).

1.4 Interaction between surfactant and inorganic precursor in the solution

The interaction between surfactants and inorganic precursors is very important in the sol-gel synthesis of mesoporous materials. The possible interactions are listed in Figure 3, ranked from the strongest interaction to the weakest. In the columbic interaction, the charged surfactant is able to disperse the inorganic precursor very well into the solution. However, the strong interaction

between inorganic precursors and the surfactants will affect the condensation of inorganic precursor during the sol-gel transition step, resulting in the thin wall or amorphous wall structure of the obtained materials. The inorganic precursors and the surfactants can also interact through covalent bonding when strong Lewis acid center exists in the inorganic precursor. Besides these interactions, the electrons of oxygen of the surfactant can be transferred to empty orbitals of transition metals, forming another type of interaction. But this charge transfer can be easily destroyed by moisture through another stronger charge transfer between the oxygen of water and the inorganic precursor. The weakest interaction between inorganic precursors and the surfactants is hydrogen bonding.

Interaction type	Interaction form	Pros	Cons
Coulombic interaction	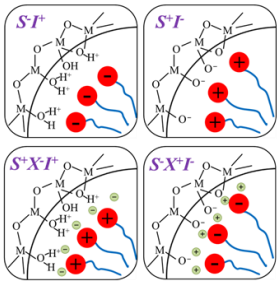	Strong S-I interaction, water-based solvent	Thin and amorphous inorganic wall and low thermal stability
Covalent bonding		Moisture resistive strong S-I interaction, controlled condensation of TM	Limited to strong Lewis acid center, low thermal stability
Charge transfer	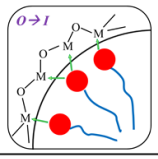	Thick (>2 nm), thermally stable, crystalline walls, and controlled mesostructure	Sensitive to water content, requires controlled evaporation of solvent
Hydrogen bonding	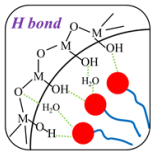	Water tolerant, thermally stable, and crystalline mesostructured	Relatively a weak interaction

Figure 3: The interactions between inorganic precursor (I) and surfactants (S) in the solution. (Reproduced from book Perovskites and Related Mixed Oxides: Concepts and Applications, chapter 31, Wiley-VCH (ref [10]); reproduced from book Nanoscale Materials in Chemistry, chapter 9, Wiley (ref [11]))

In this study, the weak interaction of hydrogen bonding is preferred, because this weak hydrogen bonding will not hinder the condensation of the inorganic precursor, and thus promote the formation of crystalline wall structure and well-controlled pore distribution. The advantages of the weak hydrogen bonding also include its water tolerance feature during the synthesis process and the thermal stability and crystallinity of the resulting mesostructured materials. Crystalline hydrates are usually used as the inorganic precursors. The schematic diagram of interaction between inorganic precursors and surfactants through hydrogen bonding is shown in Figure 3.

1.5 General procedure of sol-gel based inverse micelle method

Generally, the sol-gel based inverse micelle method includes three steps, the solution step, the sol-gel transition step, and the post synthesis step (Figure 4). In the solution step, the inorganic precursor solution is formed. The type of the inorganic precursors, dopant amount, surfactant properties (such as size, type, mixing ratio), and small additional molecules can be used to tune different properties of mesoporous materials. In the sol-gel transition step, the solvent starts evaporating, and then the micelles come together. When the solvent is totally dried, the inorganic precursors change into oxide and then oxide network. In this process, reaction temperature, reaction time, and the solvent are key factors that affect the properties of mesoporous materials. In the post synthesis step, the surfactant is first extracted by the solvent. Then the byproducts generated during the sol-gel transition step, such as NO_x and carboxyl groups, are removed by calcination at 150 °C. During post synthesis, calcination temperature, heating rate, and atmosphere can be adjusted for tuning the properties of mesoporous materials. Further modification, such as

sulfurization, reduction, and oxidation allow the generation of mesoporous metal sulfides, metal oxide with mixed valence, and metal oxide with different phases.

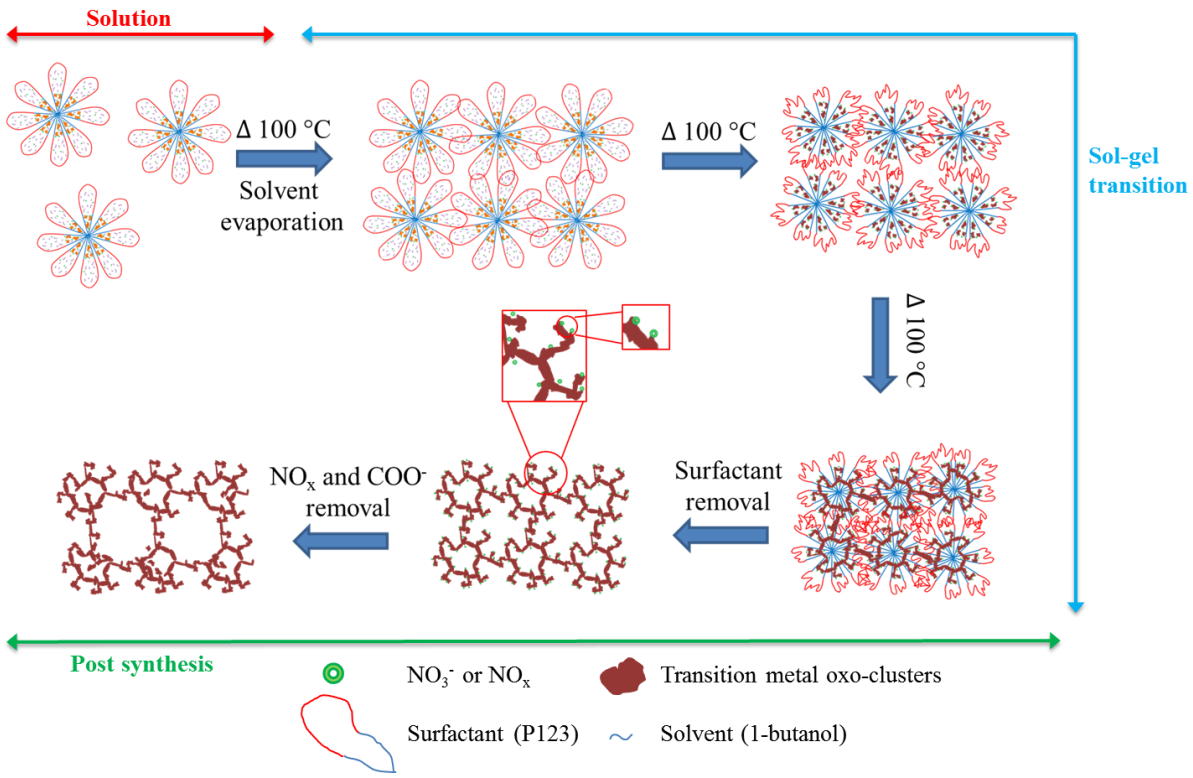

Figure 4: General procedure of sol-gel based inverse micelle method. (Reprinted by permission from Macmillan Publishers Ltd: Nature Communication (ref [3])).

1.6 Characteristics of sol-gel based inverse micelle method

There are three major characteristics of the sol-gel based inverse micelle method used in this study. The first one is the use of non-ionic surfactant P123. The non-ionic property of P123 allows the formation of hydrogen bond in the solution (Figure 5 (a)) and easy removal of the soft template. The oxygens on the hydrophilic tails of P123 are the bonding sites to inorganic precursors. So the length of hydrophilic tails of the surfactant decides the wall thickness of the as-made materials, and the length of hydrophobic tails of the surfactant decides the pore size of the as-made materials.

The second characteristic is the NO_x chemistry. The addition of nitric acid into the solution helps dissolve the inorganic precursors. In the sol-gel transition step, nitric acid decomposes to NO_x upon heating (NO_x detection by UV-Vis spectroscopy is shown in Figure 5 (b)), which quickly increases the pH of the solution thus preserves the as-made oxide materials. The pH adjustment helps stabilize the synthesized mesoporous metal oxide materials. The third characteristic is the use of organic solvent, 1-butanol. The non-polar property of organic solvent allows the formation of inverse micelle, which leads to the formation of interconnected inorganic oxide network. The interconnected mesoporous network has been proved by successful synthesis of mesoporous carbon out of the mesoporous silica template (Figure 5 (c)). The obtained mesoporous silica was used as a hard template for synthesis of mesoporous carbon and the pores of mesoporous silica were filled with the surfactant. After pyrolysis, the surfactant transformed into carbon left in the pores of mesoporous silica. After removal of mesoporous silica template, the carbon was identified as the mesoporous carbon, showing that the parent mesoporous silica template had the interconnected mesoporous network.

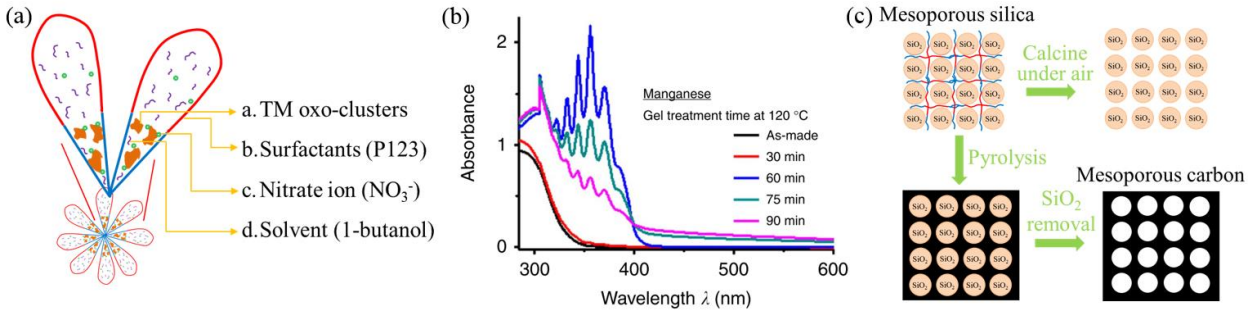

Figure 5: Explanation and proof of three characteristics of sol-gel based inverse micelle method (Reprinted by permission from Macmillan Publishers Ltd: Nature Communication (ref [3])).

1.7 Targeted applications of mesoporous materials

In recent years, environmental and economic considerations have raised strong interest to redesign commercially important processes so that the use of harmful substances and the generation of toxic waste could be avoided [12]. In this respect, there is no doubt that heterogeneous catalysis can play a key role in the development of environmentally benign processes, such as petroleum industry, production of chemicals, treatment of waste, and development of clean energy (e.g. biogas, hydrogen). Microporous materials have attracted strong attention as acids, bases, and redox catalysts. However, they present severe limitations when large reactant molecules are involved, especially in liquid-phase systems, as is frequently the case in the synthesis of fine chemicals, due to the fact that mass transfer limitations are very severe. Attempts to improve the diffusion of reactants to the catalytic sites have focused on increasing the pore sizes or providing an additional mesopore system within the microporous materials while preserving the acidic/basic or redox properties of the materials. In the following context, the background, current research status and challenges of catalysis and adsorption processes, nitrobenzene hydrogenation, dye degradation, water splitting, and siloxane adsorption, are introduced and reviewed. The preliminary work was to investigate the effectiveness of utilizing mesoporous materials in catalysis and adsorption.

1.7.1 *Photocatalytic dye degradation*

Increasing environmental concerns have been aroused by one of the largest groups of organic compounds, industrial dyes [13]. Among the industrial dyes, azo dyes (-N=N- group specified) constitute a large percentage [14]. The complete removal of the azo dyes from wastewater is necessary due to their properties of being carcinogenic, harmful, and non-biodegradable. Thus, the investigation of methods for azo dyes removal has been a hot subject with widespread research

[14,15]. There are many ways for dye removal from wastewater, such as physical-chemical methods, chemical methods, advanced oxidation processes (AOPs), and electrochemical methods [15]. Among these methods, advanced oxidation processes mostly with the help of O_3, H_2O_2, and UV, have been proven to be very effective in degrading dyes [16]. In AOPs, photo-Fenton's process is very attractive for its effectiveness in decolonization and mineralization of dyes, low cost, and non-toxicity (i.e. Fe^{2+} and H_2O_2) [17]. In most cases, strong acids are added into wastewater to meet the pH requirement (pH=2-4) for the best performance of catalysts before the application of traditional Fenton reactions. In the photo-Fenton process, organic pollutants can be degraded effectively and non-selectively by reactive oxygen species such as hydroxyl radical (•OH) and hydroperoxyl radicals (•OOH/O_2^-). The mechanism of Fenton reagents in aqueous solutions is shown as follows [18]:

$$Fe^{2+}(aq) + H_2O_2\,(aq) \rightarrow\ Fe^{3+}(aq) + OH\bullet(aq) + OH^-(aq) \quad \text{(chain initiation)}$$

$$Fe^{3+}(aq) + H_2O_2\,(aq) \leftrightarrow Fe - OOH^{2+}(aq) + H^+(aq)$$

$$Fe - OOH^{2+}(aq) \rightarrow HO_2\bullet(aq) + Fe^{2+}(aq)$$

$$OH\bullet(aq) + Fe^{2+}\,(aq) \rightarrow\ OH^-(aq) + Fe^{3+}(aq) \quad \text{(chain termination)}$$

However, there are several drawbacks of the photo-Fenton and related processes which limit their effectiveness: 1) ultra-violet light, which only accounts for 2% of sunlight, is not as widely available as visible light; 2) acid reaction conditions, which have been proved to offer the best reaction conditions for Fenton catalysts [19,20], also needs further processing to avoid second-time contamination in the processing of wastewater treatment; 3) the large volume of Fe (III)-iron sludge after a Fenton reaction needs to be removed at the end of treatment by precipitation, which

causes additional expense of the wastewater treatment. Therefore, the development of active heterogeneous systems to enable the photo-Fenton reaction to operate with 1) visible light, 2) neutral or near-neutral pH conditions, and 3) no Fe ion sludge generation, is of great significance. So focus has been given to research in heterogeneous catalysis to allow the photo-Fenton process to work at the above-mentioned conditions without a tradeoff of efficiency.

For the Fenton process under visible light, significant contribution can be found from work in the literature [21–24]. However, most of the work is limited by acidic conditions[25–27]. This is because formation of the key oxidant •OH radicals can be accelerated under acid conditions (best at pH=2-4) in the Fenton reaction [18,21,28–30]. As an improvement, in the application of azo dye degradation, a few researchers have studied the catalyst performance under neutral or near neutral pH. Feng et al. [31] studied the effectiveness of 4 different catalysts on discoloration and mineralization of orange II at pH=3 and pH=6.6 conditions. They observed bentonite clay-based Fe nanocomposite was the catalyst with the best performance in both pH conditions. Specifically, at pH=3 conditions, Fe nanocomposite was able to degrade 90% of orange II within 10 min whereas at pH=6.6 condition Fe nanocomposite needed 30 min to degrade 90% of orange II. However, in the case above, an ultraviolet light source was used for the Fenton reaction. Other examples with both visible light and neutral pH come from Cheng et al. [32] and Du et al. [33]. Cheng et al. claimed that 90% of methyl orange was degraded by Fe(III)-loaded resin within 500 min at nearly a neutral pH condition (pH=6.0) in the presence of H_2O_2 under visible irradiation. Du et al. reported that clay-supported iron oxide was able to degrade 65% of anionic orange II in 150 min and > 90% of cationic dye methyl orange within 60 min at near neutral pH conditions (pH=6.5) under visible light and H_2O_2.

Mesoporous iron oxide is very promising in dye degradation. Because in the photo-Fenton process catalyzed by mesoporous iron oxides, diffusion can be promoted by large pore sizes and pore volumes and active sites can be provided by large surface areas at the same time. Kim et al. [34] synthesized mesoporous iron oxide-layered tinanate nanohybrids with pore sizes of 3.7 nm-12 nm. The prepared material can degrade 100% methylene blue within 120 min under visible light. Panda et al. [35] synthesized a mesoporous Fe_2O_3-SiO_2 composite by using CTAB as a structure directing agent. The mesoporous Fe_2O_3-SiO_2 composite is able to discolor 98.5% methyl orange within 20 min in the presence of H_2O_2. And after a 3-cycle experiment, the catalyst is very stable and only shows 1.5% loss of activity in discoloration and mineralization of methyl orange. In this study, we modified the sol-gel-based inverse micelle methods published before [3], and successfully synthesized mesoporous 2-line ferrihydrite (UCT-5), α-Fe_2O_3 (UCT-6), γ-Fe_2O_3 (UCT-64), and Fe_3O_4 (UCT-65), by changing the reaction temperature and calcination atmosphere. Various characterization techniques have been performed in order to understand the properties of synthesized materials. The synthesized mesoporous materials have been applied to azo dye (orange II) degradation in the presence of oxidant H_2O_2 at neutral pH under visible light. The possibility of recycling catalysts offered by this study serves a further advantage of using these catalysts for industrial applications.

1.7.2 *Nitrobenzene hydrogenation*

Aniline is an important precursor for the manufacture of polyurethane, indigo, and other industrial chemicals. The common industrial method for aniline production is through catalytic hydrogenation of nitrobenzene [36,37]. In the process, carbon supported noble metal catalysts are widely used [37–45]. However, improvement of the catalyst is limited by some obstacles. The first obstacle is attributed to the use of an inactive carbon support. Although active carbon provides a

high surface area, Pd cannot be anchored as efficiently as some basic supports, such as hydrotalcite [36]. Moreover, active carbon cannot act as effectively as basic supports (metal oxide support) to bond nitrobenzene strongly by a noble metal-support interface [46–48], which will promote the reaction rate of the catalytic hydrogenation reaction. The second obstacle exists when small pore size and pore volume catalyst supports are used, restricting the dispersion of Pd nanoparticles and diffusion of reactants [49–53]. The third obstacle is the difficulty of recycling the catalysts. Since the noble metal catalysts are very expensive, separation and recycling of the catalyst are desirable [54–59]. Magnetically separable catalysts are attractive heterogeneous catalysts due to their facile recycling process [60,61].

A great deal of effort has been put to overcome these obstacles in order to synthesize effective catalysts for the nitrobenzene hydrogenation reaction. Improvement of the carbon support has been studied in the literature. Torres et al. [62] found that carbon supports treated with ozone and hydrogen peroxide could reinforce noble metal dispersion and hydrogenation capacity, compared with untreated ones. This is because treated carbon supports, which have weak acid sites formed on the surface, have stronger interaction with the noble metal precursors. Bouchenafa-saib et al. [38] treated active carbon supports with H_3PO_4 and $ZnCl_2$ and oxidized them in air to generate surface oxygenated groups. The surface oxygenated groups, which are related to acidity, affected the turnover frequency of hydrogenation of nitrobenzene.

Utilization of mesoporous metal oxides as catalyst supports has also been investigated in literature. The use of mesoporous metal oxides as catalyst supports had two functions: one was to protect nanoparticles from aggregation and improve their thermal stability; the other was to enhance the catalytic activity by providing acid/base and redox sites or desired interfaces. Banerjee et al. [49] studied the immobilization of noble metals into mesoporous materials. They encapsulated Pd

nanoparticles into mesoporous MCM-48 matrix, which could catalyze hydrogenation reactions under aerobic conditions. The excellent activity of the catalyst was mostly due to their large surface area, better metal dispersion, and interpenetrating network of three dimensional pores of MCM-48. Liu et al. [52] dispersed bimetallic nanoparticles (PtPd/AuPd/AuPt) into mesoporous metal oxides (TiO_2/Al_2O_3/SiO_2/ZrO_2) by a one-step sol-gel method.

Moreover, researchers studied the nitrobenzene hydrogenation reaction over magnetically supported palladium catalysts. Yi et al. [56] synthesized silica-coated magnetic nanoparticles as the support for Pd nanoclusters. The synthesized catalysts could be easily recycled by an external magnet and reused at least 5 times with 100% conversion in nitrobenzene hydrogenation. Lang et al. [63] used Fe_3O_4/SiO_2 and Fe_3O_4/Al_2O_3 as a core to synthesize Pd supported catalysts. Magnetic alumina-supported palladium catalysts could achieve 90% conversion of nitrobenzene within 40 min reaction time with only 1% Pd loading.

Although the studies mentioned above focused on overcoming each obstacle in catalysis for nitrobenzene hydrogenation separately, a catalyst with properties that can improve (1) the functionality of the catalyst support, (2) the mesoporosity and porous network of the support, and (3) the recyclability of the catalyst are all still under exploration. In this study, synthesis of mesoporous γ-Fe_2O_3 supported Pd catalysts and their application in nitrobenzene hydrogenation are investigated, trying to overcome the three main obstacles discussed above at the same time. In particular, iron oxide support is proposed to act as a base which can adsorb nitrobenzene to initiate the first step of heterogeneous catalysis, adsorption. The aggregated maghemite nanoparticles exhibit superparamagnetic behavior, which enables easy recycling of the catalysts.

1.7.3 *Siloxane adsorption for biogas cleanup*

Biogas, a product from anaerobic decomposition of organic waste in landfill and sewage plants, is one of the promising renewable energy sources [64–68]. Production of biogas is one of the effective ways of converting waste to fuels and energy [69–71], which can reduce the use of fossil resources and usually mitigate greenhouse gas emissions [72]. However, biogas from sewage sludge and landfills contains trace siloxane impurities (e.g. octamethylcyclotetrasiloxane (D4), hexamethyldisiloxane (L2), and trimethylsilanol (TMS)) [73], which are converted into abrasive microcrystalline silica [74,75] during combustion in the engines. The buildup of the silica layers inhibit the essential heat conduction or lubrication [74,76]. Among these siloxane impurities, cyclic siloxane is very hard to remove because of lack of functional groups and large molecular size. Since the siloxane D4 is one of the major impurities in landfill gas and anaerobic digester gas [73], D4 was chosen as a model compound in this study. The untreated biogas may contain siloxanes of up to 2000 mg/m^3 [77], which is significantly higher than the manufacturer siloxane limit (15 mg/m^3) [74,78]. Thus, removal of siloxanes has been implemented in industrial processes [79,80]. Among them, adsorption of siloxanes by solid adsorbents is widely used because of its simplicity, excellent siloxane removal performance, possible high degree of regeneration, and the possibility of increased performance by multiple columns in parallel or new advanced adsorbents [79].

So far, a variety of adsorbents of high porosity and large surface area, such as active carbon [76,81–84], silica gel [77], zeolites [85,86], and molecular sieves [77,87], have been explored for the adsorption of siloxanes. Active carbon is the most commonly used adsorbent in industry. However, utilization of active carbon has the potential danger of starting adsorbent bed fires when high concentrations of organic compounds are treated [88]. In addition, regeneration of the used active

carbon by thermal treatment is difficult [76,77,89]. In contrast, zeolites offers possibility to be regenerated by hot air at relatively high temperatures, or through advanced oxidation by H_2O_2 with low risks of catching fire because of the inertia and stability of the zeolite structure [80,89].

Super microporous (pore size=7-20 Å) and mesoporous (pore size=20-500 Å) adsorbents have been found preferable for the adsorption of the relatively large-size siloxanes, such as D4 (~10 Å kinetic diameter) [75,86,90,91]. Yu et al. [75] investigated the effect of the main textural properties of adsorbents when siloxanes are removed. The adsorbents with pore sizes distributed around 17-30 Å have the largest adsorption capacity. A recent study by Cabrera-Codony et al. [76] further proved that the mesopore volume was related more to the D4 adsorption capacity than the larger micropore volume, and the narrow micropore volume (< 7 Å) did not correlate at all with the adsorbent capacity. Therefore, development of the adsorbents with a relatively large pore size (> 17 Å) for siloxane adsorption is imperative [92]. In this study, exploration of the mesoporous zeolite-type adsorbents in D4 adsorption has been performed. The main focus of this study is to first tune the textural properties of the adsorbents by changing the synthesis conditions [93,94], such as the aluminum dopant amounts and the calcination heating rate, and then investigate the effect of the textural properties of the adsorbents on siloxane adsorption performance. Moreover, the synthesized mesoporous aluminosilicates have been compared with the commercial ZSM-5 to evaluate the effectiveness of the new mesoporous aluminosilicates on D4 adsorption. Lastly, a mechanistic discussion regarding the key adsorbent textual properties that would affect the adsorption capacity, and the fate of D4 during the adsorption is presented.

1.8 Objective of this study

In this study, the mesoporous materials are synthesized by the state-of-the-art sol-gel reverse micelle method. The details regarding material synthesis, characterization and optimization are stated and discussed as a whole chapter. The main objective of this study is to improve the performance of the mesoporous materials in organic synthesis, photocatalysis, and adsorption by tuning the structure of the materials. This dissertation is particularly focused on (1) synthesis of mesoporous iron oxides with difference phases and their application in dye degradation; (2) synthesis of mesoporous and magnetically recyclable Pd/meso-γ-Fe_2O_3 nanoparticles for nitrobenzene hydrogenation; (3) synthesis of mesoporous aluminosilicates with different structural parameters for siloxane adsorption.

2. MATERIALS CHARACTERIZATION TECHNIQUES AND PERFORMANCE EVALUATION PROCEDURE

2.1 Characterization techniques

2.1.1 *X-ray diffraction*

Powder X-ray diffraction (PXRD) data were collected on a Rigaku UltimaIV instrument using Cu Kα (1.54 Å) radiation at a beam voltage of 40 kV and a 45 mA beam current. High-angle and low-angle patterns were obtained by continuous scans in a 2θ range of 5-90° and 0.5-5° with a scan rate of 2 °/min and 0.5 °/min, respectively. The peaks were indexed with the International Center for Diffraction Data (ICDD) PDF-2 database.

2.1.2 *Nitrogen sorption*

The surface area, pore size distribution, and pore volume of iron oxides were determined in a Micrometitics Accelerated Surface Area and Porosimetry (ASAP) 2020 System. The isotherms of N_2 at 77 K were obtained from physisorption. Before analysis, the samples were degassed at 120 °C under vacuum for 12 h to remove the surface contaminants. The pore size distributions of the iron oxides were determined from the N_2 desorption isotherms at 77 K, using the Barrett–Joyner–Halenda (BJH) method. Cumulative pore volume distribution was obtained using the density function theory (DFT) method. Brunauer-Emmett-Teller (BET) specific surface area was calculated by the adsorption isotherm with the points in the range of $0.05 < P/P_0 < 0.3$. Total pore volume was determined by the amount of N_2 adsorbed at $P/P_0 = 0.99$. Micropore volume (V_{micro}) was calculated by the Dubinin-Radushkevich (DR) method with the points in the range of $10^{-4} < P/P_0 < 0.1$. Mesopore volume (V_{meso}) was calculated by the Barrett-Joyner-Halenda (BJH) method

(BJH desorption cumulative volume of pores between 17 Å and 5000 Å). Average pore size was calculated from the adsorption branch of the isotherm. The external surface area was calculated by the t-plot method; the micropore surface area is obtained by subtracting the external surface area from the BET specific surface area.

2.1.3 *Electron microscopes*

High-resolution scanning electron microscope (HRSEM) photographs were taken on a Zeiss DSM 982 Gemini FESEM with a Schottky emitter at an accelerating voltage of 2.0 kV and a beam current of 1.0 mA. A high-resolution transmission electron microscope (HRTEM) was used to characterize the crystallized structure and the morphology of the samples using a JEOL 2010 instrument with an accelerating voltage of 200 kV. EDX spectra were acquired in the same JEOL 2010 instrument as well.

2.1.4 *X-ray photoelectron spectroscopy*

X-ray photoelectron spectroscopy (XPS) was used to determine the surface properties of catalysts in a PHI 590 spectrometer with multiprobes (ΦPhysical Electronics Industries Inc.), using Al Kα radiation (λ = 1486.6 eV) as the radiation source. The powder samples were pressed on carbon tape. The carbon tape and sample stage was stuck together by double-sided adhesive copper tape before the sample stage is placed in the analysis chamber.

2.1.5 *Infrared spectroscopy*

Diffuse Reflectance Infrared Fourier Transform Spectroscopy (DRIFTS) of the mesoporous iron oxides after adsorption of dye was performed in a NICOLET 6700 Fourier Transform Infrared Spectroscopy (FTIR) from Thermo Scientific, equipped with an MCT detector and a Praying

Mantis DRIFTS cell from Harrick Scientific. Pure potassium bromide (KBr) was used as background and samples were diluted in KBr (0.5 wt% concentration) for each analysis.

2.1.6 *Raman spectroscopy*

Raman spectra were obtained using a Renishaw 2000 Ramanscope which has an optical microscope (0.024 inches focus length), graphic grating (1800 mm^{-1}), and CCD detector. A laser excitation source with 514 nm wavelength was used for testing mesoporous α-Fe_2O_3, γ-Fe_2O_3, and Fe_3O_4; a laser excitation source with 633 nm was used for testing mesoporous 2-line ferrihydrite. The laser focus was set to 40% to prevent local damage [67,95,96]. For each sample, 3 different locations were analyzed to verify the spectra.

2.1.7 *X-ray absorption spectroscopic*

The X-ray absorption spectroscopic (XAS) measurements were conducted at the National Synchrotron Light Source (NSLS) at Brookhaven National Laboratory using beamline X18A. The synchrotron radiation was monochromatized by a Silicon (111) double crystal monochromator. The incident and transmitted beam intensities were monitored using ionization chambers filled with mixtures of He and N_2 gases. The samples were diluted by h-BN with a ratio of (1:8), then pressed into pellets, and mounted between the ionization chambers of Io and It. A thin iron foil reference was used for energy calibration. The XANES data were analyzed using Athena software where background and post and pre-edge corrections were made.

2.1.8 *Thermogravimetric analysis–mass spectrometry*

Thermogravimetric analysis–mass spectrometry (TG-MS) analyses were performed with a TG 209 F1 Libra thermogravimetric analyzer coupled to a QMS 403C quadrupole mass spectrometer. The

samples (20 mg) were kept at 120 °C to removal adsorbed water and then heated to 600 °C with a 5 °C/min heating rate under 20 mL/min argon. A scanned bargraph mode was used for MS measurements.

2.1.9 *Measurement of magnetization*

Measurement of the dc magnetization were carried out for -50 kOe ≤ H ≤ +50 kOe at a temperature T=300 K using a Quantum Design MPMS-5 superconducting quantum interference device (SQUID) magnetometer. DC magnetic measurements were also carried out as a function of applied magnetic field (-10 kOe to 10 kOe at 300 K) with a vibrating sample magnetometer attached to the Evercool Physical Property Measurement System (PPMS) from Quantum Design.

2.2 Dye degradation

For the dye adsorption experiment, typically, 50 mg of iron oxide and 200 mL of 0.1 mM aqueous orange II solution at various initial concentrations C_0 was mixed in a beaker, followed by stirring at a constant rate in the dark overnight. After equilibrium was reached, the suspension was filtered through a micro filter with a 0.45 μm PVDF membrane (Pall Corporation), and the substrate Ce concentration remaining in the filtrate was analyzed. The decreased concentration (C_0-C_e) was then used to calculate the amount of adsorption, in units of milligrams per gram of iron oxide.

For dye degradation reaction, dye solutions (0.1 mM) were prepared by dissolving relative amounts of dyes into DDW. Before the degradation reaction, dye solution and catalysts (0.25 g/L) were stirred vigorously in the dark overnight to eliminate the adsorption effect to reach equilibrium. Then the degradation reaction was started by adding H_2O_2 solution to the suspension (to reach 12.5 mM concentration in solution) under visible light irradiation in a 600 mL quartz beaker as the photoreactor. The pH of solution was the intrinsic pH and no more addictive was added to adjust

the pH value. The solution was stirred by a magnetic stir bar. All the catalysts were suspended in the solution during the dye degradation reactions. The beaker was covered with a watch glass to minimize water evaporation and interference from the atmosphere.

2.3 Nitrobenzene hydrogenation

Solvent ethanol (25 mL) with 25 mg catalyst was bubbled in an inert gas atmosphere (30 mL/min nitrogen) for 1 hour to create an inert gas atmosphere. Then the suspension was purged with 30 mL/min hydrogen for 0.5 hour at 50 °C under reflux for *in-situ* reduction of catalysts. When the catalyst was ready, nitrobenzene (2.5 mmol) was injected into the solution to start the reaction. During the reaction, the vessel was kept at 50 °C and 1 atm under reflux, very mild conditions as compared with those in the literature [38,53,97–99]. Samples were taken every 20 min to analyze the conversion of nitrobenzene and concentration of reaction intermediates and products. All the samples were filtered with a 0.45 μm-PVDF syringe filter (Pall Corporation) and then analyzed as a function of time with an Agilent 7820A gas chromatograph with a 5975 MS detector (GC/MS system).

2.4 Siloxane adsorption

The D4 adsorption experiments were performed under dry conditions. During the experiments, nitrogen of 5 mL/min was used as the carrier gas. The carrier gas first passed through a bubbler with 10 mL D4 which is maintained at 25 °C in an oil bath, and then passed through adsorbents (100 mg, around 1 cm long in a quartz tube). The average siloxane concentration of 2000 mg/m^3, higher than the real industrial situation (50-500 mg/m^3) and the highest previously reported in the literature [77], was used in this study. The D4 that broke through the adsorbents was trapped by hexane in an ice bath. Samples were taken from the hexane trap regularly and analyzed by Agilent

7820A gas chromatography with a 5975 MS detector (GC-MS) to monitor the siloxane concentration. The GC-MS was calibrated with different concentrations of D4 for quantitative analyses. The D5 of 10 μL was used as an internal standard for verification of the results. GC is equipped with a 12-meter-long HP-1 column. The temperature of the oven in GC is first kept at 40 °C for 2 min, then increased to 250 °C with a 15 °C/min ramp rate, and finally kept at 250 °C for 5 min. The detection limit of GC is 1 ppm. The amount of D4 adsorbed was calculated by subtracting the D4 amount in the trap during the experiment from the D4 amount in the trap during the blank experiment under the same conditions. Each experiment was repeated at least three times and the error bars are shown in the plots. The capacities of the adsorbents were determined by the saturation points from the D4 adsorption curves. The adsorbents with adsorbed D4 were soaked and washed with hexane more than three times until no more siloxanes were removable from the adsorbents. Then the extracted siloxanes in hexane were analyzed to study the surface polymerization reactions during the adsorption. The polymerization ratio was calculated as the total amount of extracted D5, D6, and D7 over the amount of extracted D4 [76].

3. SYNTHESIS, OPTIMIZATION, AND CHARACTERIZATION OF MESOPOROUS MATERIALS

3.1 General synthesis method

A general approach, developed by A.S. Poyraz et al. [3], has been used to synthesis mesoporous materials in this study. This method is called sol-gel-based inverse micelle method, where the inversed micelles formed by surfactant species serve as nanoreactors. Acid media is used to stabilize the inorganic oxo-clusters and 1-butanol is used as interface modifier to hinder the condensation of the precursors. After forming the inverse micelle, the inorganic component is condensed and oxidized by evaporating the solvent. Then the surfactants are removed by ethanol washing. After that, the adsorbed species (NO_x and COO^-) are removed by further heat treatment.

3.2 Mesoporous iron oxides with different phases

3.2.1 *Synthesis procedure*

Iron nitrate of 0.01 mol was dissolved in a solution containing 0.12 mol 1-butanol, 0.019 mol nitric acid and 2.04×10^{-4} mol P123 in a 150 mL beaker at room temperature with magnetic stirring [3]. Then the clear gel was put in the oven under air at 95 °C for 2-3 hours to synthesize mesoporous 2-line ferrihydrite and mesoporous α-Fe_2O_3. The clear gel was placed in the oven at 100 °C under air to synthesize mesoporous γ-Fe_2O_3 and Fe_3O_4. The obtained powders were washed twice with ethanol and then centrifuged. Finally, the powders were dried in a vacuum oven overnight. To synthesize mesoporous 2-line ferrihydrite and γ-Fe_2O_3, the dried powders (as-made samples) were heated at 150 °C for 12 hours and then heated at 250 °C for 4 hours under air atmosphere. To synthesize mesoporous α-Fe_2O_3, the dried powders were heated at 150 °C for 12 hours, and then

heated at 250 °C for 4 hours, then finally heated at 350 °C for 3 hours under an air atmosphere. To synthesize mesoporous Fe_3O_4, the dried powders were heated at 150 °C for 12 hours and then heated at 250 °C for 4 hours under a nitrogen atmosphere. The different parameters which were used in the synthesis method are summarized in Table 1. The synthesis processes of each phase of iron oxide were repeated at least five times for accuracy and repeatability.

Table 1: Experimental parameters for various mesoporous iron oxides.

	Reaction temperature	Heating cycles	Heating atmosphere
2-line ferrihydrite	95°C	150°C (12h) - 250°C (4h)	Air
α-Fe_2O_3 (Hematite)	95°C	150°C (12h) - 250°C (4h) - 350°C (3h)	Air
γ-Fe_2O_3 (Maghemite)	100°C	150°C (12h) - 250°C (4h)	Air
Fe_3O_4 (Magnetite)	100°C	150°C (12h) - 250°C (4h)	Nitrogen

3.2.2 *Characterization*

High-angle PXRD is used to identify phases and crystallinity of the synthesized iron oxides samples (Figure 6 (a)). PXRD patterns of mesoporous α-Fe_2O_3, γ-Fe_2O_3, and Fe_3O_4 match with standard PDF cards of hematite (33-0664), maghemite (39-1346), and magnetite (19-0629) respectively. In comparison with the literature, XRD patterns of α-Fe_2O_3, γ-Fe_2O_3, and Fe_3O_4 show low peak intensities. This indicates low crystallinity of these samples. The PXRD pattern of 2-line ferrihydrite (Fe_2O_3•$n$$H_2O$) contains two peaks of low intensity appearing at *d*-spacings of 2.53Å (35.4°) and 1.47Å (63.0°), which match patterns of 2-line ferrihydrite very well in the literature [100]. For ferrihydrite, a range of compounds with different degrees of structural order exist; these compounds are generally named according to the number of broad X-ray peaks which they exhibit:

e.g. 2-line and 6-line ferrihydrite [101]. The formula of ferrihydrite has not been fully established [101]. $Fe_5HO_8 \cdot 4H_2O$ and $5Fe_2O_3 \cdot 9H_2O$ have been suggested, but the amounts of structural water may in fact be less than those indicated in these formulas [101,102]. It was difficult to obtain the actual formula of 2-line ferrihydrite in this study. As shown in the TG-MS plot (Figure 30 (a) and (f), the weight loss takes place at 150 °C and 300 °C, caused by losing both H_2O and CO_2. The temperature of releasing H_2O overlaps with that of losing CO_2, which makes the attempt to calculate the formula of 2-line ferrihydrite unsuccessful. The crystallinity of mesoporous α-Fe_2O_3 was obtained by further heating mesoporous 2-line ferrihydrite at 350 °C. Recent studies from our group [3] found that transition metal oxides are amorphous when calcined at a low temperature while they become crystalline with different phases when calcined at a higher temperature. Patterns of γ-Fe_2O_3 and Fe_3O_4 only show differences below 30°. Both γ-Fe_2O_3 and Fe_3O_4 are inverse spinel structures and the differences between the crystal structures of them are the iron valence and the vacancies. Fe_3O_4 can be formulated as $(Fe^{III})_A[Fe^{II}Fe^{III}]_BO_4$ and γ-Fe_2O_3 can be formulated as $(Fe^{III}_8)_A[Fe^{III}_{40/3}\square_{8/3}]_BO_{32}$, where A represents tetrahedral sites and B represents octahedral sites.

Figure 6 (b) shows the low-angle diffraction lines for mesoporous iron oxide samples. The low-angle diffraction line position is 1.35° (6.5 nm) for 2-line ferrihydrite. Since mesoporous α-Fe_2O_3 was obtained by further heating 2-line ferrihydrite to 350 °C, the shift of low-angle diffraction peak positions of mesoporous α-Fe_2O_3 to 0.94° (9.4 nm) is attributed to the sintering nature of small crystalline nanosize particles [3]. Mesoporous γ-Fe_2O_3 has a similar low-angle diffraction line position to 2-line ferrihydrite which is at 1.35° (6.5 nm). The meso-structures (low-angle diffraction line) of mesoporous 2-line ferrihydrite, α-Fe_2O_3, and γ-Fe_2O_3 are all very clear. In case of Fe_3O_4, we can only see a shoulder because the position of the line, 0.58° (15.2 nm) is too low

to get the full peak. The mesoporous structures of the iron oxides are further confirmed by nitrogen sorption.

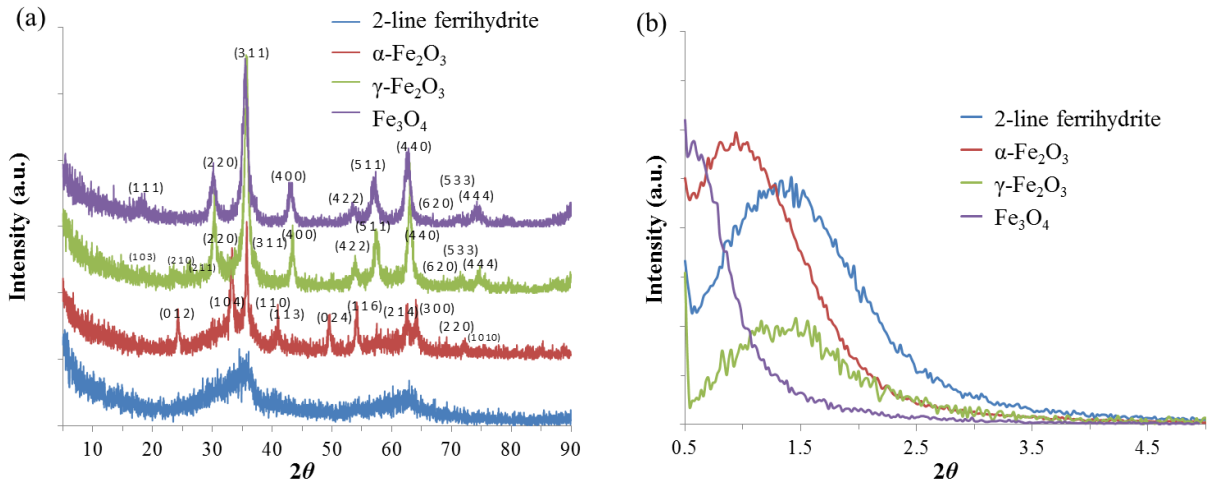

Figure 6: (a) High-angle and (b) low-angle PXRD patterns of mesoporous iron oxides.

Nitrogen sorptions and Barrett-Joyner-Halenda (BJH) pore size distributions are shown in Figure 7 (a) and (b). All iron oxides show characteristic Type-IV adsorption isotherms suggesting that the materials preserve the mesoporous structure with different reaction temperatures, heating cycles, and heating atmosphere. In addition, these different experimental parameters in the synthesis of mesoporous iron oxide show excellent control in the development of pores and phases. Compared with 2-line ferrihydrite, mesoporous α-Fe_2O_3 shows pore expansion, increase in *d*-spacing, and decrease in surface area (Figure 6 (b), Figure 7 (b) and Table 2) caused by nanoparticle sintering upon thermal treatment at a higher calcination temperature (350 °C). At a reaction temperature of 100 °C, γ-Fe_2O_3 with a final calcination temperature of 250 °C has a similar pore size distribution as α-Fe_2O_3 with a final calcination temperature of 350 °C (Figure 7 (b)). Furthermore, mesoporous Fe_3O_4 has much larger pore size than the other mesoporous iron oxides, including mesoporous α-Fe_2O_3 which is further treated at a higher calcination temperature. The detailed structural parameters of mesoporous iron oxides are listed in Table 2. UCT materials have a typical unit-cell

expansion behavior upon heat treatment caused by nanoparticle sintering [3,103]. The explanation of pore expansion could be that different phases of materials have different tendency of sintering on heat treatment. So even after the same calcination cycle at 150 °C for 12 hours and 250 °C for 4 hours, mesoporous 2-line ferrihydrite, γ-Fe_2O_3, and Fe_3O_4 nanocrystals have different extents of pore expansion. Mesoporous α-Fe_2O_3 has larger pore size than mesoporous 2-line ferrihydrite because further heat treatment at 350 °C will cause more sintering of nanoparticles.

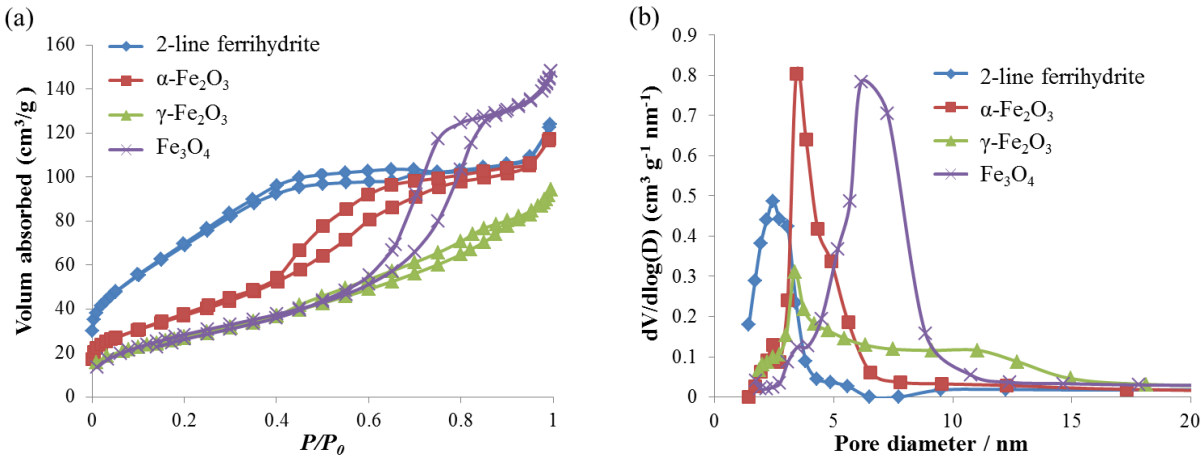

Figure 7: (a) N_2 sorption isotherms (b) BJH pore size distributions for mesoporous iron oxides.

Table 2: Structure parameters of mesoporous iron oxides.

	2-line ferrihydrite	α-Fe_2O_3	γ-Fe_2O_3	Fe_3O_4
Surface area (m^2/g)	258	137	100	75
Pore size (nm)	2.2	3.4	5.1	7.1
Pore volume (cm^3/g)	0.20	0.19	0.15	0.18

SEM and TEM images of mesoporous iron oxides are shown in Figure 8. SEM, iron oxide nanoparticles have the morphology of spherical, hedgehog-like, or pin-cushion aggregates that consist of radially oriented nanoparticles. Observed in TEM images, the thorns are formed by small

crystalline nanosize particles and pores are formed among these nanosize particles. All TEM images are collected at the same magnification. Hence, the effects of experimental parameters on pore sizes and aggregation of nanoparticles can be observed. The order of pore sizes of mesoporous iron oxides (Fe_3O_4 > γ-Fe_2O_3 > α-Fe_2O_3 > 2-line ferrihydrite) matches that of pore sizes obtained from BET pore size distributions.

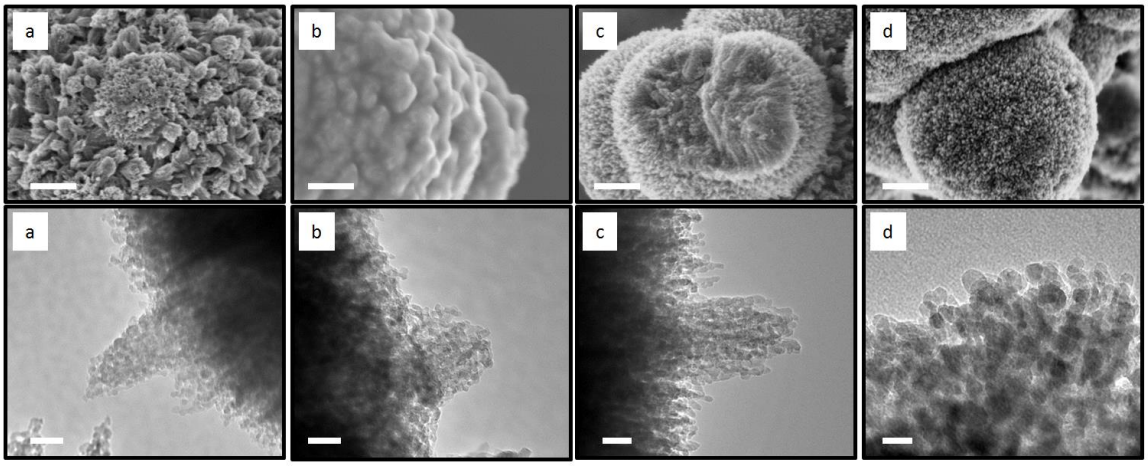

Figure 8: SEM images (top row) and TEM images (bottom row) of mesoporous (a) 2-line ferrihydrite (b) α-Fe_2O_3 (c) γ-Fe_2O_3 (d) Fe_3O_4 (scale bars are 200 nm in SEM images and scale bars are 20 nm in TEM images).

Raman spectra of mesoporous 2-line ferrihydrite, α-Fe_2O_3, γ-Fe_2O_3, and Fe_3O_4 are shown in Figure 9. Raman can detect phase information which can help us confirm the phases of iron oxides. Raman spectra of iron oxides match literature spectra [95,104,105] very well. Mesoporous 2-line ferrihydrite matches 2-line ferrihydrite in the literature. Peaks in the spectrum of mesoporous α-Fe_2O_3 are 228 cm^{-1}, 246 cm^{-1}, 293 cm^{-1}, 411 cm^{-1}, 497 cm^{-1}, 616 cm^{-1}, and 1320 cm^{-1}. Peaks in the spectrum of mesoporous γ-Fe_2O_3 are 352 cm^{-1}, 504 cm^{-1}, 719 cm^{-1}, and 1409 cm^{-1}. Peaks in the spectrum of mesoporous Fe_3O_4 are 352 cm^{-1}, 528 cm^{-1}, and 682 cm^{-1}. The peak shift (676 cm^{-1} to

682 cm^{-1}) [95] of Fe_3O_4 is attributed to non-equivalent sites or internal strain in the structure. [95,104].

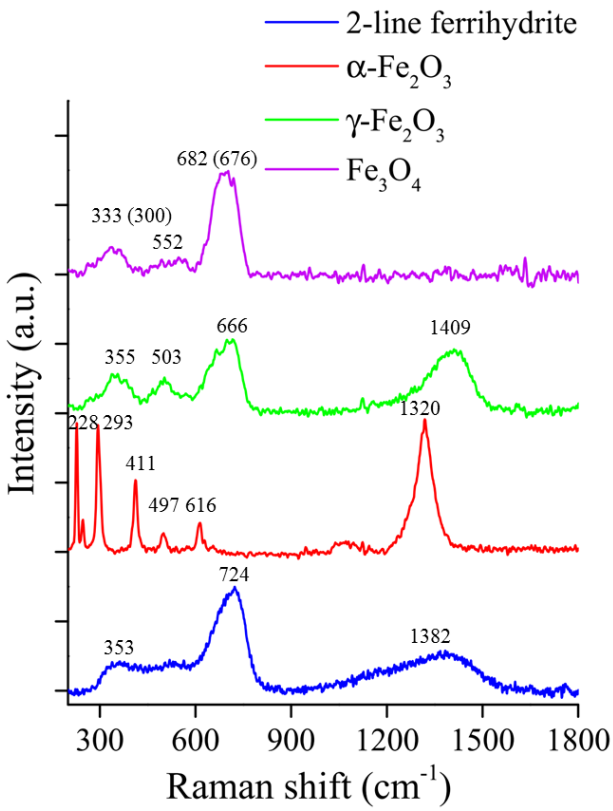

Figure 9: Raman spectra of mesoporous 2-line ferrihydrite, α-Fe_2O_3, γ-Fe_2O_3, and Fe_3O_4.

Figure 10 shows the XANES data of mesoporous 2-line ferrihydrite, α-Fe_2O_3, γ-Fe_2O_3, and Fe_3O_4 compared with standard iron oxides. From the XANES data, the mesoporous 2-line ferrihydrite, α-Fe_2O_3 match standard α-Fe_2O_3 very well. Mesoporous γ-Fe_2O_3 and Fe_3O_4 match standard γ-Fe_2O_3 and Fe_3O_4 very well. The average oxidation states of mesoporous 2-line ferrihydrite, α-Fe_2O_3, γ-Fe_2O_3, and Fe_3O_4 are 2.84, 2.77, 2.68, and 2.56 respectively. From the average oxidation state, all the mesoporous iron oxides have some oxygen vacancies.

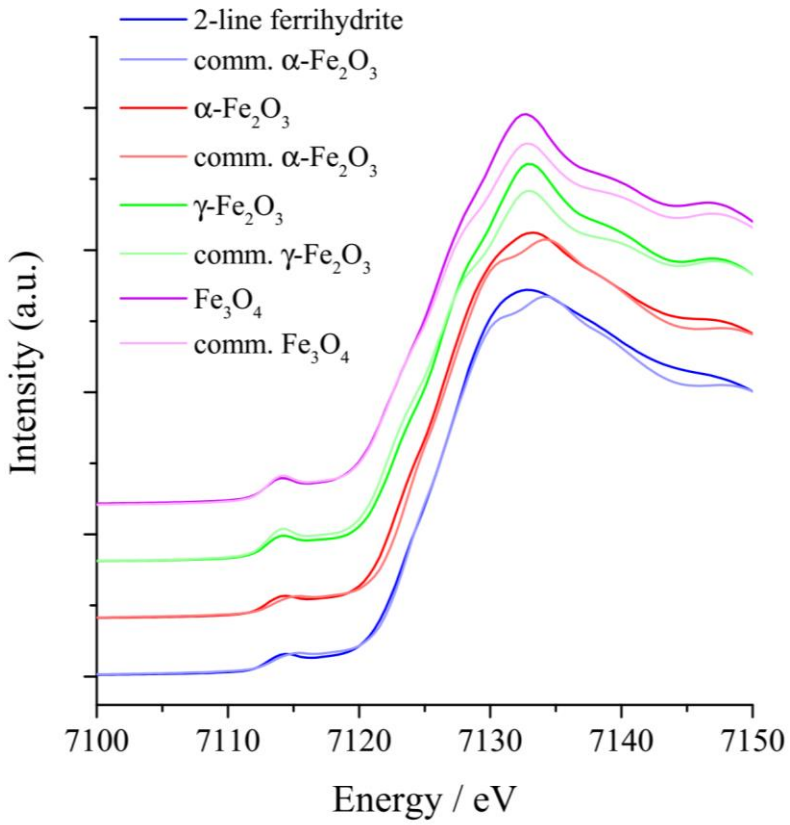

Figure 10: XANES data of mesopporous (a) 2-line ferrihydrite, (b) α-Fe_2O_3, (c) γ-Fe_2O_3, and (d) Fe_3O_4 (dark lines) compared with standard samples (light lines) (a) α-Fe_2O_3, (b) α-Fe_2O_3, (c) γ-Fe_2O_3, and (d) Fe_3O_4.

Figure 11 presents field-dependent magnetism by VSM of mesoporous γ-Fe_2O_3 and Fe_3O_4 catalysts at 300K. The mesoporous γ-Fe_2O_3 and Fe_3O_4 catalysts exhibit superparamagnetic behavior [106,107] with saturated magnetization values of 39.8 emu/g and 45.7 emu/g respectively. Mesoporous γ-Fe_2O_3 and Fe_3O_4 catalysts can be easily recycled by external magnets because of their superparamagnetic properties. This is an additional advantage of mesoporous iron oxide catalysts.

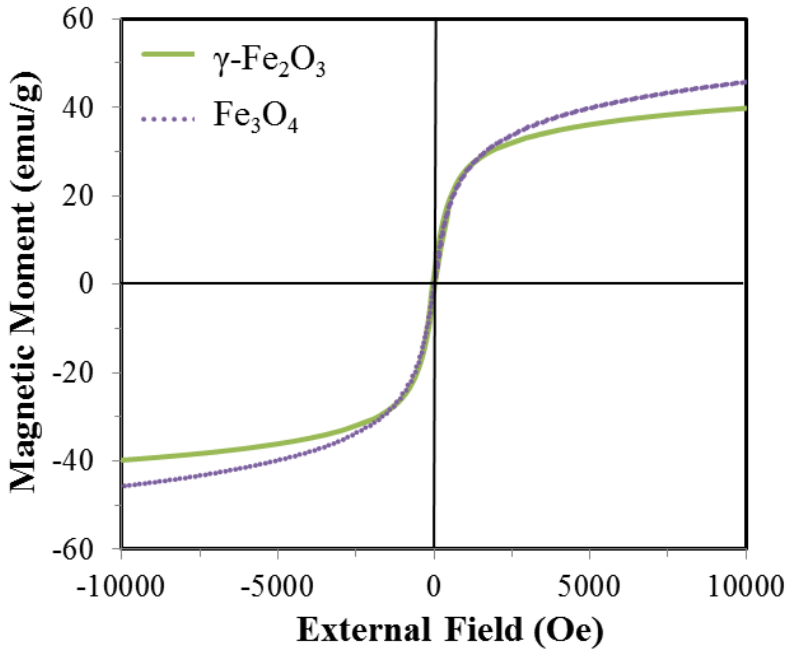

Figure 11: Vibrating sample magnetometer curves of mesoporous γ-Fe_2O_3 and Fe_3O_4 at 300 K.

The picture of the samples (Figure 12) shows that the mesoporous 2-line ferrihydrite, α-Fe_2O_3, and γ-Fe_2O_3 are dark brown and the mesoporous Fe_3O_4 is black. The colors of the samples indicate mesoporous iron oxides are able to absorb visible light.

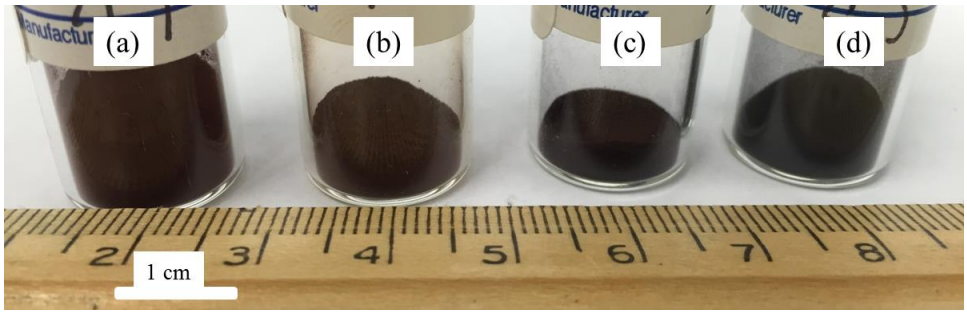

Figure 12: Picture of mesoporous (a) 2-line ferrihydrite, (b) α-Fe_2O_3, (c) γ-Fe_2O_3, and (d) Fe_3O_4 materials.

3.3 Mesoporous & magnetically recyclable catalysts

3.3.1 *Synthesis procedure*

Pd/meso-γ-Fe_2O_3 by impregnation method

For the synthesis of the mesoporous γ-Fe_2O_3 support, a solution was prepared by adding 0.01 mol iron nitrate, 0.12 mol 1-butanol, 0.019 mol nitric acid, and 2.04×10^{-4} mol poly(ethylene glycol)-block-poly(propylene glycol)-block-poly(ethylene glycol) (P123, M_n~5800). The clear solution was placed in the oven at 100 °C and then heated to 150 °C for 12 hours and 250 °C for 4 hours under an air atmosphere. The freshly made palladium nitrate aqueous solution with the same volume as the pore volume of the mesoporous γ-Fe_2O_3 support was added to mesoporous γ-Fe_2O_3. Then the Pd impregnated mesoporous γ-Fe_2O_3 was dried at 40 °C for 30 min to remove water and heated at 150 °C for 1 hour to remove the nitrate ions. Pd loading amounts on mesoporous γ-Fe_2O_3 were 1% and 2% in molar ratio. The catalysts synthesized in this way are written as 1% Pd/meso-γ-Fe_2O_3-im and 2% Pd/meso-γ-Fe_2O_3-im (listed in Table 1). Both catalysts were reduced under mild conditions in hydrogen before the reactions.

Pd/meso-γ-Fe_2O_3 by one-step sol-gel method

The palladium nitrate was added in the initial solution which contained 0.01 mol iron nitrate, 2.04×10^{-4} mol P123, 0.019 mol nitric acid, and 0.12 mol 1-butanol. All the following synthesis steps were the same as those for mesoporous γ-Fe_2O_3 [3]. Pd loadings of 1% and 2% molar ratio were used to synthesize Pd/meso-γ-Fe_2O_3 following the one-step sol-gel method. These catalysts are written as 1% Pd/meso-γ-Fe_2O_3-os and 2% Pd/meso-γ-Fe_2O_3-os (listed in Table 1). Both catalysts were reduced under mild conditions in hydrogen before the reactions.

Other catalysts containing Pd by impregnation method

Commercial Fe_2O_3 (non-porous maghemite), mesoporous SiO_2, and mesoporous carbon were also used as the supports to synthesize Pd-containing catalysts. The Pd impregnation of these materials follows the exact same procedures as those of the Pd impregnated mesoporous γ-Fe_2O_3 catalysts. Mesoporous SiO_2 and mesoporous carbon were synthesized by the same inversed micelle method as the mesoporous mesoporous γ-Fe_2O_3 [3]. All the catalysts synthesized by the impregnation method with these supports were loaded with 1% Pd molar content. These catalysts are written as 1% Pd/comm-Fe_2O_3-im, 1% Pd/meso-SiO_2-im, and 1% Pd/meso-C-im, respectively (listed in Table 1). All the catalysts were reduced under mild conditions in hydrogen before the reactions.

3.3.2 *Characterization*

Figure 13 shows the low-angle PXRD patterns of mesoporous SiO_2, 1% Pd/meso-SiO_2-im, mesoprous carbon, 1% Pd/meso-C-im, commercial Fe_2O_3, 1% Pd/comm-Fe_2O_3-im, mesoporous γ-Fe_2O_3, 1% and 2% Pd/meso-γ-Fe_2O_3-im, and 1% and 2% Pd/meso-γ-Fe_2O_3-os catalysts. Mesoporous SiO_2, mesoporous carbon, and mesoporous γ-Fe_2O_3 catalysts show peaks in the low-angle PXRD patterns, reflecting meso-structures of these catalysts. After synthesis of Pd-containing catalysts using impregnation and one-step sol-gel methods, all the catalysts still show peaks in low-angle PXRD patterns, indicating that after impregnating or doping Pd into the mesoporous supports, the supports still maintain a meso-structure. The *d*-spacings of mesoporous SiO_2, mesoporous carbon, mesoporous γ-Fe_2O_3 are 38Å (2.30°), 54Å (1.65°), and 41Å (2.14°), respectively. After Pd impregnation, the *d*-spacings of 1% Pd/meso-SiO_2-im and 1% Pd/meso-C-im catalysts shift to 23 Å (3.83°) and 24 Å (3.71°) while the peak positions of 1% and 2% Pd/meso-γ-Fe_2O_3-im catalysts do not change much. Although the peak positions of 1% and 2% Pd/meso-γ-

Fe_2O_3-im catalysts in the low-angle PXRD patterns remain relatively unaffected, the change of the shape of peaks indicates that the impregnation of Pd nanoparticles has an impact on the structure of mesoporous γ-Fe_2O_3. The 1% and 2% Pd/meso-γ-Fe_2O_3-os catalysts both show peaks at a *d*-spacing of 41 Å (2.15°) in the low-angle PXRD patterns.

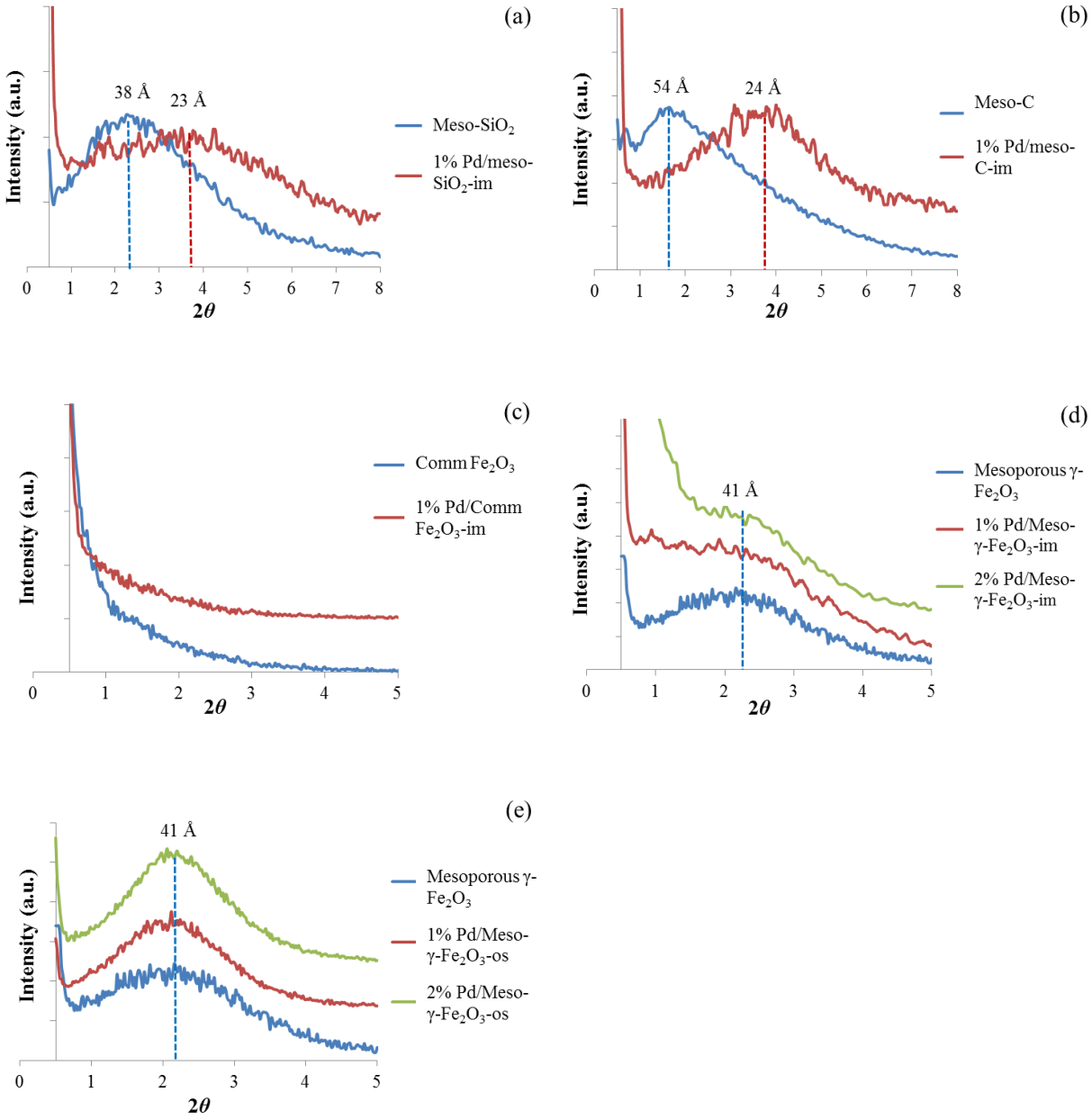

Figure 13: Low-angle PXRD patterns of (a) mesoporous SiO_2 and 1% Pd/meso-SiO_2-im, (b) mesoporous carbon and 1% Pd/meso-C-im, (c) commercial Fe_2O_3 and 1% Pd/comm-Fe_2O_3-im, (d) mesoporous γ-Fe_2O_3, 1%, and 2% Pd/meso-γ-Fe_2O_3-im, and (e) mesoporous γ-Fe_2O_3, 1% and 2% Pd/meso-γ-Fe_2O_3-os catalysts.

Figure 14 shows the high-angle PXRD patterns of mesoporous SiO_2, 1% Pd/meso-SiO_2-im, mesoprous carbon, 1% Pd/meso-C-im, mesoporous γ-Fe_2O_3, 1% and 2% Pd/meso-γ-Fe_2O_3-im, and 1% and 2% Pd/meso-γ-Fe_2O_3-os catalysts. Mesoporous SiO_2 and mesoporous carbon show broad peaks at 23.1° and 22.8°, respectively. After 1% Pd impregnation, a weak peak at 2θ=33.8° is observed in the high-angle PXRD pattern of mesoporous SiO_2, which matches well with PdO (standard PDF card 02-1432). After 1% Pd impregnation, weak peaks at 2θ=33.8°, 42.3°, 55.2°, 61.0°, and 72.2° are observed in the high-angle PXRD pattern of mesoporous carbon, which also match well with PdO. The 1% and 2% Pd/meso-γ-Fe_2O_3 catalysts synthesized using the impregnation and one-step sol-gel methods match with maghemite (standard PDF card 39-1346) very well. The palladium peaks are too small to be observed in the high-angle PXRD patterns of Pd/meso-γ-Fe_2O_3 catalysts synthesized using the impregnation and one-step sol-gel methods. Using the Scherrer equation and the broadening of the (220), (311), (400), (422), (511), and (440) reflections, the particle sizes of 1% Pd/comm-Fe_2O_3-im, 1% Pd/meso-γ-Fe_2O_3-im, 2% Pd/meso-γ-Fe_2O_3-im, 1% Pd/meso-γ-Fe_2O_3-os, 2% Pd/meso-γ-Fe_2O_3-os catalysts are 25.8 nm, 11.9 nm, 11.9 nm, 12.8 nm, and 8.1 nm, respectively. The particle sizes of 1% Pd/meso-SiO_2-im and 1% Pd/meso-C-im catalysts are not available because of their amorphous nature shown in high-angle PXRD patterns.

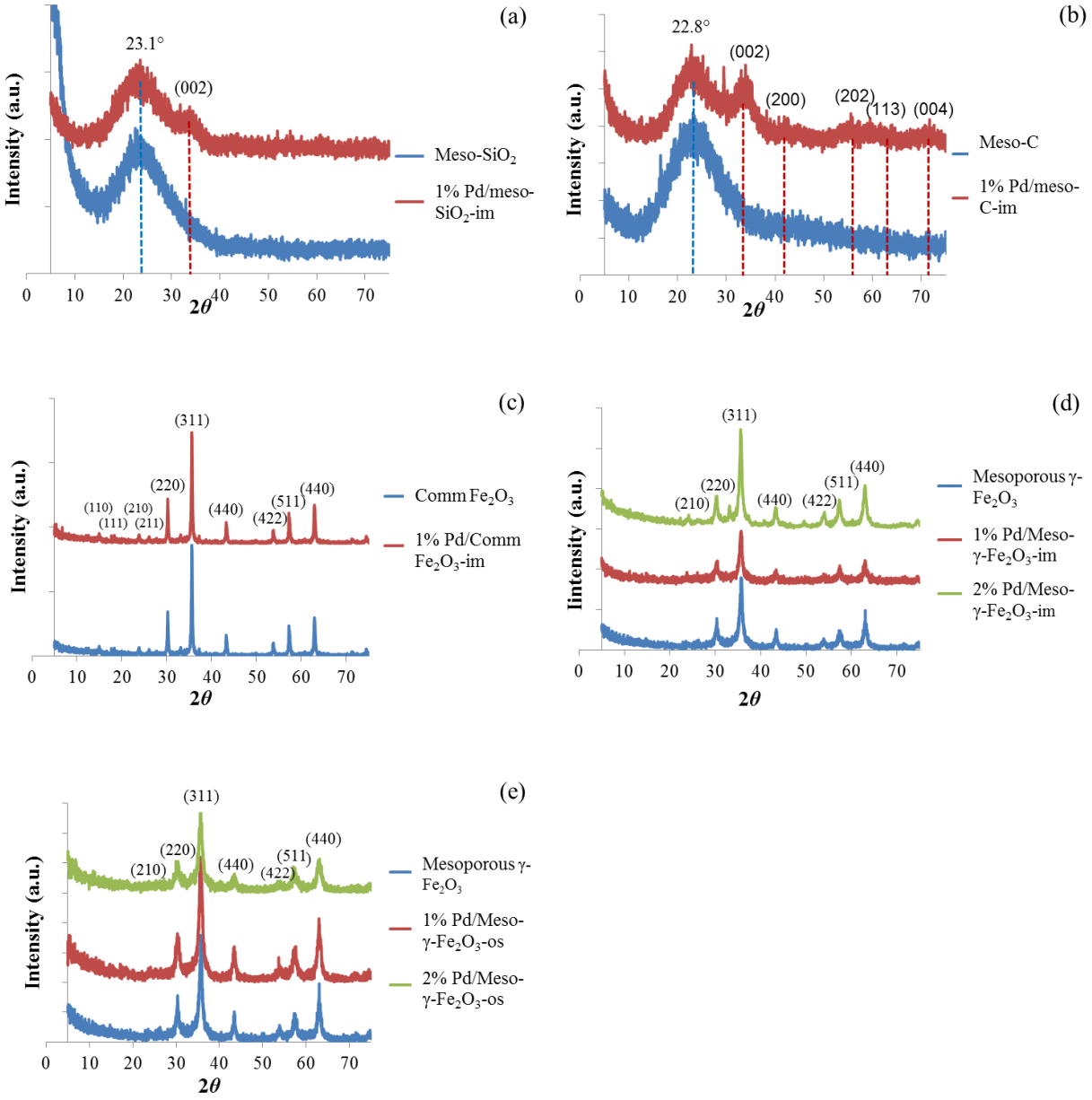

Figure 14: High-angle PXRD patterns of (a) mesoporous SiO_2 and 1% Pd/meso-SiO_2-im, (b) mesoporous carbon and 1% Pd/meso-C-im, (c) commercil Fe_2O_3 and 1% Pd/comm-Fe_2O_3-im, (d) mesoporous γ-Fe_2O_3, 1%, and 2% Pd/meso-γ-Fe_2O_3-im, and (e) mesoporous γ-Fe_2O_3, 1% and 2% Pd/meso-γ-Fe_2O_3-os catalysts. (The planes in (a) and (b) refer to the reflections of PdO; the planes in (c), (d), and (e) refer to the reflections in maghemite.)

Table 3 lists the surface area and porosity of mesoporous SiO_2, 1% Pd/meso-SiO_2-im, mesoprous carbon, 1% Pd/meso-C-im, commercial Fe_2O_3, 1% Pd/comm-Fe_2O_3-im, mesoporous γ-Fe_2O_3, 1% and 2% Pd/meso-γ-Fe_2O_3-im, and 1% and 2% Pd/meso-γ-Fe_2O_3-os catalysts. The surface areas of 1% Pd/meso-SiO_2-im and 1% Pd/meso-C-im catalysts decrease after Pd impregnation compared with the original mesoporous SiO_2 and carbon. The pore sizes of 1% Pd/meso-SiO_2-im and 1% Pd/meso-C-im also changed after Pd impregnation compared with original mesoporous SiO_2 and mesoporous carbon due to the impregnation of palladium. The surface area, pore size, and pore volume of 1%, 2% Pd/meso-γ-Fe_2O_3-im and 1% Pd/meso-γ-Fe_2O_3-os catalysts are similar to the original mesoporous γ-Fe_2O_3 catalyst. The 1% and 2% Pd/meso-γ-Fe_2O_3-os catalysts have larger surface areas and pore volumes than the intrinsic mesoporous γ-Fe_2O_3 catalyst. The 2% Pd/meso-γ-Fe_2O_3-os catalyst has a larger pore size than 1% Pd/meso-γ-Fe_2O_3-os and intrinsic mesoporous γ-Fe_2O_3 catalysts. The BET isotherms of these catalysts are shown in Figure 15. All the N_2 isotherms of mesoporous samples before and after Pd loadings are Type IV isotherms, which indicate the mesoporosity of the structures.

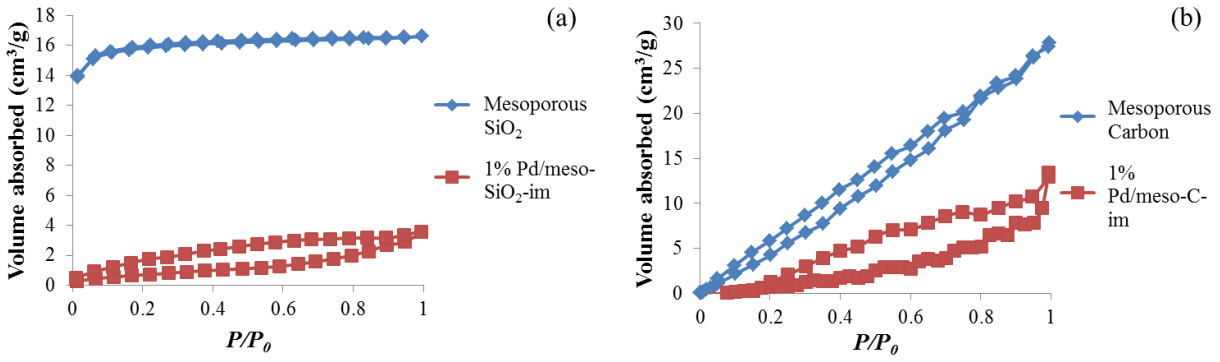

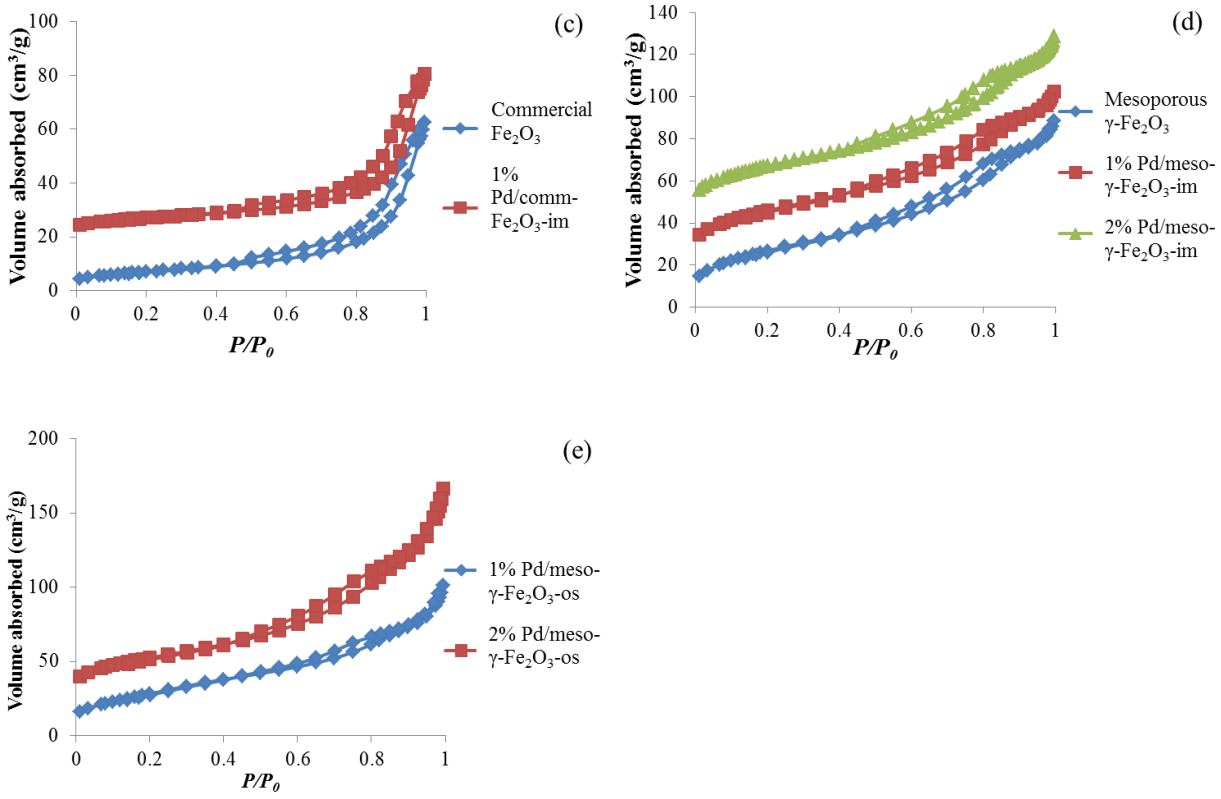

Figure 15: BET isotherms of (a) mesoporous SiO_2 and 1% Pd/meso-SiO_2-im, (b) mesoporous carbon and 1% Pd/meso-C-im, (c) commercial Fe_2O_3 and 1% Pd/comm-Fe_2O_3-im, (d) mesoporous γ-Fe_2O_3, 1%, and 2% Pd/meso-γ-Fe_2O_3-im, and (e) 1% and 2% Pd/meso-γ-Fe_2O_3-os catalysts. (The blue lines in (c), (d), and (e) are offset 20 cm^3/g each and green line in (d) is offset 40 cm^3/g)

Table 3: The structural parameters of catalysts containing Pd by the impregnation and one-step sol-gel methods.

	Surface area (m^2/g)	Pore size (Å)	Pore volume (cm^3/g)
Mesoporous SiO_2	442	18	0.01
1% Pd/meso-SiO_2-im	27	27	0.03
Mesoporous Carbon	424	32	0.04
1% Pd/meso-C-im	41	20	0.03
Commercial Fe_2O_3	26	-	-
1% Pd/comm-Fe_2O_3-im	26	-	-
Mesoporous γ-Fe_2O_3	99	54	0.14
1% Pd/meso-γ-Fe_2O_3-im	95	52	0.13
2% Pd/meso-γ-Fe_2O_3-im	99	56	0.14
1% Pd/meso-γ-Fe_2O_3-os	105	56	0.16

2% Pd/meso-γ-Fe_2O_3-os	118	71	0.23

- Not available

Figure 16 shows the TEM images of 1% Pd/meso-SiO_2-im, 1% Pd/meso-C-im, 1% Pd/comm-Fe_2O_3-im, 1% and 2% Pd/meso-γ-Fe_2O_3-im, and 1% and 2% Pd/meso-γ-Fe_2O_3-os catalysts. The support of the Pd/meso-γ-Fe_2O_3 catalyst is spherical, "hedgehog-like", or "pin-cushion" aggregates that consist of radially oriented nanoparticles. In circled areas of the TEM images, Pd/Fe or Pd/Si or Pd/C ratios are different from the ratios in bulk areas. The Pd/Fe or Pd/Si or Pd/C ratios of circled areas and bulk from EDX spectra are listed in Table 4. The dispersion of Pd nanoparticles in the mesoporous γ-Fe_2O_3 matrix can be observed by TEM images at the thin region of the sample (Figure 40) and the dark spots are proved to be Pd nanoparticles by the inserted HRTEM image. The bulk Pd/Fe ratios of 1% Pd/comm-Fe_2O_3-im, 1% and 2% Pd/meso-γ-Fe_2O_3-im, and 1% and 2% Pd/meso-γ-Fe_2O_3-os catalysts are 0.026, 0.023, 0.054, 0.024, and 0.048, respectively. The bulk Pd/Fe_2O_3 ratios of 1% Pd/comm-Fe_2O_3-im, 1% and 2% Pd/meso-γ-Fe_2O_3-im, and 1% and 2% Pd/meso-γ-Fe_2O_3-os catalysts are 0.013, 0.012, 0.027, 0.012, and 0.024, respectively. So the actual Pd concentrations in these five catalysts are close to Pd concentrations we used for synthesis.

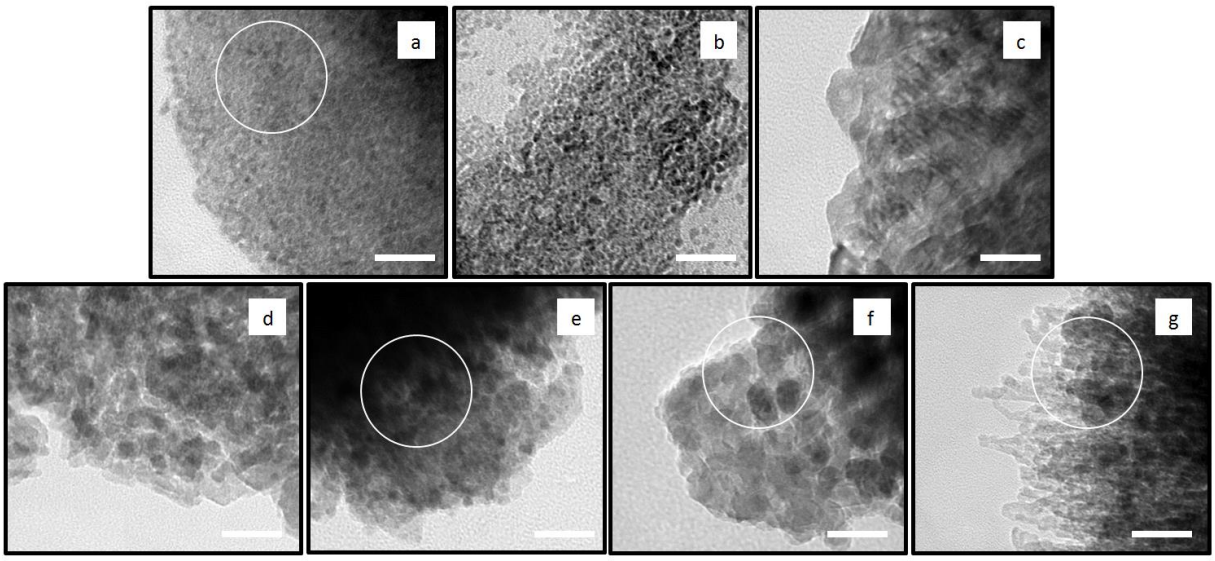

Figure 16: TEM images of (a) 1% Pd/meso-SiO_2-im, (b) 1% Pd/meso-C-im, (c) 1% Pd/comm-Fe_2O_3-im, (d) 1% Pd/meso-γ-Fe_2O_3-im, (e) 2% Pd/meso-γ-Fe_2O_3-im, (f) 1% Pd/meso-γ-Fe_2O_3-os, and (g) 2% Pd/meso-γ-Fe_2O_3-os catalysts. (scale bar 20 nm).

Figure 17 shows XPS spectra of the Pd 3d region of 1% Pd/meso-SiO_2-im, 1% Pd/meso-C-im, 1% Pd/comm-Fe_2O_3-im, 1% and 2% Pd/meso-γ-Fe_2O_3-im, and 1% and 2% Pd/meso-γ-Fe_2O_3-os catalysts after the *in-situ* reduction. To analyze XPS spectra, the peaks were deconvoluted to all the possible Pd species, like Pd, PdO, PdO_2, $Pd(NO_3)_2$, or combinations of these possible Pd species. The most reasonable peak fittings are shown in Figure 17. From the deconvolution of the curves, the most possible species existing in the catalysts after *in-situ* reduction is Pd(0). The spectra show two main peaks at around 335.5 eV and 340.7 eV, which can be ascribed to Pd $3d_{5/2}$ and Pd $3d_{3/2}$, respectively. The Pd/Fe ratios from XPS survey that give the surface compositions of catalysts are listed in Table 2. The Pd/Fe ratios on the surface of 1% Pd/comm-Fe_2O_3-im, 1% and 2% Pd/meso-γ-Fe_2O_3-im, and 1% Pd/meso-γ-Fe_2O_3-os catalysts are similar to the bulk. Only for 2% Pd/meso-γ-Fe_2O_3-os catalyst is the Pd/Fe ratio on the surface much higher than that in the bulk.

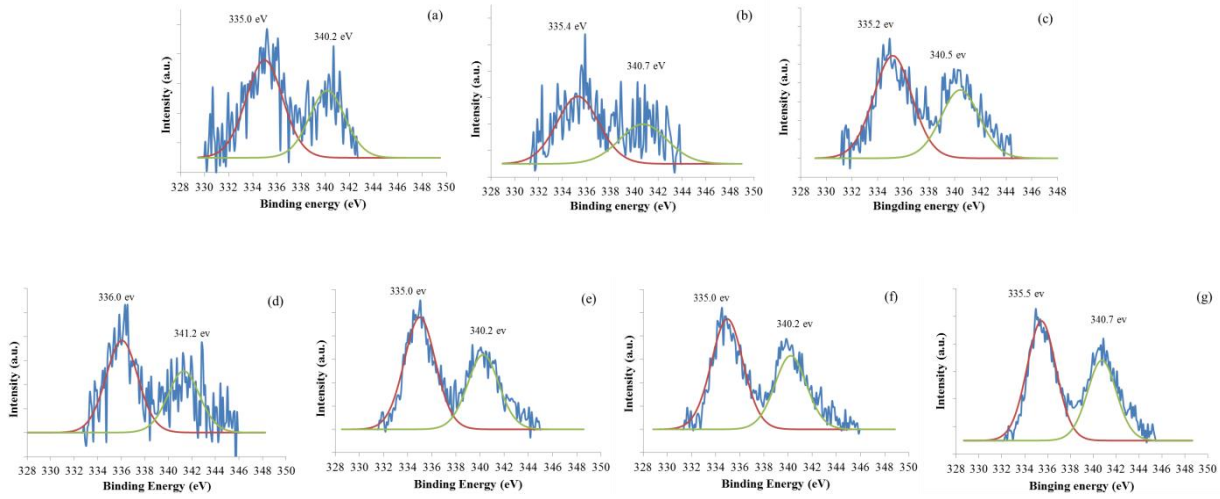

Figure 17: XPS spectra of Pd 3d region of (a) 1% Pd/meso-SiO_2-im, (b) 1% Pd/meso-C-im, (c) 1% Pd/comm-Fe_2O_3-im, (d) 1% Pd/meso-γ-Fe_2O_3-im, (e) 2% Pd/meso-γ-Fe_2O_3-im, (f) 1% Pd/meso-γ-Fe_2O_3-os, and (g) 2% Pd/meso-γ-Fe_2O_3-os catalysts after *in-situ* reduction.

Table 4: Pd/Fe ratio or Pd/Si or Pd/C [a] by EDX and XPS survey

	Circled area [b]	Bulk [b]	Surface [d]
1% Pd/meso-SiO_2-im	17.8	0.029	-
1% Pd/meso-C-im	-	0.112 [c]	-
1% Pd/comm-Fe_2O_3-im	-	0.026	0.012
1% Pd/meso-γ-Fe_2O_3-im	-	0.023	0.011
2% Pd/meso-γ-Fe_2O_3-im	0.179	0.054	0.051
1% Pd/meso-γ-Fe_2O_3-os	0.213	0.024	0.029
2% Pd/meso-γ-Fe_2O_3-os	0.106	0.048	0.219

[a] Pd/Fe ratio applies to 1% Pd/comm-Fe_2O_3-im, 1% Pd/meso-γ-Fe_2O_3-im, 2% Pd/meso-γ-Fe_2O_3-im, 1% Pd/meso-γ-Fe_2O_3-os, and 2% Pd/meso-γ-Fe_2O_3-os catalysts; Pd/Si ratio applies to 1% Pd/meso-SiO_2-im. Pd/C ratio applies to 1% Pd/meso-C-im catalyst.

[b] "Circled area and bulk" refer to different regions in TEM images and both ratios were obtained from EDX detector which is attached TEM.

[c] Pd/C ratio of 1% Pd/meso-C-im is obtained with an EDX detector attached to a scanning electron microscope by putting the sample on a copper tape. This ratio is for reference only, because it can be affected by the environment.

[d] Surface composition ratio was obtained from XPS survey analysis. The surface compositions of 1% Pd/meso-SiO_2-im and 1% Pd/meso-C-im catalysts are not available because of the low signal to noise ratio of Pd in these two samples.

- Not available.

Figure 18 shows magnetization hysteresis loops obtained at 300 K for mesoporous γ-Fe_2O_3, 1% Pd/meso-γ-Fe_2O_3-im, 2% Pd/meso-γ-Fe_2O_3-im, 1% Pd/meso-γ-Fe_2O_3-os, and 2% Pd/meso-γ-Fe_2O_3-os catalysts. The saturated magnetization values of 1% and 2% Pd/meso-γ-Fe_2O_3-im catalysts are 51.3 emu/g and 50.8 emu/g, respectively. The saturated magnetization values of 1% and 2% Pd/meso-γ-Fe_2O_3-os catalysts are 46.0 emu/g and 48.0 emu/g, respectively. For comparison, the saturation magnetization for mesoporous γ-Fe_2O_3 is 52.4 emu/g. The magnetization curves show no remanence or coercivity at 300 K (room temperature), suggesting superparamagnetic behavior required for magnetic separation [108].

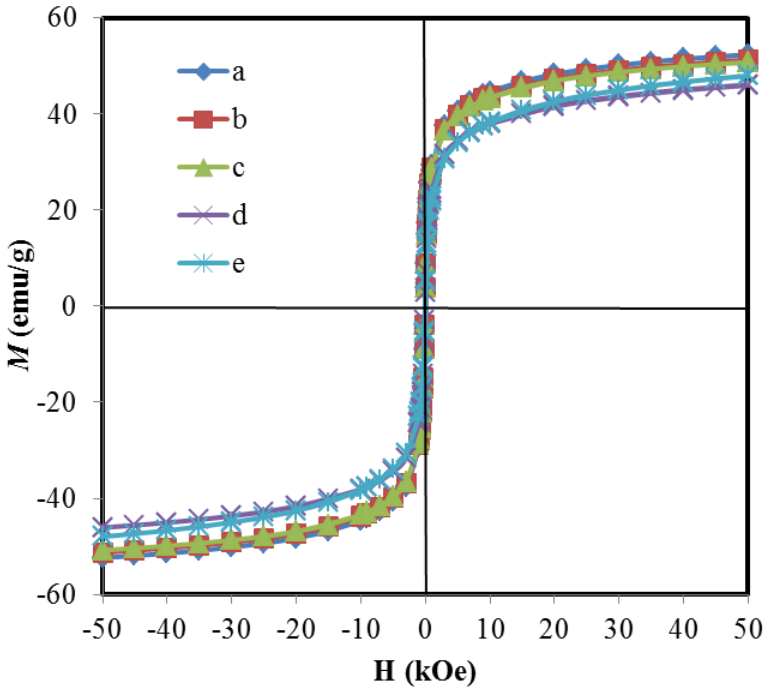

Figure 18: Magnetization hysteresis loops obtained at 300 K for: (a) mesoporous γ-Fe_2O_3, (b) 1% Pd/meso-γ-Fe_2O_3-im, (c) 2% Pd/meso-γ-Fe_2O_3-im, (d) 1% Pd/meso-γ-Fe_2O_3-os, and (e) 2% Pd/meso-γ-Fe_2O_3-os catalysts. The absence of remanence and coercivity at room temperature is necessary for magnetic separation.

3.4 Mesoporous aluminosilicate adsorbents

3.4.1 *Synthesis procedure*

Mesoporous aluminosilicates were synthesized by the sol-gel-based inverse micelle method. Tetraethylorthosilicate (0.02 mol) and aluminum nitrate (Si:Al=5, 10, and 20 molar ratio) were dissolved in a solution containing 0.188 mol (14 g) of 1-butanol, 0.022 mol (2 g) of HNO_3, and 2 g of P123 surfactant at room temperature under magnetic stirring. Then, the obtained clear gel was placed in an oven at 120 °C for 4 hours. Lastly, the obtained transparent yellow film was placed in a calcination cuvette and calcined in air at 550 °C for 4 hours at the heating rates of 1 °C/min, 5 °C/min, and 10 °C/min. The samples were taken out of the furnace right after 4 hours calcination. A constant heating rate of 2 °C/min and a constant Si:Al ratio of 5 were maintained when different aluminum dopant amounts and different calcination heating rates were studied, respectively. The mesoporous aluminosilicates synthesized by this sol-gel based inverse micelle method are nanoparticle aggregations [3].

3.4.2 *Characterization*

All the synthesized mesoporous aluminosilicates show peaks at 2θ=0.8~2° in low-angle PXRD patterns, reflecting their meso-structure (Figure 19 (a, b)). The mesoporous aluminosilicates with Si:Al ratios of 10 and 20 have similar *d*-spacing of ~48 Å, while the aluminosilicate with a Si:Al ratio of 5 has a *d*-spacing of 80 Å. The aluminum is chosen to be the dopant metal due to similar atomic size with silica and can change the basicity of the adsorbents. Moreover, the mesoporous aluminosilicates with 1 °C/min, 5 °C/min, and 10 °C/min calcination heating rates have *d*-spacings of 100 Å, 75 Å, and 65 Å, respectively. Since the mesoporous aluminosilicates are synthesized from inverse micelles, the pores of mesoporous aluminosilicates are actually formed from the

voids among the inverse micelles. The *d*-spacing at the low-angle range of XRD correlates with the size of voids in the materials. Thus, the d spacing can reflect the pore size of the material to some extent [3,93,94,109,110]. The observation that the aluminosilicate with a larger amount of aluminum dopant has a larger *d*-spacing means that the aluminum dopant can possibly enlarge the pore size of the mesoporous aluminosilicate. However, the prediction of the pore size by *d*-spacing can not be applied to the mesoporous aluminosilicates synthesized under different calcination heating rates, since the calcination heating rate can change the atomic ordering of the SiO_2 structure [111]. The accurate pore sizes and pore size distributions of the mesoporous aluminosilicates are measured by nitrogen sorption. All the aluminosilicates have broad and low intensity peaks at 2θ=23.1° (*d*-spacing=3.8Å) in the high-angle PXRD patterns (Figure 19 (c, d)), reflecting their low crystallinity properties.

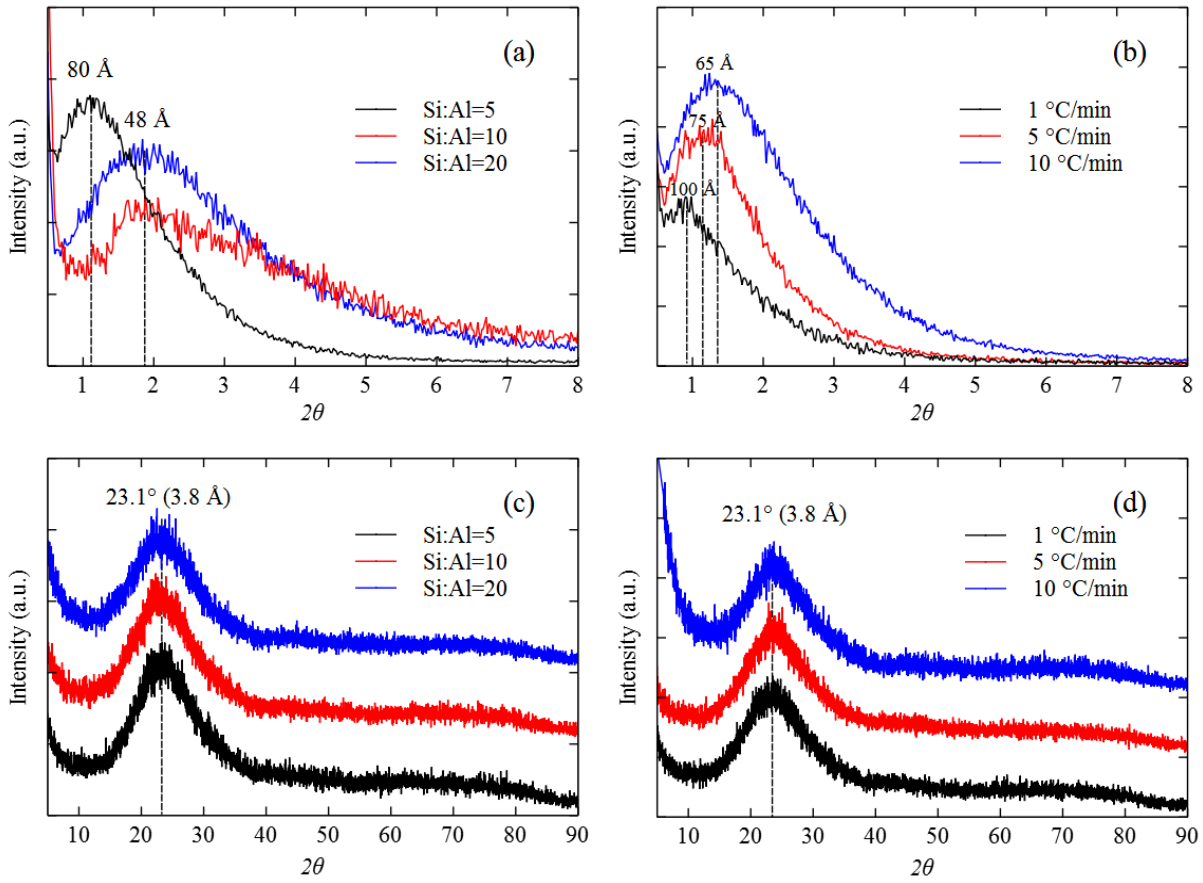

Figure 19: Low-angle PXRD patterns and high-angle PXRD patterns of mesoporous aluminosilicates with different aluminum dopant amounts (a, c) and different calcination heating rates (b, d).

Nitrogen adsorption/desorption analyses were performed to study the effect of aluminum dopant amounts and calcination heating rates on the textural properties of the adsorbents. Figure 20 shows the BET isotherms and cumulative pore volume distributions of the synthesized mesoporous aluminosilicates. Except for the isotherm of aluminosilicate with Si:Al ratio of 20, all the isotherms are "Type I-like" isotherms [112], indicative of both microporous and mesoporous characteristics [113]. According to NIST [114], these materials can be considered as mesoporous materials, even though the isotherms are "Type I-like" isotherms [115,116]. For a better discussion, detailed textural parameters of mesoporous aluminosilicates obtained from nitrogen sorptions are

summarized in Table 5. The morphology of the synthesized mesoporous aluminosilicates was shown in the SEM images (Figure 21).

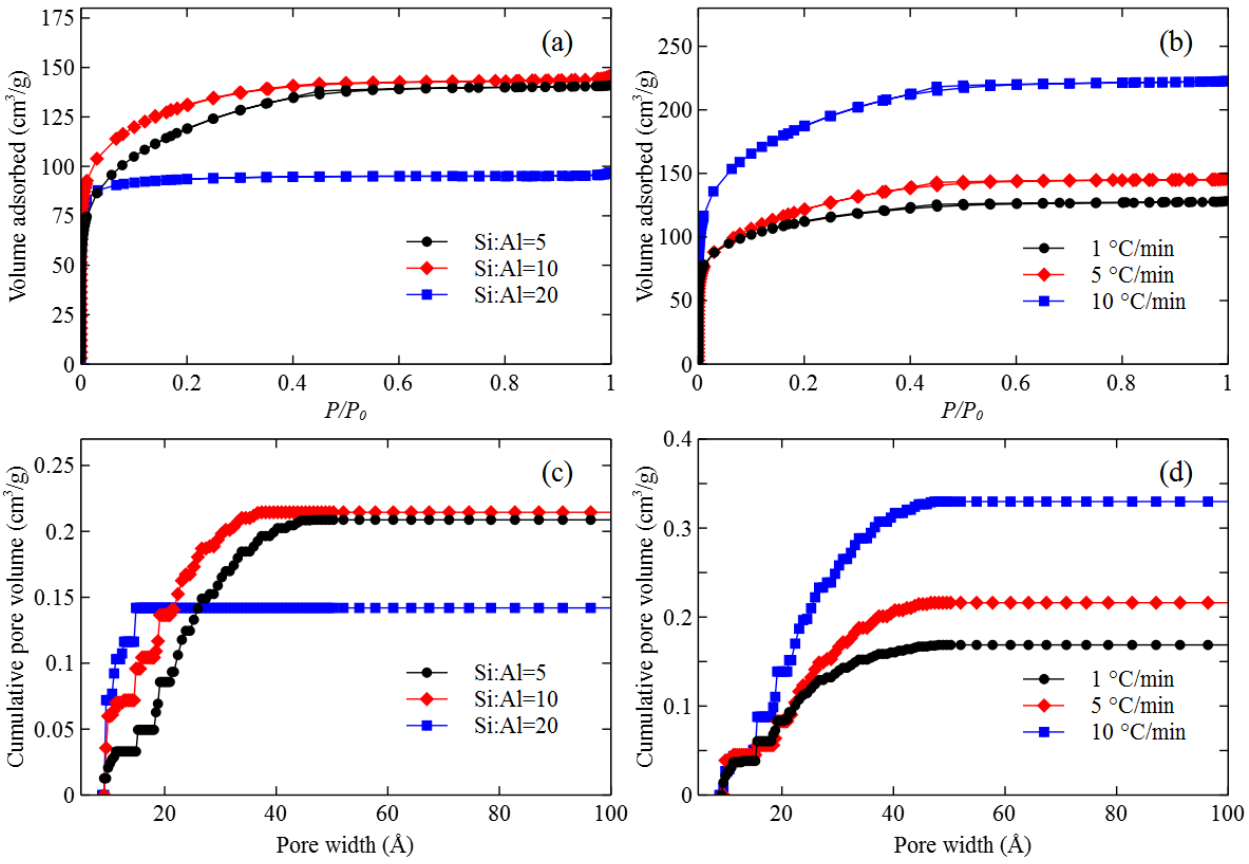

Figure 20: BET isotherms and cumulative pore volume distributions of mesoporous aluminosilicates with different aluminum dopant amounts (a, c) and different calcination heating rates (b, d).

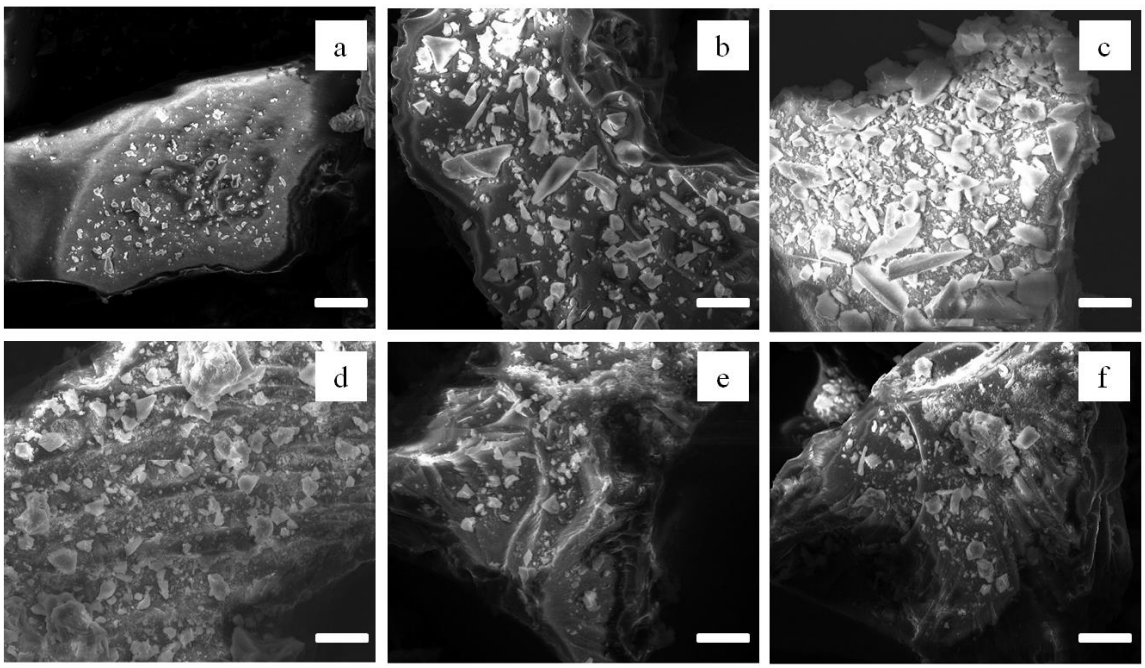

Figure 21: SEM images of mesoporous aluminosilicates with (a) Si:Al=5, (b) Si:Al=10, (c) Si:Al=20, (d) 1 °C/min heating rate, (e) 5 °C/min heating rate, and (f) 10 °C/min heating rate. (Scale bars are 20 μm.)

When the aluminum dopant amount increases, the external surface area and mesopore volume of the mesoporous aluminosilicates increase. Since UCT mesoporous materials are nanoparticle aggregates, introducing heteroatoms (such as aluminum) in the mesoporous materials during the sol-gel synthesis process leads to an increase in surface area [109,117], because the heteroatoms can prevent the nanoparticles from aggregating during the calcination. This explains the increased external surface area (the area of the particle outer surface, taken into account the roughness) as the aluminum content increases. At the same time, prevention of nanoparticle aggregation will also help preserve the mesopore volume of the mesoporous aluminosilicate since the mesopores synthesized by the sol-gel based inverse micelle method are actually formed in the space between the nanoparticles.

The decrease of the surface area due to large aluminum content was observed by Xia and Mokaya [118] during synthesis of MCM-48 using hydrothermal methods. The incorporation of Al into the mesostructured silica framework changed the structural ordering of the material, resulting in partial loss of the mesoporous structure. In contrast, our materials were synthesized by solvent evaporation. The aluminum dopants stayed between nanoparticles as heteroatoms rather than incorporate into the silica framework. During the calcination process, on one hand, the aluminum content prevented the aggregation of nanoparticles, which preserved the external surface area; on the other hand, the aluminum content blocked micro/mesopore channels [119], which decreased the micropore surface area. Therefore, overall, with the increased aluminum content, the BET surface area of our materials (sum of external surface area and micropore surface area) first increased and then decreased. This observation is consistent with the literature [120,121]. Moreover, the pores of our mesoporous materials were formed among the voids of nanoparticles. Thus, prevention of aggregation of nanoparticles by higher aluminum content could help preserve the pores of the materials, forming pores of larger size. The first increase and then decrease of total pore volume (sum of mesopore volume and micropore volume) with the increased aluminum dopant is attributed to the same phenomenon.

Table 5: Textual properties and D4 adsorption capacity of mesoporous aluminosilicates.

Heating rate (°C/min)	Si:Al ratios*	BET surface area (m^2/g)	External surface area (m^2/g)	Micropore surface area (m^2/g)	Total pore volume (cm^3/g)	V_{meso} (cm^3/g)	V_{micro} (cm^3/g)	Ave. pore size (Å)	Crystalline size (Å)**	Capacities (mg D4/g adsorbents)
2	5 (5.50)	424	309	115	0.209	0.115	0.151	20.5	74.9	77.0 ± 3.70
2	10 (15.1)	454	237	216	0.214	0.077	0.172	19.7	77.9	62.3 ± 3.85
2	20 (25.9)	313	38	275	0.142	0.013	0.141	19.0	71.3	10.3 ± 0.93
1	5 (5.11)	391	219	171	0.190	0.081	0.146	20.2	74.9	28.1 ± 0.93
5	5 (4.98)	433	327	106	0.216	0.125	0.153	20.8	78.1	88.2 ± 2.58

10	5 (5.09)	533	341	191	0.261	0.135	0.172	21.8	73.5	104.5 ± 1.71

* The numbers in the brackets are the actual ratios in the products determined by EDX.
** Calculated by Scherrer's equation.

The calcination heating rate can significantly affect the surface, chemical, and textural properties of the porous materials during the calcination process [122]. In this study, when the calcination heating rate increases, the BET surface area, the external surface area, the total pore volume, the mesopore volume, and the micropore volume all increase (Figure 20 (d) and Table 5). This observation is consistent with Bagshaw and Bruce's work [111], which concluded that the surface area, pore size, and pore volume of non-ionically PEO type surfactant templated materials (SBA-15 and MSU-X) can be increased by a fast calcination heating rate. This is probably caused by the heat released in the early stages of the combustion of oxygen rich P123 surfactant during the calcination (template removal step) [123]. The fast calcination heating rate causes the sample temperature to rise rapidly during the combustion of the template, producing excessive heat within a short time [111]. The released heat in a short time could cause the structural rearrangement, which will change the atomic ordering of the SiO_2 structure [111].

4. APPLICATION OF MESOPOROUS IRON OXIDES WITH DIFFERENT PHASES ON PHOTOCATALYTIC DYE DEGRADATION

4.1 Catalyst performance test

Figure 22 shows the adsorption capabilities of mesoporous iron oxides, compared with that of commercial Fe_2O_3. The average adsorption capability of commercial Fe_2O_3 is 21.1 mg/g. The greatest adsorption capability (49.3 mg/g) is found on mesoporous 2-line ferrihydrite. All of the mesoporous iron oxides have greater adsorption capability than the commercial iron oxide because of the large surface area of mesoporous Fe_2O_3. The adsorption capability of γ-Fe_2O_3 is similar to that of commercial Fe_2O_3. Furthermore, the adsorption capability of α-Fe_2O_3 and Fe_3O_4 is 50% more than that of commercial Fe_2O_3. In addition, the adsorption capability of 2-line ferrihydrite is more than twice that of the commercial Fe_2O_3. All these results prove that the mesoporous iron oxides synthesized by the sol-gel-based inverse micelle method have greater adsorption capability for orange II than commercial Fe_2O_3.

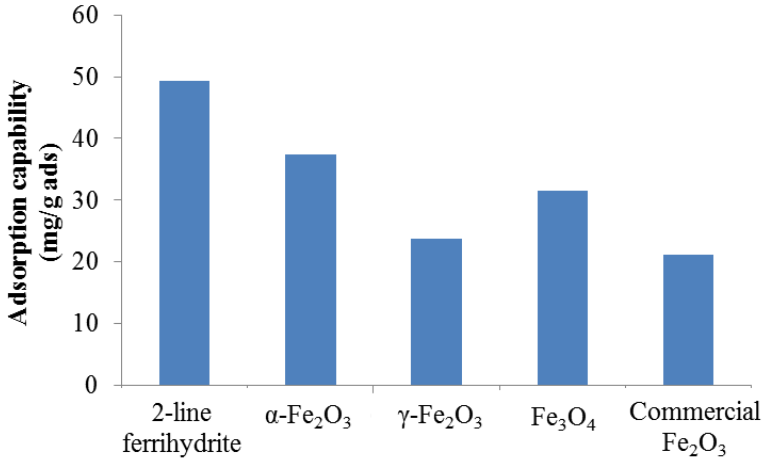

Figure 22: Adsorption capabilities of mesoporous 2-line ferrihydrite, α-Fe_2O_3, γ-Fe_2O_3, Fe_3O_4, and commercial Fe_2O_3.

Figure 23 shows the dye degradation efficiency with different mesoporous iron oxide compared with commercial iron oxide and catalyst free conditions under visible light in presence of H_2O_2. Without catalysts, the dyes can be slightly degraded by H_2O_2 under irradiation of visible light. Without H_2O_2, the dyes can only be adsorbed rather than be degraded by the catalysts under irradiation of visible light. After 8 hours, no more than 30% of dyes were degraded. In Figure 23, the rate constant of reaction without iron oxide catalysts was very slow compared to that with catalytic reactions. All the mesoporous 2-line ferrihydrite, α-Fe_2O_3, γ-Fe_2O_3, and Fe_3O_4 have higher rate constant than commercial Fe_2O_3. The commercial Fe_2O_3 catalysts can only degrade about 70% of the dye after 8 hours reaction. With mesoporous 2-line ferrihydrite, α-Fe_2O_3, and γ-Fe_2O_3 catalysts, 100% of dyes can be degraded within 8 hours of reaction time. Among them, the mesoporous 2-line ferrihydrite was the most efficient catalyst. This catalyst can achieve 100% degradation of dyes within 3 hours. Mesoporous γ-Fe_2O_3 can degrade the dyes completely within 5 hours. The half-life of the dyes which are catalyzed by commercial Fe_2O_3 is 3 hours whereas the half-life of the dyes which were catalyzed by mesoporous α-Fe_2O_3 is 2 hours. In the case of the mesoporous Fe_3O_4 catalyst, there is a small platform at the beginning of the reaction, as shown in Figure 23. In the first 2 hours of the reaction, the dye contents change very little with only 5% degraded. After an 8 hour reaction, mesoporous Fe_3O_4 is able to degrade 80% of orange II dyes.

Figure 24 shows the pseudo-first-order kinetic plot of dye degradation reactions by mesoporous iron oxides. The corresponding apparent reaction rate constants of dye degradation reactions with iron oxides catalysts are listed in Table 6. The apparent rate constant of α-Fe_2O_3 is twice as much as that of commercial Fe_2O_3 and apparent rate constant of γ-Fe_2O_3 is four times as much as that of commercial Fe_2O_3. Moreover, the apparent rate constant of 2-line ferrihydrite is six times more than that of commercial Fe_2O_3. These catalysts are much more efficient than commercial Fe_2O_3 in

catalyzing dye degradation of orange II. The turnover frequency (TOF) is defined as the number of molecules of a given product per catalytic site per unit time. Unit surface area of catalyst is used to represent the number of active sites for the calculation of the TOF [124]. Calculated TOF's of iron oxides catalysts are also listed in Table 6.

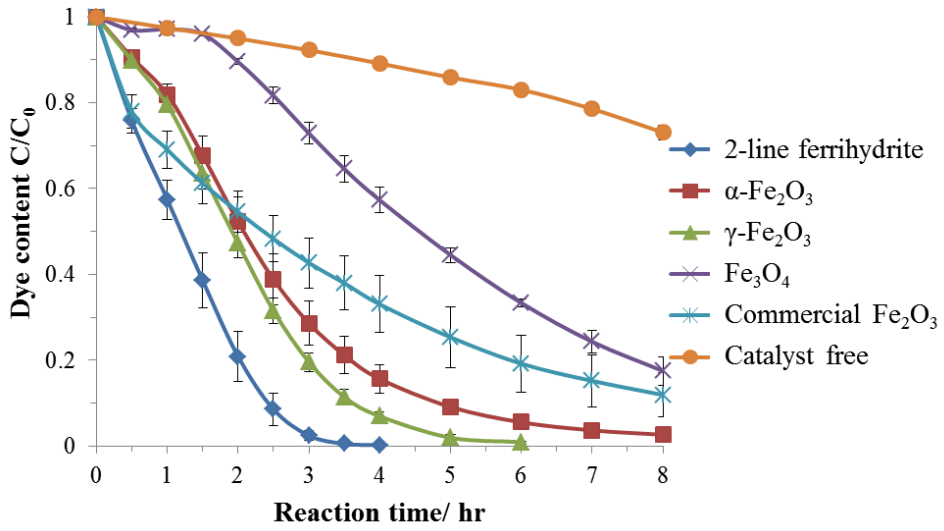

Figure 23: Dye degradation effects by different mesoporous iron oxides.

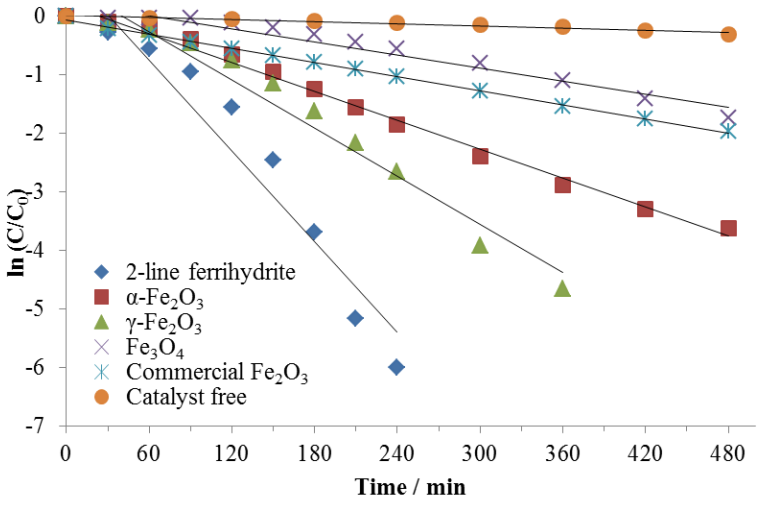

Figure 24: Pseudo-first-order kinetics plot of degradation of orange II by mesoporous iron oxides.

Table 6: First-order kinetic parameters for degradation reactions by mesoporous iron oxides and turnover frequencies of catalysts.

Catalysts	k* (min^{-1})	R^2	Turnover frequencies** $\times 10^{-7}$ mol/(m^2/g*h)
2-line ferrihydrite	0.0258	0.930	1.260
α-Fe_2O_3	0.0082	0.992	0.888
γ-Fe_2O_3	0.0137	0.961	1.960
Fe_3O_4	0.0037	0.952	1.375
Commercial Fe_2O_3	0.0040	0.998	4.236
Catalyst free	0.0006	0.970	N/A

* Apparent rate constant

** Turnover frequency is expressed as (# dye reacted)/(unit surface area)(unit time)

4.2 Stability and recyclability of mesoporous iron oxide catalysts

The performance of recycled mesoporous 2-line ferrihydrite was tested by repeating the catalytic degradation of orange II over mesoporous 2-line ferrihydrite/visible light/H_2O_2 system for 4 times, as shown in Figure 25. The recycle experiments show that the performance of the mesoporous 2-line ferrihydrite catalysts can remain almost unchanged after at least three cycles of degradation reactions. High-angle PXRD pattern of used catalyst shows amorphous nature of catalysts. The appearance of the peak in the low-angle PXRD pattern of the used catalyst indicates that the used catalyst still maintains the meso-structure after the 4^{th} run, as shown in Figure 26 (b). However, the peak in the low-angle PXRD patterns of the used catalyst shifts to lower angles, which means the *d*-spacing of the used catalyst is larger than the fresh catalyst. The structural change of the catalyst could be possibly caused by the residue of carboxyl groups on the surface [3]. For the high angle PXRD patterns, the used catalyst maintains the amorphous nature after the 4^{th} run of the reaction (Figure 26 (a)). Combining the results from Figure 25 and Figure 26, although, in the 4^{th}

cycle, some degree of activity decay of the catalyst appears at the end of the dye degradation reaction, the overall performance of the mesoporous 2-line ferrihydrite catalyst is good in terms of stability during the first three cycle, which is further confirmed by HRTEM (Figure 27).

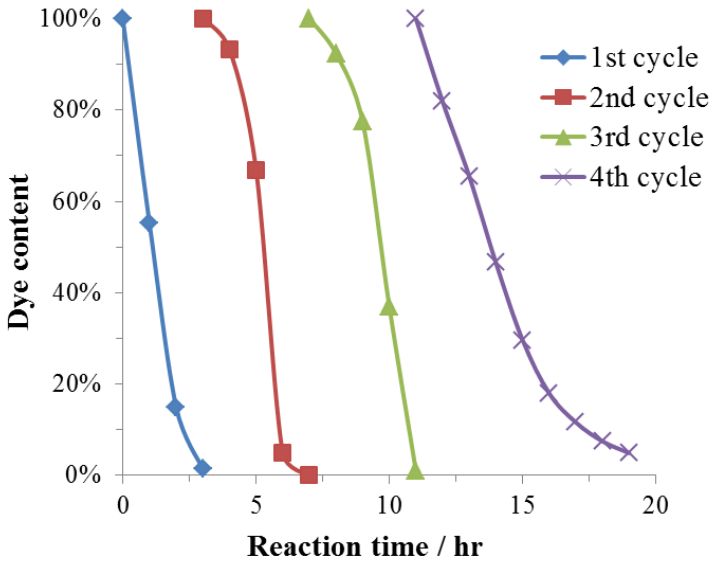

Figure 25: Performance of recycled mesoporous 2-line ferrihydrite catalysts.

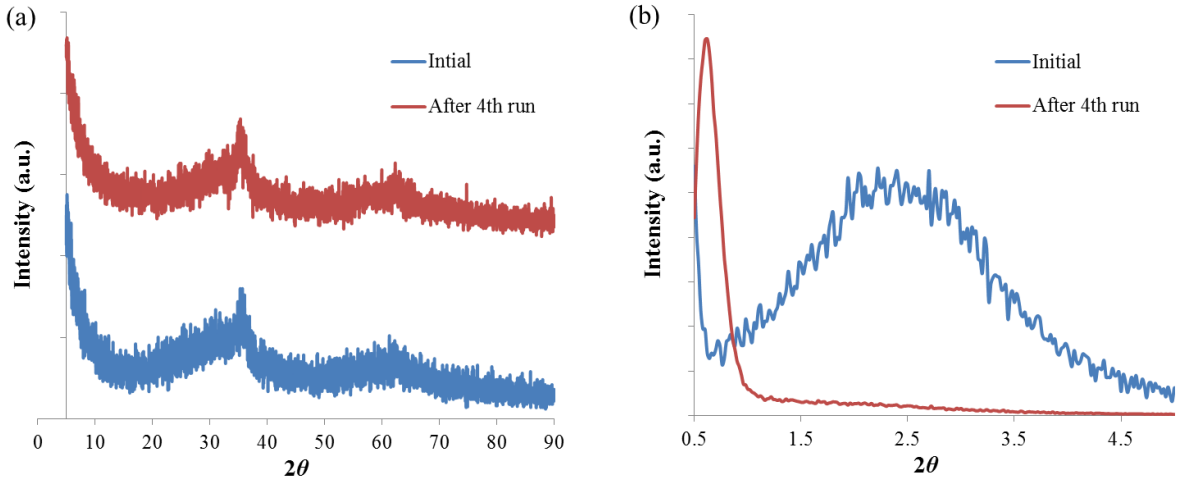

Figure 26: (a) High-angle and (b) low-angle PXRD patterns of recycled mesoporous 2-line ferrihydrite.

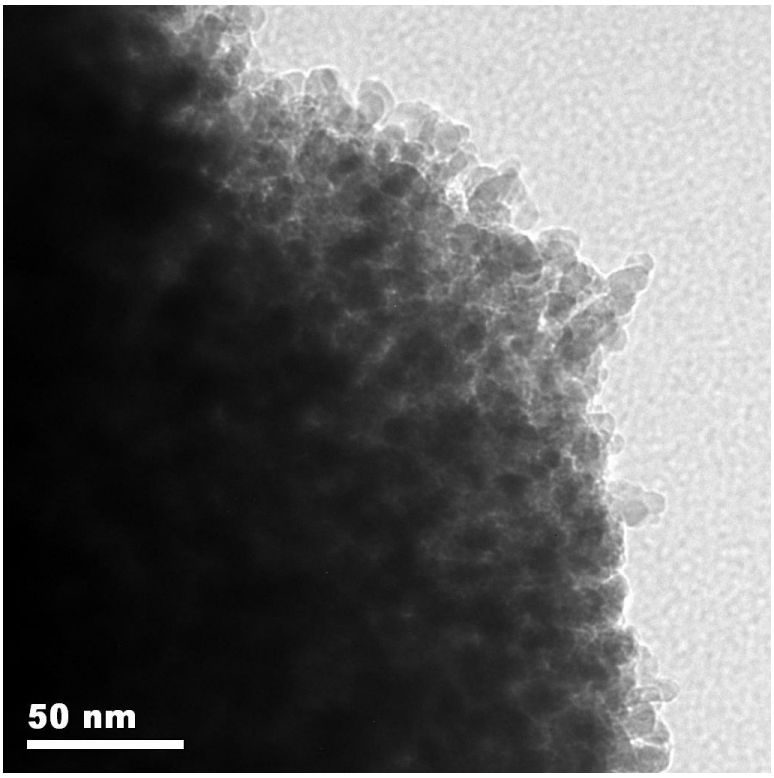

Figure 27: HRTEM image of the mesoporous 2-line ferrihydrite after the 4th cycle of reaction.

4.3 Intermediates of reaction

The initial pH of solution is the intrinsic pH of orange II solution (8.4). However, the pH of the reaction solution is changed during both adsorption in the dark and the reaction. From Figure 28, after adsorption in the dark overnight, the pH values of solutions with Fe_3O_4 and 2-line ferrihydrite decrease significantly to 6.1 and 6.0, respectively, whereas the pH values of solutions with α-Fe_2O_3, γ-Fe_2O_3, and commercial Fe_2O_3 decrease only a little to 8.2, 8.2, and 8.0 respectively. Overall, during the degradation reaction of orange II, the pH values of reaction solutions have a decreasing tendency regardless of iron oxide catalyst types and properties. For experiments with 2-line ferrihydrite, the pH of the solution drops dramatically to 4.4 as soon as the degradation reaction time reaches 0.5 hour. During the process of degradation, the pH of the solution with 2-line ferrihydrite is always the lowest. After the reactions, the pH of mesoporous Fe_3O_4 changes from

6.1 to 4.4, while the pH values of solutions with α-Fe_2O_3, γ-Fe_2O_3, and commercial Fe_2O_3 drop to 6.1, 5.1, and 5.3, respectively. The drop of pH caused by degradation products is consistent with the literature[33].

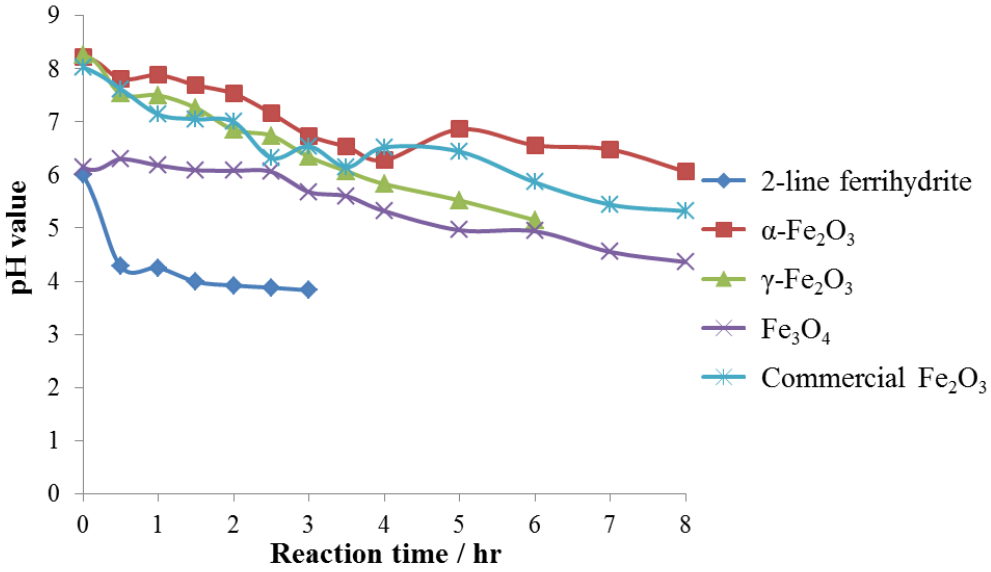

Figure 28: pH values of reaction solutions on different mesoporous iron oxides.

ESI/MS characterization of the reaction solutions catalyzed by 2-line ferrihydrite and commercial Fe_2O_3 are shown in Figure 29 (a) and (b), respectively. The degradation reaction of orange II usually starts from hydroxyl radicals attacking -N=N- functional groups. So the intermediate products after the first step dye degradation reaction are fragments with *m/z* 187 and 157. A large amount of 50-150 *m/z* fragments appearing right after reaction begins (0.5 hour) with 2-line ferrihydrite while with commercial Fe_2O_3, they appear at the half time of the reaction (4 hours). In addition, in Figure 29 (a), the initial fragment from orange II (*m/z*=327) disappears after 1 hour reaction time and the fragment (*m/z*=187, contains a naphthalene ring) after the first step degradation disappears after 2.5 hour reaction time. However, in Figure 29 (b), with commercial

Fe_2O_3, the initial fragment from orange II (*m/z*=327) does not disappear until the end of the reaction. When the dye degradation reaction is catalyzed by mesoporous 2-line ferrihydrite, large *m/z* fragments with the aromatic rings after the first-step degradation are quickly reacted to produce other small *m/z* compounds (appears from the very beginning of the degradation reaction) by possible reactions of being attacked by hydroxyl radicals. In summary, mesoporous iron oxides show better performance than commercial Fe_2O_3, not only on the aspect of higher reaction rate constant but also being able to quickly degrade dyes into smaller species by breaking aromatic rings.

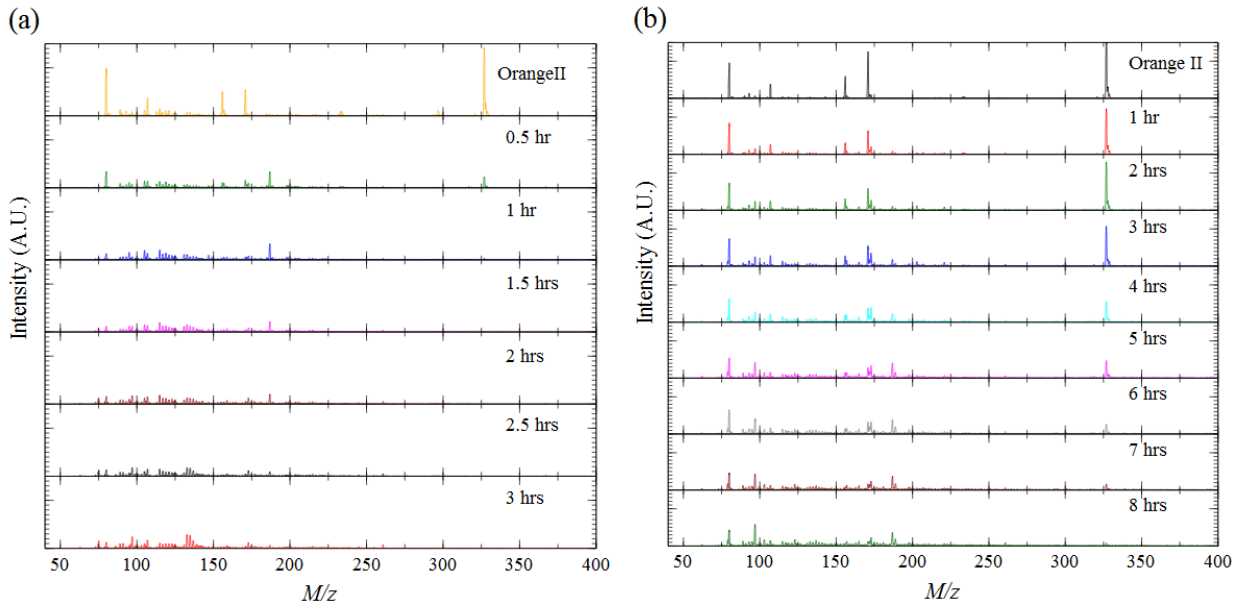

Figure 29: ESI/MS plots of reaction solutions over (a) mesoporous 2-line ferrihydrite and (b) commercial Fe_2O_3. (The intensity of each plot has been adjusted to the same scale.)

4.4 Discussion

4.4.1 *Structure of mesoporous catalysts*

During the synthesis of mesoporous iron oxides, reaction temperature is a critical parameter, since inverse micelle formed by surfactant species serves as a nanoreactor in our sol-gel-based inverse micelle method [3]. At a higher reaction temperature, the formation of carboxyl groups from the surfactant has the possibility of resulting in partially deforming the inverse micelles. According to this, when higher reaction temperature (100 °C) is used for synthesizing mesoporous γ-Fe_2O_3, the pore volume of γ-Fe_2O_3 is smaller than that of 2-line ferrihydrite due to decomposition of surfactants. This explains the result of Figure 7 (a), where γ-Fe_2O_3 shows only a small hysteresis loop. The uniformity of the nanocrystalline distribution is achieved through a short nucleation period that produces all the particles obtained at the end of the reaction.

During the synthesis procedure, for the late transition metal oxides such as Mn, Fe, and Co, the adsorbed NO_x and carboxyl species on the materials are concerns for these systems because they have the possibility of forming multiple oxidation states [3]. In our iron oxide case, the as-synthesized iron oxides possibly have an *in-situ* redox reaction with NO_x and carboxyl species at a higher reaction temperature (100 °C) because of increased oxidation potential of NO_x and carboxyl species when the temperature is increased. On the other hand, at a lower reaction temperature (95 °C), there would be less chance for the redox reaction to take place which could form iron (III) oxide with higher oxidation states. Higher reaction temperatures such as 105 °C and 110 °C have also been tried during the experiment. However, these temperatures were not adopted because there was greater chance for the reaction gel to dangerously splash out when the reaction almost reached the end. When heated in a nitrogen atmosphere, Fe(II) species could be

kept to form Fe_3O_4 while Fe(II) species were oxidized back to a higher valence when calcined at 250 °C in an air atmosphere. The formation of different phases of iron oxide nanoparticles has been observed in the literature [125,126] during low temperature sol-gel syntheses. In order to obtain more information about the surface hydroxyl and carboxyl groups, TG-MS analyses of all the synthesized mesoporous materials and commercial Fe_2O_3 were performed and are shown in Figure 30. Although carboxyl groups on mesoporous iron oxides can be mostly removed by heating at 150 °C for 12 h and followed by heating at 250 °C for 4 h [3], some residues of carboxyl groups are observed on mesoporous 2-line ferrihydrite and Fe_3O_4. These residues of carboxyl groups may cause the structure of mesoporous 2-line ferrihydrite and Fe_3O_4 materials to be unstable while the structure of mesoporous α-Fe_2O_3, γ-Fe_2O_3 and commercial Fe_2O_3 may not be affected by carboxyl group residues.

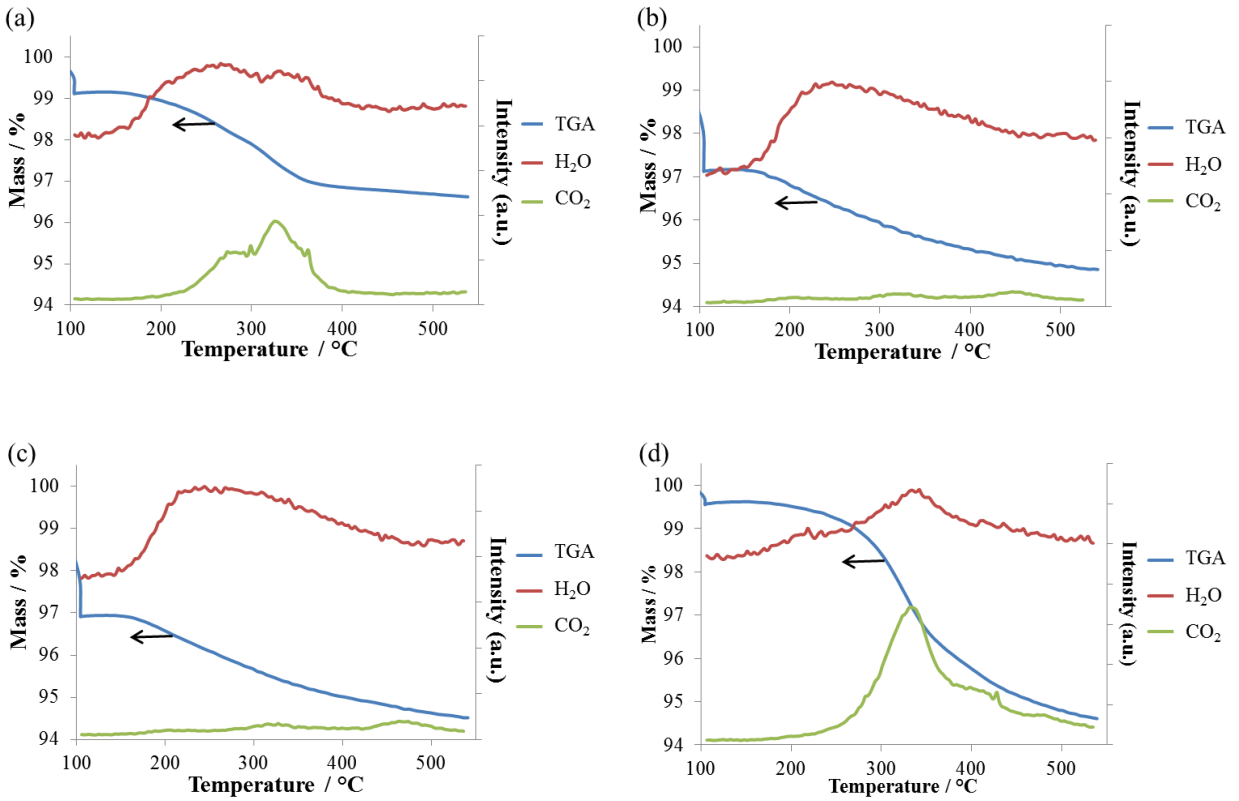

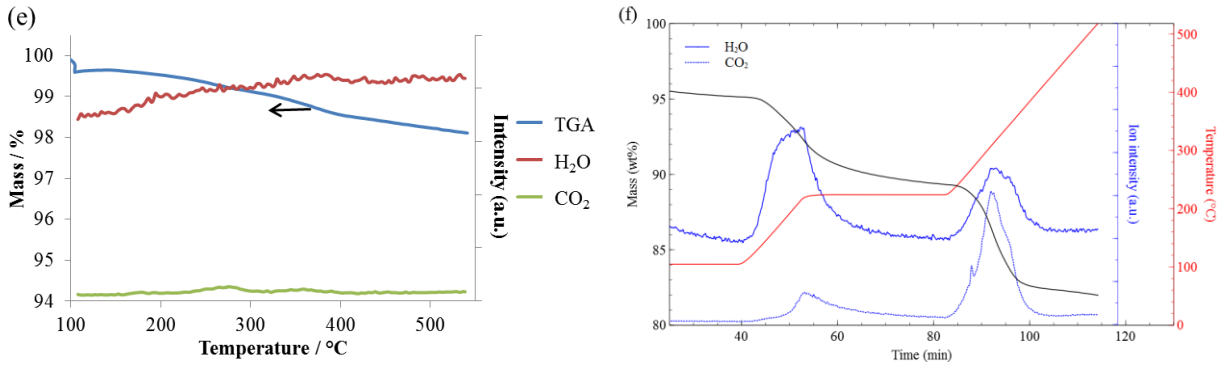

Figure 30: TG-MS analyses of mesoporous (a) 2-line ferrihydrite (b) α-Fe_2O_3 (c) γ-Fe_2O_3 (d) Fe_3O_4 (e) commercial Fe_2O_3 (f) 2-line ferrihydrite. (The temperature profile of (f) is different than (a)-(e) and it is drawn in Figure S1(f).)

4.4.2 *Adsorption properties*

The adsorption capacities (mg dye/g catalyst) of mesoporous iron oxides in this study are greater than commercial Fe_2O_3 (shown in Figure 22) mainly due to the large surface area of mesoporous iron oxide. The mesoporous iron oxides synthesized in this study with small crystalline nanostructure could have more than three times adsorption capability of orange II compared with those (~17.5 mgL^{-1}) synthesized using conventional precipitation methods, when the orange II concentration was around 0.1 mM [127]. Furthermore, the adsorption capability of orange II would become even higher when the pH (pH=8.4 in this study) is adjusted to be as low as what is used in the literature (pH=6.5) [128]. Other competitive catalysts come from flower-like α-Fe_2O_3, γ-Fe_2O_3, and Fe_3O_4 with 3D ordered nanostructures, which were also synthesized by a self-assembly process. They could perform an average removal capacity of around 43.5 mg orange II g^{-1} [125]. The experiments in this study show that the average adsorption capability of mesoporous α-Fe_2O_3 is 37.5 mg orange II g^{-1}; that of mesoporous 2-line ferrihydrite is 49.3 mg/g. Both of them are comparable with literature values. But the adsorption capability of γ-Fe_2O_3 and Fe_3O_4 are lower

than the average removal capacity from the literature. The adsorption capability of iron oxides synthesized in this study is roughly in agreement with and can be generally reflected by the trend in surface area as reported in the literature.

The adsorption mechanism of dyes on iron oxides is proved by B. Saha et al. in a recent report [129]. They reported that preferable and enhanced adsorption phenomena of the dyes contains hydroxyl (-OH) groups on iron oxide nanoparticles with hydroxyl groups on the surface. The formation of hydrogen bonds will shift the frequency of hydroxyl vibrations (in the 3000-3500 cm^{-1} range) to lower wavenumbers after dye absorption on the iron oxide nanoparticle surface. The IR shifts due to hydrogen bond formation are also observed on our mesoporous iron oxides. In Figure 31, the vibrational band of hydroxyl group of orange II dye occurs at 3440 cm^{-1}. After orange II adsorbed on the iron oxide catalysts, the peaks of hydroxyl groups of orange II adsorbed on mesoporous 2-line ferrihydrite, α-Fe_2O_3, γ-Fe_2O_3, Fe_3O_4, and commercial iron oxide shifted from 3440 cm^{-1} to 3435 cm^{-1}, 3428 cm^{-1}, 3435 cm^{-1}, 3419 cm^{-1}, and 3438 cm^{-1}, respectively. This is clear evidence of direct hydrogen bonding formation between hydroxyl groups of orange II and the surfaces –OH group of iron oxides. Moreover, comparing with the red shifts on commercial Fe_2O_3, there are larger red shifts of –OH bonds adsorbed on mesoporous 2-line ferrihydrite, α-Fe_2O_3, γ-Fe_2O_3, and Fe_3O_4. The longer red shifts indicate stronger elongation of O-H bonds which is caused by stronger attractive interactions between positive H and iron oxide surfaces [130]. This means the bonding between mesoporous iron oxides and orange II is stronger than that between commercial Fe_2O_3 and orange II. This causes a preferable adsorption of orange II on mesoporous iron oxides compared with the commercial Fe_2O_3.

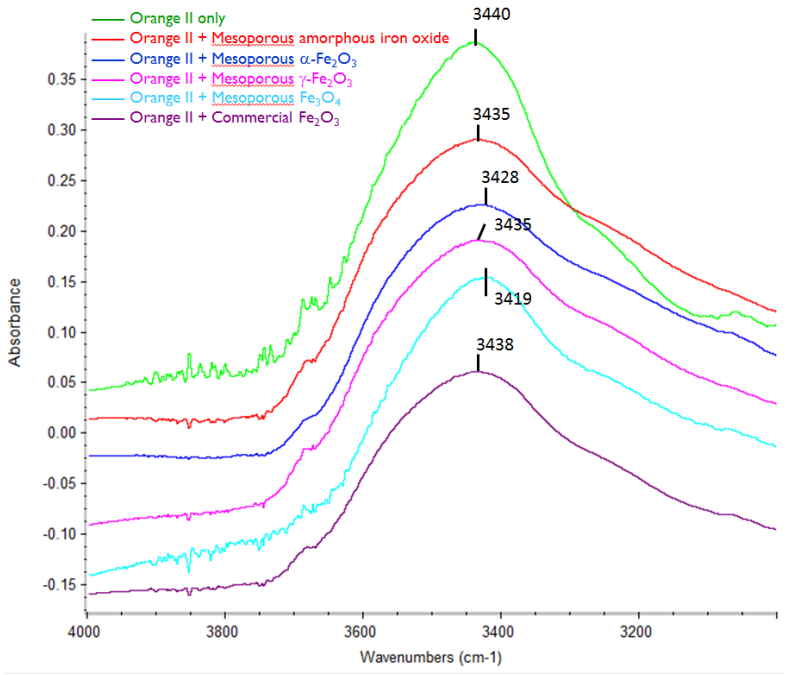

Figure 31: Infrared spectra of hydroxyl stretching of orange II adsorbed on iron oxides.

Another adsorption mechanism of dyes on iron oxides was proposed by J. Bandara et al. in their studies [131,132]. They showed that sulfonic groups of orange II precipitated the adsorption on iron oxide surface by the formation of an unidentate complex with oxide surface. They observed an SO_2 symmetric peak at 1190 cm^{-1} and an asymmetric peak 1305 cm^{-1} disappeared after adsorption. Similar observations were reported in the literature. Figure 32 (a) shows infrared spectra of orange II adsorbed on mesoporous 2-line ferrihydrite, mesoporous α-Fe_2O_3, and commercial Fe_2O_3 compared with free orange II. After being adsorbed on catalysts, the asymmetric stretching peak (1191 cm^{-1}) of -SO_2 is missing since -SO_2 groups are attached on the catalysts after adsorption. Peaks at 1405 cm^{-1} and 1318 cm^{-1} on the spectra of mesoporous 2-line ferrihydrite also disappear. These two peaks represent the bending –OH deformation. This means that adsorption of orange II on mesoporous 2-line ferrihydrite may restrict the –OH bending deformation which leads to a possibility that –OH is on another binding site when adsorbed on mesoporous 2-line

ferrihydrite. On one hand, additional sites of adsorption may make the position of the adsorbed molecules “more fixed”. On the other hand, additional sites of adsorption may give the adsorbed molecules extra strain by possibly changing the bond angle and bond length. Both effects caused by additional sites of adsorption will cause the adsorbed molecules to be attacked more easily by the hydroxyl radical. So with an increase in overall energy, adsorbed molecules will become much more unstable. Figure 32 (b) shows infrared spectra of orange II adsorbed on mesoporous γ-Fe_2O_3 and Fe_3O_4 compared with free orange II. The peak at 1160 cm^{-1} and broad peak at the 1230 cm^{-1} are due to aromatic =C-H bending. This is because crystal structures of γ-Fe_2O_3 and Fe_3O_4 are both cubic close packed while the crystal structures of mesoporous 2-line ferrihydrite and γ-Fe_2O_3 are both hexagonal close packed.

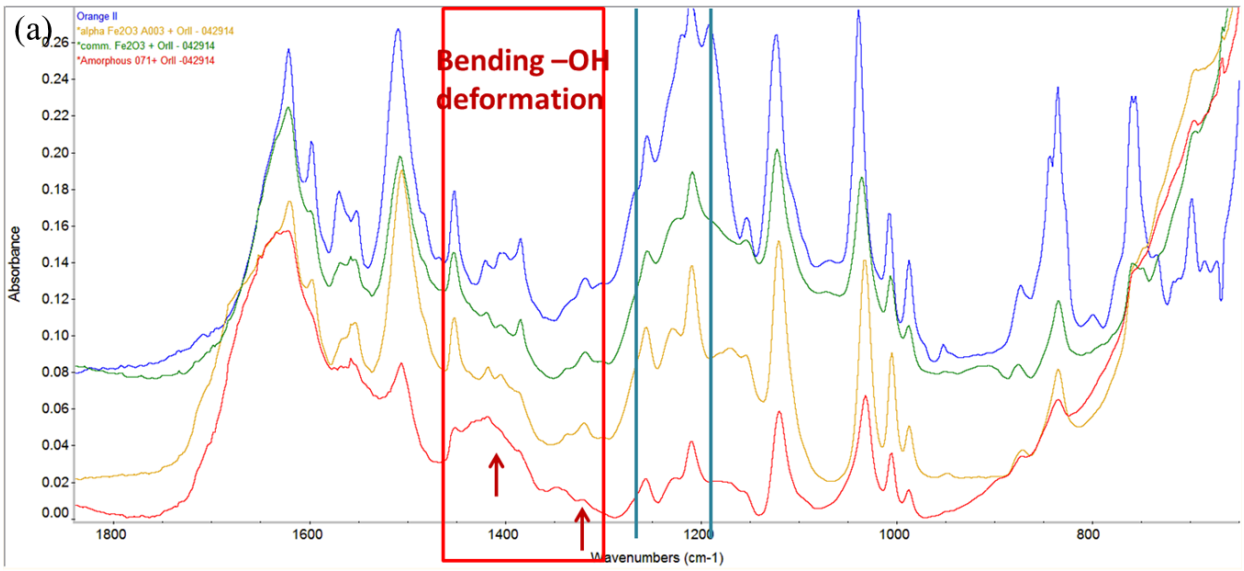

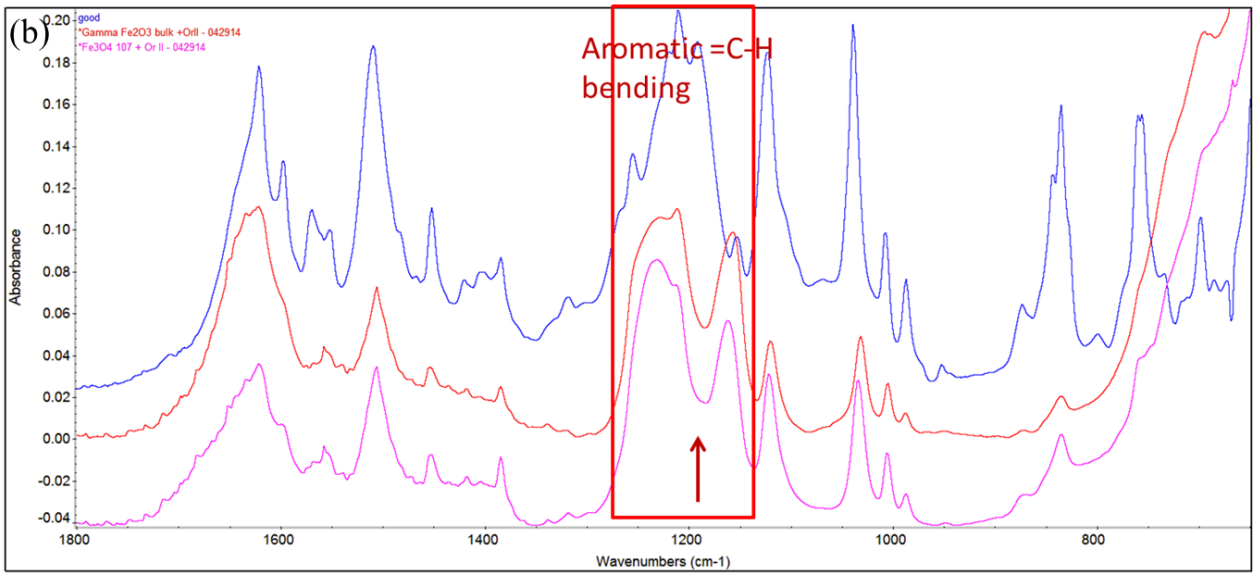

Figure 32: FTIR spectra for orange II and orange II adsorbed on mesoporous iron oxides.

4.4.3 *Catalyst performance*

For the catalytic degradation of orange II under visible light in the presence of H_2O_2, all the mesoporous iron oxides have higher rate constants than commercial iron oxide as Fenton catalysts. Furthermore, the reaction catalyzed by mesoporous 2-line ferrihydrite has the highest rate constant. The major reason for the excellent performance of the mesoporous iron oxides is that they contain large surface area (Table 2), which will provide more available sites for orange II to adsorb on and for H_2O_2 to produce highly reactive hydroxyl radicals. The TOFs of mesoporous iron oxides (Table 6) are smaller than that of commercial Fe_2O_3. Since TOF is calculated by the number of moles of dye degraded per unit surface area per hour, the calculated TOF number of mesoporous iron oxides is neutralized by the large surface areas of mesoporous iron oxides. This indicates that the major advantage of mesoporous iron oxides is their large surface area. Although the mesoporous structure in the catalysts could help to promote the diffusion of reactants, the transportation of reactants to the active sites may be still limited by the size of the dyes and morphology of the

catalysts. The amorphous transition metal oxide has markedly different catalytic activity in photochemical reactions compared with highly crystallized transition metal oxides [133]. The high photochemical activity of amorphous transition metal oxides could be due to highly disordered packing, oxygen vacancies, small particle sizes, and high surface areas. In this study, the high activity of mesoporous 2-line ferrihydrite (amorphous in high-angle PXRD) in dye degradation could be attributed to a variety of factors, such as large surface area, surface hydroxyl groups, acidic products or possible additional adsorption sites.

The rate constants of mesoporous iron oxides catalysts are comparable with those of iron oxides in the literature under mild reaction conditions, such as visible light and neutral pH. Table 7 summarizes the previous work regarding degradation of orange II using different iron oxides catalysts. All the literature data discussed here had the assumption of pseudo-first-order kinetics for the dye degradation process. Feng et al. [31] reported degradation of orange II using different catalysts, including bentonite-clay-based Fe nanocomposite (Fe-B) and α-Fe_2O_3 in the presence of H_2O_2 at pH=6.6 under UV light. Taking advantage of UV light, they obtained faster reaction kinetics, compared to this study, with their catalysts, for example, k_{app}=0.077 with Fe-B nanocomposite and k_{app}=0.063 with α-Fe_2O_3. The research from Du et al. [127] included effect of H_2O_2 on photodegradation orange II by different iron oxides, α-Fe_2O_3, γ-Fe_2O_3, and Fe_3O_4 under UV light at a neutral pH=6.5. Apparent rate constants on different iron oxides in their study were at least 50% smaller than the apparent rate constant shown in this study. As far as visible light is concerned, Cheng et al. [32] synthesized Fe (III) iron exchange resin as a catalyst for the degradation of various dyes including orange II in the presence of H_2O_2 at pH=6.0 under visible light. The catalyst degraded less than 5% orange II after 700 min irradiation whereas the mesoporous 2-line ferrihydrite in this study can degrade 100% orange II within 180 min. Du et al.

[33] synthesized clay-supported iron oxide with different ratios of clay and Fe_2O_3 as catalysts for cationic and anionic dyes including orange II at pH=6.5 under visible light. Very good performance is observed by samples containing 20% Fe_2O_3 (20FeC in the literature). The 20FeC catalysts can degrade 65% orange II in 150 min. In comparison, mesoporous 2-line ferrihydrite catalyst can degrade 90% orange II in 150 min. Furthermore, as shown in the literature [21,134], increasing the amount of catalyst amount can largely increase the rate of dye degradation. The catalyst amount used in their study is twice as large as the catalyst amount used in this study.

Table 7: Effectiveness of iron oxide catalysts on azo dye degradation in the literature.

	Dye	Dye conc.	Catalyst	Catalyst conc.	Light source	H_2O_2 conc.	pH value	Time for total conv.	k_{app} (min^{-1}) $\times 10^{-3}$*
[31]	Orange II	0.2mM	Fe-B	1 g/L	UV	10mM	6.6	120 min	77
			α-Fe_2O_3						63
[127]	Orange II	0.1mM	α-Fe_2O_3	0.5 g/L	UV	1.2mM	6.5	-	8
			γ-Fe_2O_3						14
			Fe_3O_4						11
[32]	Orange II	0.1mM	Fe(III)-loaded resin	0.02g/L	Visible	2.5mM	6.0	>>700min	-
[33]	Orange II	0.2mM	Fe_2O_3/Clay	0.5g/L	Visible	2.0mM	6.5	-	4.9
This study	Orange II	0.1mM	2-line ferrihydrite	0.25g/L	Visible	12.5mM	Neutral	180min	26

* best reported k_{app} is used in this table - Not available

4.4.4 *Mechanism*

In order to distinguish the photo Fenton process and the semiconductor mediated photocatalytic reactions, we proposed an experiment which uses mesoporous 2-line ferrihydrite as the catalyst to degrade orange II without the presence of H_2O_2 under visible light in ambient air. The other conditions, such as catalyst concentration, dye concentration, and power of visible light, are kept the same as the reaction conditions used in this paper. The result is shown in Figure 33. The dye content only drops a little bit after 4 hours irradiation with visible light. Further comparisons of

the UV-Vis spectra of the original dye, degraded dye in the presence of H_2O_2 and the dye after experiments without H_2O_2 are shown in Figure 33 (b). The dye in the experiment without H_2O_2 has not been degraded, showing different characteristics in UV-Vis spectra (~200 nm wavenumber) from the typical degraded dye. This means that the decrease of dye content is mainly caused by adsorption rather than degradation. The reason why this happens is that the mesoporous iron oxide catalyst is not able to generate $O_2^{-\bullet}$ radicals under ambient air conditions under visible light exposure with TiO_2. Therefore, the degradation of dyes on mesoporous iron oxides is contributed by the photo Fenton reaction.

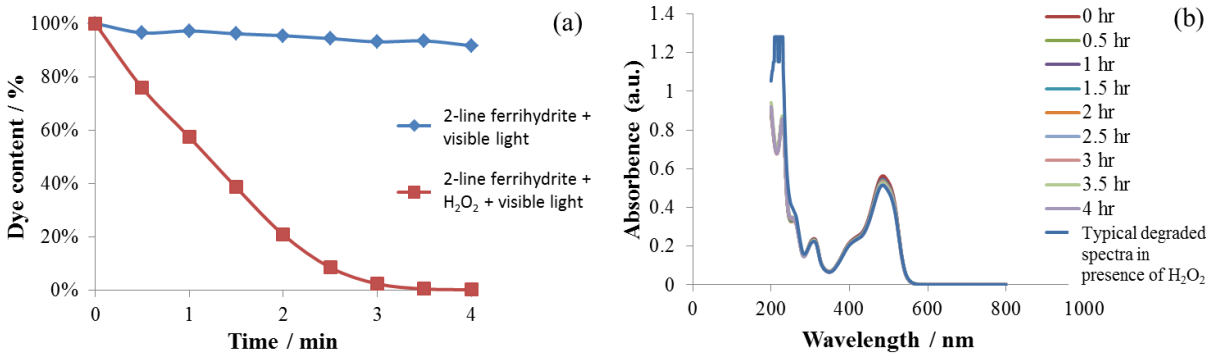

Figure 33: The mesoporous iron oxide mediated dye degradation without H_2O_2 under visible light: (a) dye content vs. time; (b) original UV-Vis adsorption spectra.

The mechanism [18] of Fenton reagents in aqueous solutions is shown as follows:

$$Fe^{2+}(aq) + H_2O_2(l) \rightarrow Fe^{3+}(aq) + OH\bullet(aq) + OH^-(aq) \quad \text{(chain initiation)}$$

$$Fe^{3+}(aq) + H_2O_2(l) \leftrightarrow Fe - OOH^{2+}(aq) + H^+(aq)$$

$$Fe - OOH^{2+}(aq) \rightarrow HO_2\bullet(aq) + Fe^{2+}(aq)$$

$$OH\bullet(aq) + Fe^{2+}(aq) \rightarrow OH^-(aq) + Fe^{3+}(aq) \quad \text{(chain termination)}$$

In the heterogeneous photo Fenton reaction, we believe that a similar mechanism also takes place on the surface of our mesoporous iron oxides. The hydroxyl radicals (•OH) and the hydroperoxyl radicals (•OOH) will react with dyes in solution.

Bandara et al. [135] showed that Orange II could form Fe complexes with iron species in combination with H_2O_2, which is not preferred in basic media. During the degradation of azo dyes, the azo bonds -N=N- are usually firstly broken down [136–138]. The splitting of -N=N- bonds will produce mono-substituted benzene and substituted naphthalene compounds and then the opening of an aromatic ring of substituted naphthalene will form substituted benzene and other acid products [136,139–141]. Similar results were reported in the literature. In Figure 29 (a), the fragments of orange II with *m/z* 327 starts to break down from 0.5 hour. At the same time, the fragments with *m/z* 187 appears, which are products from splitting -N=N- bonds. The fragments with *m/z* 187 are substituted naphthalene compounds. After 1 hour, only weak peaks at *m/z* 327 are observed and the fragments with *m/z* 187, which are the substituted naphthalene compounds, start to break down. A lot of fragments with m/z lower than 150 appear. Table 8 lists observed major peak positions and possible corresponding structures. The appearance of fragments with *m/z* 115 and 121 indicate that substituted naphthalene has been broken down by opening an aromatic ring. This step could form some organic acids. In addition, the pH drop of the reaction solutions also indicates the formation of acid products. So based on ESI/MS and pH analyses, a proposed reaction pathway for orange II degradation over mesoporous 2-line ferrihydrite catalyst is shown in Figure 34. Degradation of orange II starts with azo bonds attacked by hydroxyl radicals to form benzenesolanate and (2-hydroxynaphthalen-1-yl)diazenolate. Then the naphthalene ring in the (2-hydroxynaphthalen-1-yl)diazenolate was attacked at different positions. Breakage of the naphthalene ring at one position can form 2-diazenlyphenol and but-2-enedioic acid. Breakage of

the naphthalene ring at another position can form benzoic acid and 2-hydroxy-3-(2-hydroxydiazen-1-yl)prop-2-enal. The possible breakage position is based on possible appearance of organic acid which causes the drop of pH value of the solution. The formation of organic acid can help the catalyst perform better by adjusting the pH value of the solution to around 4. This will further accelerate mesoporous 2-line ferrihydrite on discoloration and mineralization of orange II. The fragments with low m/z are observed in ESI/MS spectra.

Table 8: Major peaks on ESI/MS spectra and possible corresponding structures.

M/z	Possible structures	*M/z*	Possible structures
187	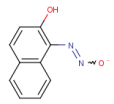	115	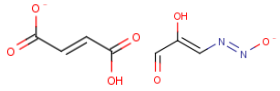
173	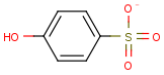	107	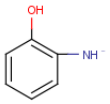
171		105	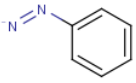
165	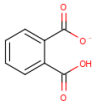	97	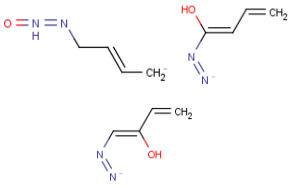
156	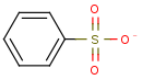	95	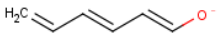
137	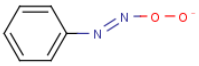	93	
121	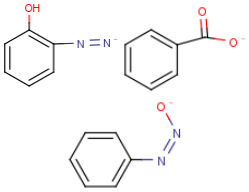	80	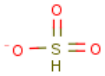

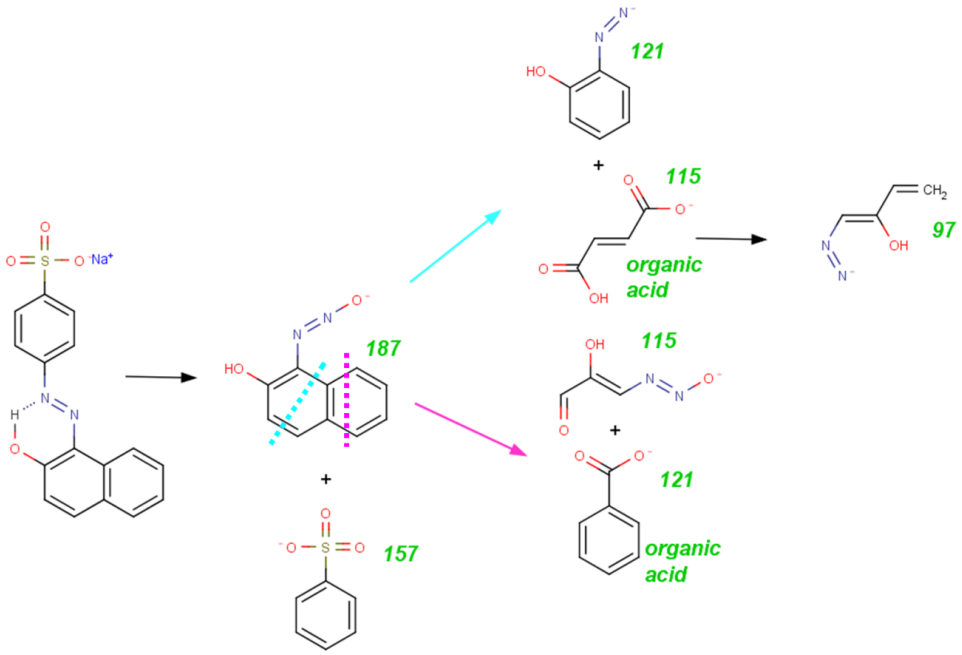

Figure 34: Proposed mechanism of Fenton reactions on mesoporous 2-line ferrihydrite catalyst.

5. APPLICATION OF MAGNETIC IRON OXIDE SUPPORTED PALLADIUM NANOPARTICLES ON NITROBENZENE HYDROGENATION

5.1 Catalyst activity

Figure 35 shows the catalytic conversions of nitrobenzene hydrogenation reactions using 1% Pd/meso-SiO_2-im, 1% Pd/meso-C-im, 1% Pd/comm-Fe_2O_3-im, 1% and 2% Pd/meso-γ-Fe_2O_3-im, and 1% and 2% Pd/meso-γ-Fe_2O_3-os catalysts. Among all the 1% Pd impregnated catalysts, the 1% Pd/meso-γ-Fe_2O_3-im provides a faster reaction rate (100% conversion within 80 min) than 1% Pd/comm-Fe_2O_3-im, 1% Pd/meso-SiO_2-im, and 1% Pd/meso-C-im catalysts. When 1% Pd/comm-Fe_2O_3-im, 1% Pd/meso-C-im, 1% Pd/meso-SiO_2 catalysts are used, 64%, 100%, and 4% conversions of nitrobenzene are reached after 120 min reaction time, respectively. Moreover, the rate of reaction over 2% Pd/meso-γ-Fe_2O_3-im catalyst is greater than that of 1% Pd/meso-γ-Fe_2O_3-im catalyst. For the catalysts synthesized by one-step sol-gel method, 100% conversion is reached within 80 min with the 2% Pd/meso-γ-Fe_2O_3-os catalyst whereas only 76% nitrobenzene is converted after 120 min reaction time when 1% Pd/meso-γ-Fe_2O_3-os catalyst is used. A blank experiment which was performed with intrinsic mesoporous γ-Fe_2O_3 without Pd loading shows that the mesoporous γ-Fe_2O_3 is not active without Pd nanoparticles (Figure 36).

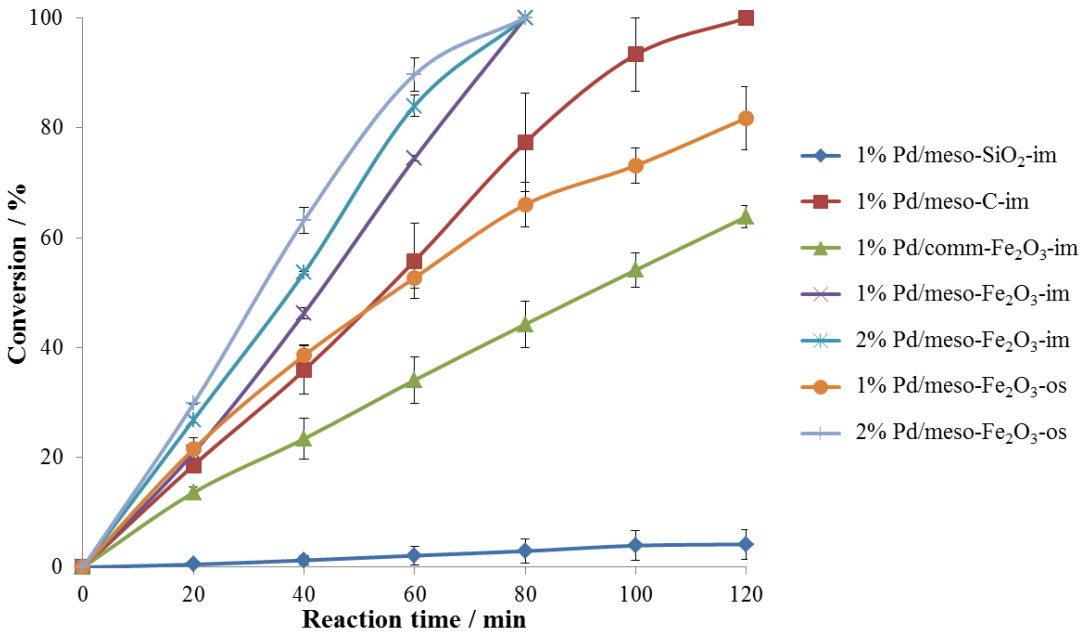

Figure 35: Catalytic performance of catalysts containing Pd synthesized by the impregnation and one-step sol-gel methods for nitrobenzene hydrogenation; inserted is nitrobenzene hydrogenation with mesoporous γ-Fe_2O_3 (without Pd loading).

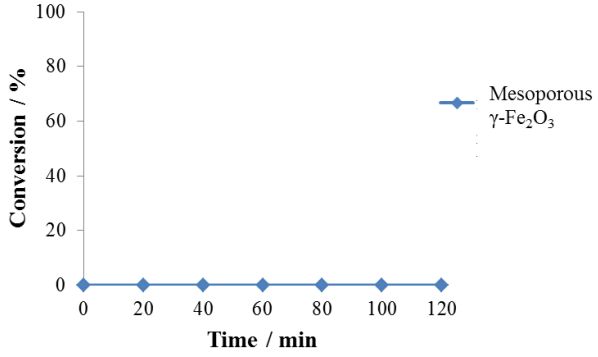

Figure 36: Nitrobenzene hydrogenation reaction by mesoporous γ-Fe_2O_3 without Pd loadings.

Figure 37 shows the turnover frequency (TOF) numbers of 1% Pd/meso-SiO_2-im, 1% Pd/meso-C-im, 1% Pd/comm-Fe_2O_3-im, 1% and 2% Pd/meso-γ-Fe_2O_3-im, and 1% and 2% Pd/meso-γ-Fe_2O_3-os catalysts for the nitrobenzene hydrogenation reaction. The TOF number is defined as the moles of nitrobenzene converted per Pd site per hour. The values in the "bulk" column of EDX data of

Table 4 are used to calculate actual Pd active sites in the catalysts since the amounts of Pd on the surfaces of some catalysts are not available from XPS surveys. The TOF numbers of Pd/meso-γ-Fe_2O_3 catalysts synthesized by the impregnation method (1% Pd/meso-γ-Fe_2O_3-im, TOF 1036 h^{-1}; 2% Pd/meso-γ-Fe_2O_3-im, TOF 498 h^{-1}) and one-step sol-gel method (1% Pd/meso-γ-Fe_2O_3-os, TOF 508 h^{-1}; 2% Pd/meso-γ-Fe_2O_3-os, TOF 598 h^{-1};) are all larger than those of 1% Pd/meso-SiO_2-im (TOF 12 h^{-1}), 1% Pd/meso-C-im (TOF 83 h^{-1}) catalysts, and 1% Pd/comm-Fe_2O_3-im catalyst (TOF 393 h^{-1}) catalysts. Among Pd/meso-γ-Fe_2O_3 catalysts synthesized by the impregnation and one-step sol-gel methods, 1% Pd/meso-γ-Fe_2O_3-im has the largest TOF number. The TOF numbers of 2% Pd/meso-γ-Fe_2O_3-im, 1% Pd/meso-γ-Fe_2O_3-os, and 2% Pd/meso-γ-Fe_2O_3-os catalysts are similar to each other. If the TOF value of our best catalyst, 1% Pd/meso-γ-Fe_2O_3-im, is calculated by the surface Pd content instead of bulk Pd content, the TOF value will be 2166 h^{-1}. This is better than the reported TOF value of 5-Pd/SiO_2 catalyst (292 h^{-1}) from Yan et. al [142] and comparable with the TOF values of Pd/hydrotalcites catalysts (2500 h^{-1}) from Sangeetha et. al [36].

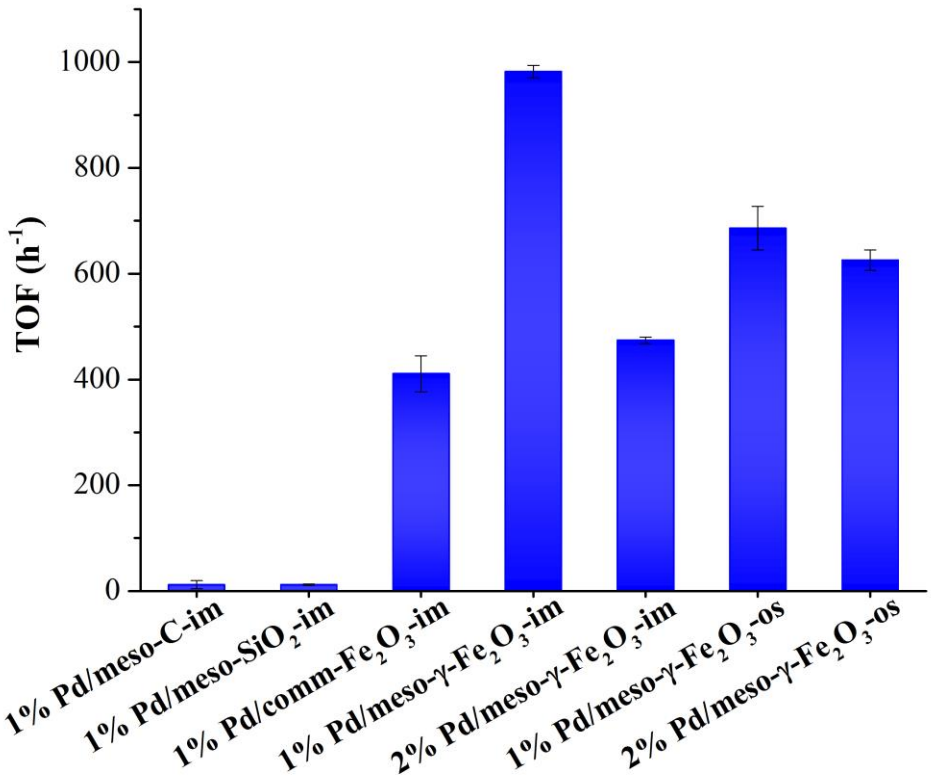

Figure 37: TOF numbers of catalysts containing Pd synthesized by the impregnation and one-step sol-gel methods for nitrobenzene hydrogenation.

5.2 Catalyst recyclability

Figure 38 shows the recyclability of 1% Pd/meso-γ-Fe_2O_3-im, 2% Pd/meso-γ-Fe_2O_3-im, 1% Pd/meso-γ-Fe_2O_3-os, and 2% Pd/meso-γ-Fe_2O_3-os catalysts. With the 1% Pd/meso-γ-Fe_2O_3-im catalyst, only 2% conversion is reached after 120 min in the 2nd cycle of reaction. With the 2% Pd/meso-γ-Fe_2O_3-im catalyst, 61% conversion is reached after 120 min in the 2nd cycle of reaction and only less than 4% conversion is reached after 120 min in the 3rd cycle of reaction. In contrast, Pd/meso-γ-Fe_2O_3 catalysts synthesized by the one-step sol-gel method perform better in recyclability than Pd/meso-γ-Fe_2O_3 catalysts synthesized by the impregnation method. With the 1% Pd/meso-γ-Fe_2O_3-os catalyst, 27% conversion can be reached after 120 min in the 2nd cycle of

reaction and 4% conversion is reached after 120 min in the 3rd cycle of reaction. With the 2% Pd/meso-γ-Fe_2O_3-os catalyst, 100% conversion can be reached within 90 min in the 2nd cycle of reaction while 88% and 50% conversions are reached in the 3rd and 4th cycles of reaction, respectively.

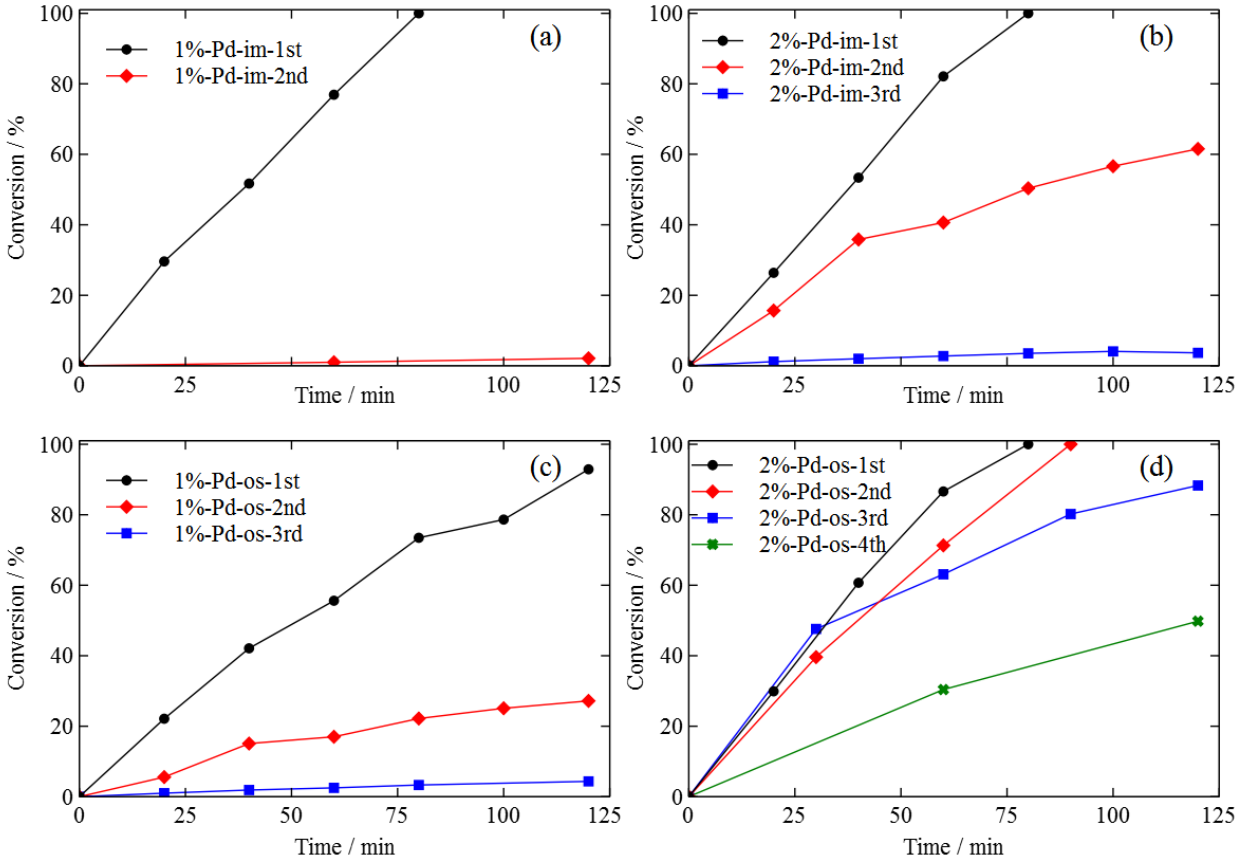

Figure 38: Recyclability of (a) 1% Pd/meso-γ-Fe_2O_3-im catalyst, (b) 2% Pd/meso-γ-Fe_2O_3-im catalyst, (c) 1% Pd/meso-γ-Fe_2O_3-os catalyst, and (d) 2% Pd/meso-γ-Fe_2O_3-os catalyst.

Figure 39 shows the high-angle PXRD patterns of 1% Pd/meso-γ-Fe_2O_3-im, 2% Pd/meso-γ-Fe_2O_3-im, 1% Pd/meso-γ-Fe_2O_3-os, and 2% Pd/meso-γ-Fe_2O_3-os catalysts before and after reactions. The high-angle PXRD patterns were collected from recycled catalysts after the last cycle of recyclability experiments. Consistent PXRD patterns are shown between initial 1% Pd/meso-γ-

Fe_2O_3-im catalyst, 2% Pd/meso-γ-Fe_2O_3-im, 1% Pd/meso-γ-Fe_2O_3-os, 2% Pd/meso-γ-Fe_2O_3-os catalysts and their recycled catalysts. This means all the Pd/meso-γ-Fe_2O_3 catalysts maintain their crystal structures after recyclability experiments.

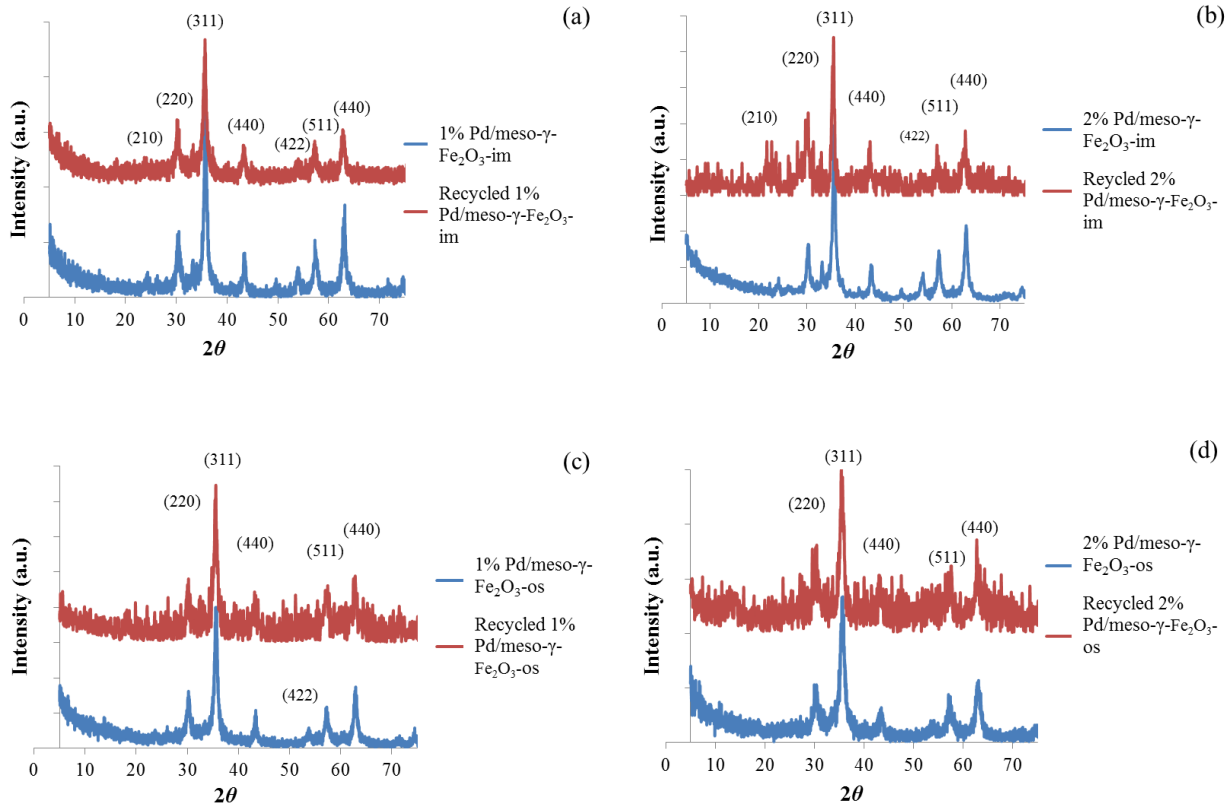

Figure 39: High-angle PXRD patterns of (a) 1% Pd/meso-γ-Fe_2O_3-im catalyst, (b) 2% Pd/meso-γ-Fe_2O_3-im catalyst, (c) 1% Pd/meso-γ-Fe_2O_3-os catalyst, and (d) 2% Pd/meso-γ-Fe_2O_3-os catalyst before and after reaction.

5.3 Discussion

5.3.1 *Structure of catalysts*

From Figure 13, after impregnation, the *d*-spacings of mesoporous SiO_2 and mesoporous carbon catalysts change from 18Å to 27Å and from 32Å to 20Å, respectively. At the same time, there is

a decrease in the surface areas of mesoporous SiO_2 and mesoporous carbon catalysts after impregnation (Table 3). The pore sizes of mesoporous SiO_2 and mesoporous carbon are close to micropores since the mesopore range is 2-50 nm and the micropore range is < 2nm according to IUPAC. The decrease in *d*-spacings of mesoporous SiO_2 and carbon shown in XRD patterns and structural parameters of impregnated catalysts suggests that the Pd nanoparticles accommodate inside the mesopores because a lot of space in the mesoporous network is occupied after impregnation. Since the pore sizes of these materials are small, the impregnation process could affect the structure of the materials. The Pd nanoparticles occupied a lot of space in the micro/mesopores of mesoporous SiO_2 and carbon catalysts. The decrease of surface area of the catalysts synthesized by the incipient wet impregnation method was also observed by Sangeetha et al. [36]. For the 1% Pd/comm-Fe_2O_3-im catalyst, the surface areas and low-/high-angle PXRD patterns are almost the same as the intrinsic commercial Fe_2O_3 catalyst, because the non-porous structure of commercial Fe_2O_3 leads to the existence of Pd nanoparticles on the outer surface. For the Pd/meso-γ-Fe_2O_3-im catalysts, compared with intrinsic mesoporous Fe_2O_3, the pore sizes, surface areas and pore volumes of the structure are preserved because of large pore size of the mesoporous γ-Fe_2O_3 support.

On the high-angle PXRD patterns, all the peaks are retained as well, due to the low Pd loading. However, in low-angle PXRD patterns, the shape of the pattern changes more significantly when more Pd is impregnated on the support. This means the impregnation of Pd will also affect the *d*-spacing of mesoporous γ-Fe_2O_3. For Pd/meso-γ-Fe_2O_3-os catalysts, low-angle and high-angle PXRD patterns stay the same as in the intrinsic mesoporous γ-Fe_2O_3. When the mesoporous γ-Fe_2O_3 catalyst is doped with 1% Pd, the surface areas, pore sizes, and pore volumes of the catalyst remain similar to the intrinsic mesoporous γ-Fe_2O_3. However, when mesoporous γ-Fe_2O_3 is doped

with 2% Pd, the surface areas, pore sizes, and pore volumes become larger than those of intrinsic mesoporous γ-Fe_2O_3. This is attributed to the change of the mesoporous γ-Fe_2O_3 structure caused by the large amount of Pd content. As shown in another study [3], calcination causes the aggregation of nanoparticles, which will result in a decrease of surface area. The large amount (2%) of Pd content prevents the aggregation of iron oxide nanoparticles during the calcination, so the 2% Pd/meso-γ-Fe_2O_3-os catalyst has a larger (118 m^2/g) surface area than the intrinsic mesoporous Fe_2O_3 catalyst. When a large amount of Pd is added into the initial solution, the formation of micelles is disturbed to some extent, which likely makes the micelle formation incomplete. The pores formed from incomplete micelles are not stable. They could merge with other pores during calcination, leading to a larger pore size and pore volume than in the intrinsic mesoporous γ-Fe_2O_3.

The Pd/Fe or Pd/Si or Pd/C ratios in the circled area, in the bulk, and on the surface of all the Pd containing catalysts are shown in Figure 16 and Table 4. For 1% Pd/comm-Fe_2O_3-im and 1% Pd/meso-γ-Fe_2O_3-im catalysts, no region with particularly high Pd/Fe ratio is observed. The Pd nanoparticles in these catalysts are not gathering in a small region of the iron oxide support and are dispersed relatively better than those in other catalysts. For 2% Pd/ meso-γ-Fe_2O_3-im, 1% Pd/ meso-γ-Fe_2O_3-os, 2% Pd/meso-γ-Fe_2O_3-os, and 1% Pd/meso-SiO_2-im catalysts, Pd/Fe or Pd/Si ratios in the circled region are higher than those in the bulk. The Pd nanoparticles are not well dispersed in these supports. Comparing 1% and 2% Pd/meso-γ-Fe_2O_3-im catalysts, the mesoporous γ-Fe_2O_3 cannot impregnate Pd nanoparticles homogeneously when the Pd loading amount is 2%. Comparing 1% Pd/meso-γ-Fe_2O_3-im and 1% Pd/meso-γ-Fe_2O_3-os catalysts, the one-step sol-gel method cannot disperse Pd nanoparticles very well, because, when the Pd/meso-γ-Fe_2O_3 catalysts are synthesized by the one-step sol-gel method, the Pd nanoparticles change the structure of the

iron oxide support, leading to the gathering of Pd nanoparticles in the circled region. For all the Pd containing catalysts except 2% Pd/meso-γ-Fe_2O_3, the Pd/Fe ratios obtained by EDX are similar to those obtained by the XPS data. Pd nanoparticles stay in the bulk of the catalysts rather than gathering on the surface of catalysts. For 2% Pd/meso-γ-Fe_2O_3 catalyst, the Pd/Fe ratio on surface is much higher than that in the bulk. Part of the Pd nanoparticles is ejected out of the iron oxide support during the merging of pores during calcination. The Pd/C ratio in 1% Pd/meso-C-im catalyst is for reference only because of the carbon element in the ambient experiment environment.

5.3.2 *Effect of supports – mesoporous SiO_2, mesoporous carbon, commercial Fe_2O_3 and mesoporous-γ-Fe_2O_3*

Compared with the 1% Pd/comm-Fe_2O_3-im catalyst (Figure 35), 1% Pd/meso-γ-Fe_2O_3-im catalyst has much higher activity in nitrobenzene hydrogenation reactions. Since these two catalysts are both prepared by the impregnation method, the major difference between them exists in the support – one is a mesoporous support and the other is a non-porous support. The higher activity of the 1% Pd/meso-γ-Fe_2O_3-im catalyst is probably due to two reasons related to the mesoporous support: one is that the mesoporous support has a larger surface area, pore size, and pore volume, which can provide more sites and disperse Pd better than the non-porous materials; the other is that the mesoporous support can reduce the mass transport of reactants and/or products [143]. All the catalysts supported on mesoporous γ-Fe_2O_3 in this study have higher TOF numbers than commercial non-porous γ-Fe_2O_3. Compared with 1% Pd/meso-SiO_2-im and 1% Pd/meso-C-im catalysts, the activity of 1% Pd/meso-γ-Fe_2O_3-im catalysts for the nitrobenzene hydrogenation reaction is much higher. This is consistent with Ge et al. [144], who found that the basic sites (oxygen vacancies) of iron oxide support could help palladium catalysts reach higher activity in the glycerol hydrogenolysis reaction. The reason for oxide supported catalysts being more active

in nitrobenzene hydrogenation reaction is possibly due to the large surface area and phases of iron oxide nanoparticles [145,146], or the strong interaction between palladium and iron oxide supports [144,147,148]. It is not fair to compare the Pd/meso-γ-Fe_2O_3-im with Pd/meso-SiO_2-im and Pd/meso-C-im catalysts, because of the significant decrease of surface areas of silica and carbon supports after Pd impregnation. It seems surface area and pore size have significant impact on the catalyst activity. Further studies focusing on the synthesis of Pd impregnated materials (include mesoporous γ-Fe_2O_3, silica, and carbon) with higher surface area and proper pore size are necessary. However, for comparison purposes, the Pd impregnated catalysts are synthesized under identical procedures in this study. The better catalytic performance of iron oxide support might be restricted to the current impregnation method. An exhaustive study on optimizing the synthesis conditions for the Pd impregnated mesoporous γ-Fe_2O_3, silica, and carbon individually and in comparison with their catalytic performance in nitrobenzene hydrogenation may be interesting as future work.

5.3.3 *Effect of preparation method – impregnation method vs one-step sol-gel method*

Comparing the 1% Pd/meso-γ-Fe_2O_3-im and 1% Pd/meso-γ-Fe_2O_3-os catalysts (Figure 35), the TOF number of 1% Pd/meso-γ-Fe_2O_3-im catalyst is almost double that of 1% Pd/meso-γ-Fe_2O_3-os catalyst. This is possibly because 1% Pd/meso-γ-Fe_2O_3-os catalyst has some Pd nanoparticles inside the iron oxide support which are not accessible to reactant. The Pd nanoparticles of 1% Pd/meso-γ-Fe_2O_3-im catalyst stay on the surface of the iron oxide support, which makes them more available for reaction than those inside the iron oxide support. One possible reason for the high TOF number of 1% Pd/meso-γ-Fe_2O_3-im catalyst is that the Pd nanoparticles are well dispersed in the support due to a large pore size and interconnected network of mesoporous γ-Fe_2O_3 (Figure 16, Figure 40 and Table 4). No apparent aggregation of Pd nanoparticles in 1% Pd/meso-γ-Fe_2O_3-im

catalysts occurs (Figure 25 and Table 4). Compared with 2% Pd/meso-γ-Fe_2O_3-im and 2% Pd/meso-γ-Fe_2O_3-os catalysts, the TOF numbers are similar while the low TOF number of 2% Pd/meso-γ-Fe_2O_3-im catalyst is due to the aggregation of Pd nanoparticles in the support; the low TOF number of 2% Pd/meso-γ-Fe_2O_3-os catalyst is because not all the Pd nanoparticles are accessible to reaction which is discussed in detail in Section 5.3.4 Effect of Pd loading amount. Another reason for high activity of 1% Pd/meso-γ-Fe_2O_3-im catalysts could be also due to the leached homogeneous Pd nanoparticles [149,150]. From a recyclability perspective, the one-step sol-gel method helps to improve the noble metal leaching problem which is further discussed in Section 5.3.6 Recyclability of Pd/meso-γ-Fe_2O_3 catalysts.

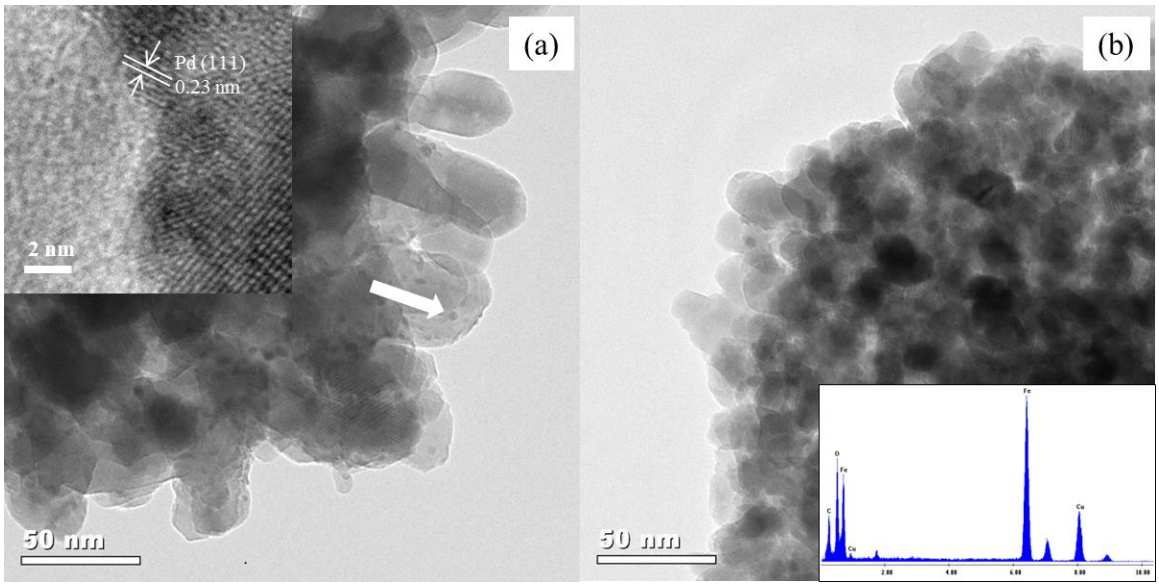

Figure 40: TEM images of 1% Pd/meso-γ-Fe_2O_3-im catalyst (a) before the reaction (inserted is the HRTEM image of Pd nanoparticles) and (b) after reaction (inserted is the EDX pattern of this region.)

5.3.4 *Effect of Pd loading amount*

From Figure 36, the reaction rate of nitrobenzene hydrogenation reaction becomes faster when the Pd amount in the catalysts increases. This is reasonable in the sense that Pd is well-known as an

effective catalyst for reactions related to hydrogen in a variety of reactions [151]. However, in this study, the reaction rate of 2% Pd/meso-γ-Fe_2O_3-im catalyst is only slightly faster than that of 1% Pd/meso-γ-Fe_2O_3-im catalyst. The TOF number of 2% Pd/meso-γ-Fe_2O_3-im catalyst is almost half of that of the 1% Pd/meso-γ-Fe_2O_3-im catalyst. As discussed in Section 4.1, in the 2% Pd/meso-γ-Fe_2O_3-im catalyst, there is aggregation of Pd nanoparticles, which makes not all the Pd nanoparticles accessible for reaction. This is why although the Pd impregnation amount is doubled in 2% Pd/meso-γ-Fe_2O_3-im catalyst, the activity only increases a small amount.

From Figure 36, 2% Pd/meso-γ-Fe_2O_3-os catalyst has better catalytic performance than 1% Pd/meso-γ-Fe_2O_3-os catalyst. However, from Figure 37, the TOF numbers of nitrobenzene hydrogenation reaction on 1% and 2% Pd/meso-γ-Fe_2O_3-os catalysts are similar. This means that the better performance of 2% Pd/meso-γ-Fe_2O_3-os catalyst is mainly due to the larger amount of Pd. Although Pd/meso-γ-Fe_2O_3 synthesized by the one-step sol-gel method cannot disperse Pd nanoparticles homogeneously, the overall effectiveness of Pd nanoparticles in the catalysts is similar.

5.3.5 *Selectivity of Pd/meso-γ-Fe_2O_3 catalysts*

All the Pd containing catalysts used in this study have > 97% selectivity to aniline after reactions, because the reaction mainly follows a direct pathway. The nitrobenzene hydrogenation reaction has two possible reaction pathways [152]: one is the direct route; the other is the condensation route. The direct route of nitrobenzene hydrogenation will occur when the hydrogenation over the catalysts is sufficiently fast to prevent condensation of pheneylhydroxyamine with nitrosobenzene. In the direct route, the reactions catalyzed by the Pd containing catalysts follow this path: nitro compound → (nitroso compound →) hydroxylamine → aniline derivative [153]. In the condensation route, the condensation of hydroxylamine and nitroso intermediates is the step to form impurities. A typical GC spectrum of a sample solution during nitrobenzene hydrogenation reaction is shown in Figure 41. Typical MS spectra of impurities hydroxylamine and N-ethylaniline are shown in

Figure **42.** In the GC spectrum, only trace amounts of hydroxylamine and N-ethylaniline are observed in the reaction solution which are intermediates and products of possible aldol condensation side reactions, respectively [154]. The product of the reaction (aniline) is further confirmed by nuclear magnetic resonance spectroscopy (Figure 44). For side reactions, trace amounts of acetaldehyde in the ethanol solvent react with the product aniline following an aldol condensation reaction mechanism. The product of this aldol condensation reaction is N-ethylideneaniline. Then N-ethylideneaniline is reduced by hydrogen to form N-ethylaniline. The proposed pathways of nitrobenzene hydrogenation and aldol condensation side reaction are shown in Figure 43.

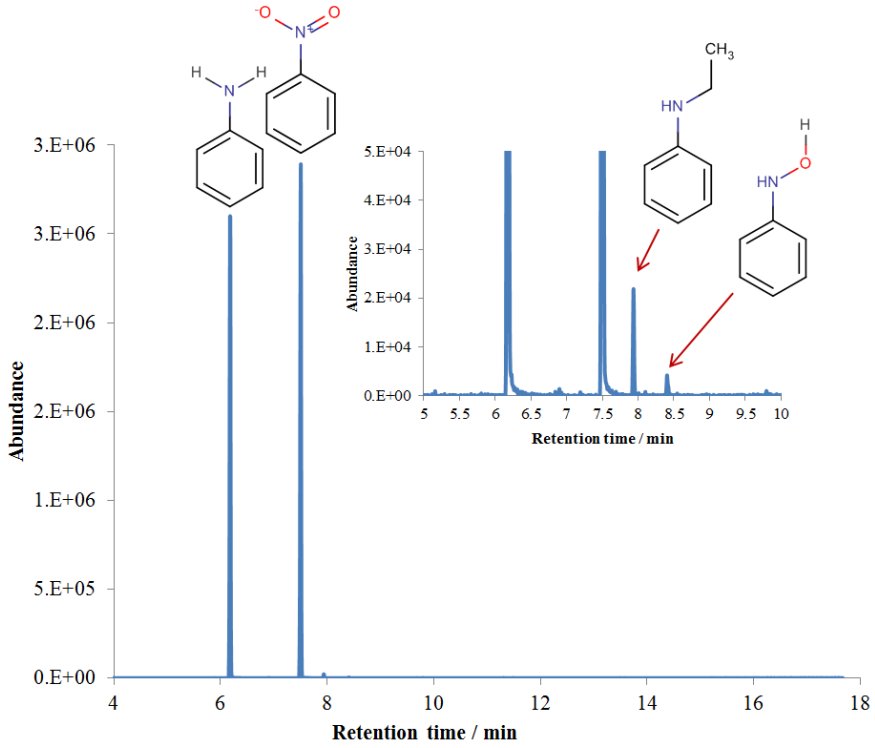

Figure 41: GC spectrum of nitrobenzene hydrogenation reaction over Pd/meso-γ-Fe_2O_3 catalysts and corresponding compounds for the peaks (Inserted spectrum is the zoomed area).

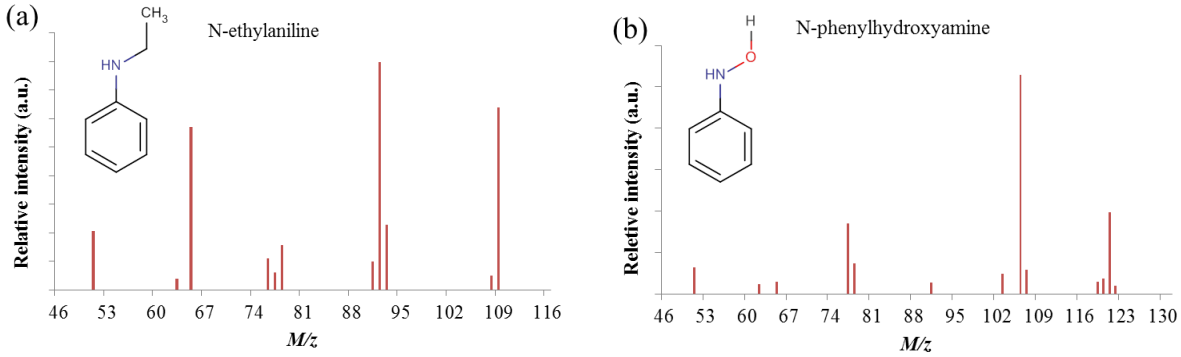

Figure 42: MS spectra of (a) N-ethylaniline (b) N-phenylhydroxyamine.

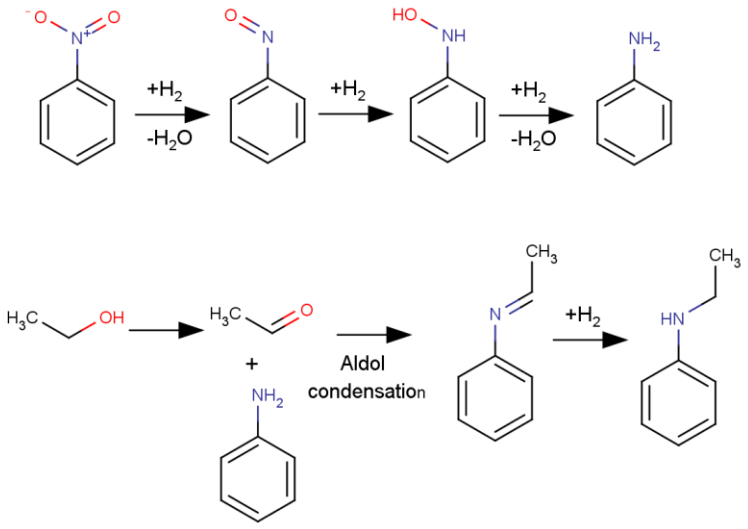

Figure 43: The proposed pathways of nitrobenzene hydrogenation reaction (upper row) and possible side reaction by aldol condensation (lower row).

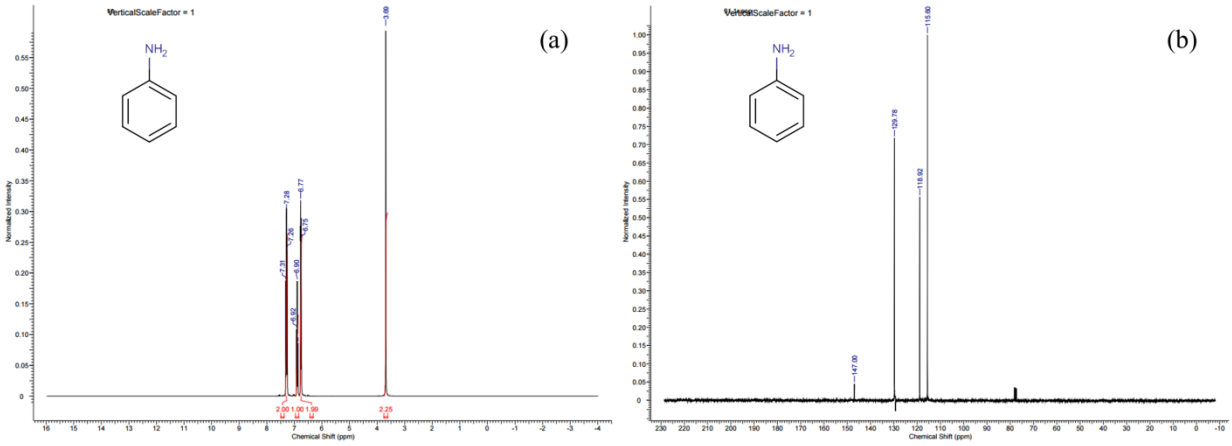

Figure 44: (a) ^{1}H NMR and (b) ^{13}C NMR spectra of product of nitrobenzene hydrogenation reaction by 1% Pd/meso-γ-Fe_2O_3 catalyst.

5.3.6 *Recyclability of Pd/meso-γ-Fe_2O_3 catalysts*

The 1% and 2% Pd/meso-γ-Fe_2O_3-im catalysts have an obvious decay in catalytic performance in the 2nd cycle of reaction (Figure 38 (a) and (b)). This is due to serious leaching of palladium. The leaching problem in this study is confirmed by TEM images. The TEM images of the catalyst with highest TOF values (1% Pd/meso-γ-Fe_2O_3 catalyst) before and after the reaction are shown in Figure 40. Before the reaction, Pd nanoparticles are well dispersed in the iron oxide matrix. The dark spots in Figure 40 (a) are proven to be Pd nanoparticles by matching Pd (111) lattice spacings in the inserted HRTEM images. But after the reaction, there's no evidence of Pd nanoparticles in the selected region (shown in the EDX pattern). This indicates that part of the Pd nanoparticles leached out during the reaction. Agglomeration of Pd nanoparticles on Pd/meso-γ-Fe_2O_3 catalysts cannot be observed by TEM. When the sizes of Pd particles are large, the contrast of the Pd particles becomes similar to those of overlapped iron oxide nanoparticles.

Leaching of the effective metals during experiments has been observed on catalysts synthesized by the impregnation method in many studies [39,43,50,142,155]. In the literature, there are several

approaches that can mitigate leaching from the perspective of modifying synthesis methods. Webb et al. [156] loaded palladium on functionalized mesoporous silica by a grafting approach. The catalysts can be highly active and recyclable for Suzuki–Miyaura coupling reaction under certain reaction conditions. Su et al. [157] synthesized ruthenium nanoparticles by impregnating ruthenium into mesoporous materials then thermally reducing ruthenium to ruthenium nanoparticles. The nanoparticles showed high activity and stability in hydrogenation of monoaromatics with less leaching. Banerjee et al. [49] synthesized Pd-MCM-48 using tetra-n-octylammonium bromide as a capping and stabilizing agent of Pd nanoparticles during typical Stober syntheses of MCM-48. The synthesized catalysts can be used at least ten times for hydrogenation of olefins with minimal loss of activity. Ge et. al [158] synthesized core-shell nanocomposite catalysts using superparamagnetic Fe_3O_4 as a core and protecting noble metal nanoparticles by mesoporous silica shell. The catalysts with protection of mesoporous silica shell showed high activity after 6 cycles of reduction of 4-nitrophenol.

In this study, the one-step sol-gel method is investigated to help mitigate the noble metal leaching problem [159]. With the same Pd loading amount, Pd/meso-γ-Fe_2O_3-os catalysts have better recyclability than Pd/meso-γ-Fe_2O_3-im catalysts. From Figure 38 (d), in the 1st and 2nd cycle of reaction, 100% nitrobenzene is converted within 80 min over 2% Pd/meso-γ-Fe_2O_3-os catalyst. In the 3rd cycle of reaction, although there is some decay in catalytic performance, 88% conversion of nitrobenzene can still be reached after 120 min reaction time over the 2% Pd/meso-γ-Fe_2O_3-os catalyst. Overall, the catalysts synthesized by the one-step sol-gel method can help improve the recyclability of the catalyst compared to the catalysts synthesized by impregnation methods.

6. APPLICATION OF MESOPOROUS ALUMINOSILICATE ON SILOXANE ADSORPTION FOR BIOGAS CLEANUP

6.1 Adsorption capacity of mesoporous aluminosilicates

Figure 45 (a, b) shows breakthrough curves of mesoporous aluminosilicates with different aluminum dopant amounts and different calcination heating rates. D4 breaks through the mesoporous aluminosilicates with Si:Al ratio=5, 10, and 20, and the mesoporous aluminosilicate with 1 °C/min at the very beginning of the adsorption, whereas breakthrough for the mesoporous aluminosilicate with 5 °C/min and 10 °C/min heating rate occurs at around 30 min and 60 min, respectively, implying better adsorption performance.

Adsorption curves of mesoporous aluminosilicates with different aluminum dopant amounts and different calcination heating rates are shown in Figure 46 (a, b). The mesoporous aluminosilicate with a Si:Al ratio=20 saturated at around 120 min while the mesoporous aluminosilicates with Si:Al=5 and 10 saturated at around 220 min. In fact, the aluminum content itself does not affect the adsorption capacities of the materials. Chica et al. [160] found that the adsorption capacity of the zeolite adsorbents was independent of Al content but was influenced by the zeolite structure. As a further contribution, we have correlated the key textural properties of the mesoporous aluminosilicates with the adsorption capacities (See Section 4.1 for the detailed discussion). The mesoporous aluminosilicate with 1 °C/min heating rate saturated at around 160 min while the mesoporous aluminosilicates with 5 °C/min and 10 °C/min heating rates saturated at around 240 min and 260 min, respectively. This is mainly attributed to the higher surface area and pore volume that the mesoporous aluminosilicates can be obtained with faster calcination heating rates.

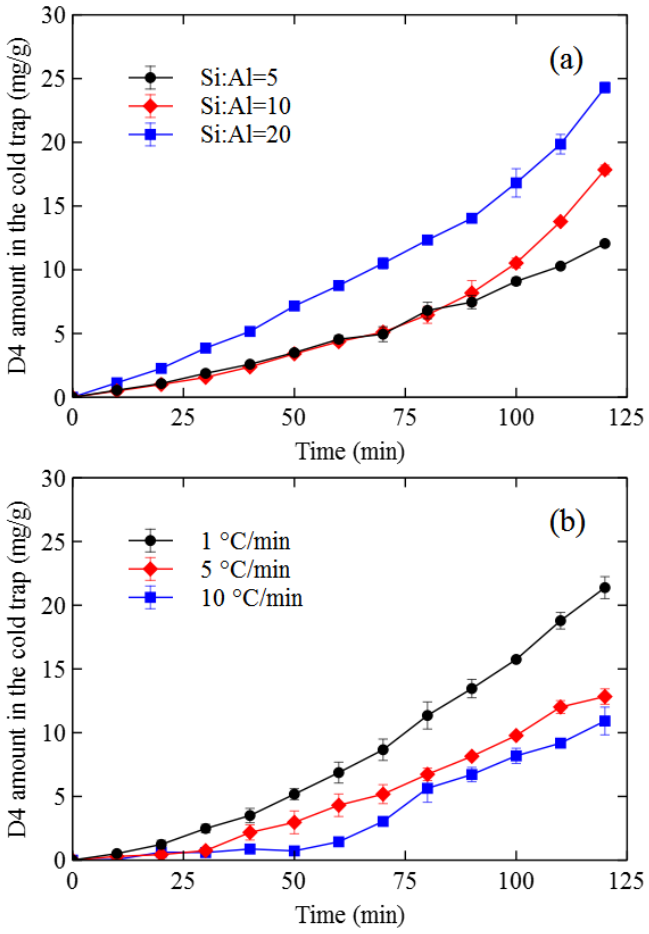

Figure 45: Breakthrough curves on mesoporous aluminosilicates with (a) different aluminum dopant amounts and (b) different calcination heating rates.

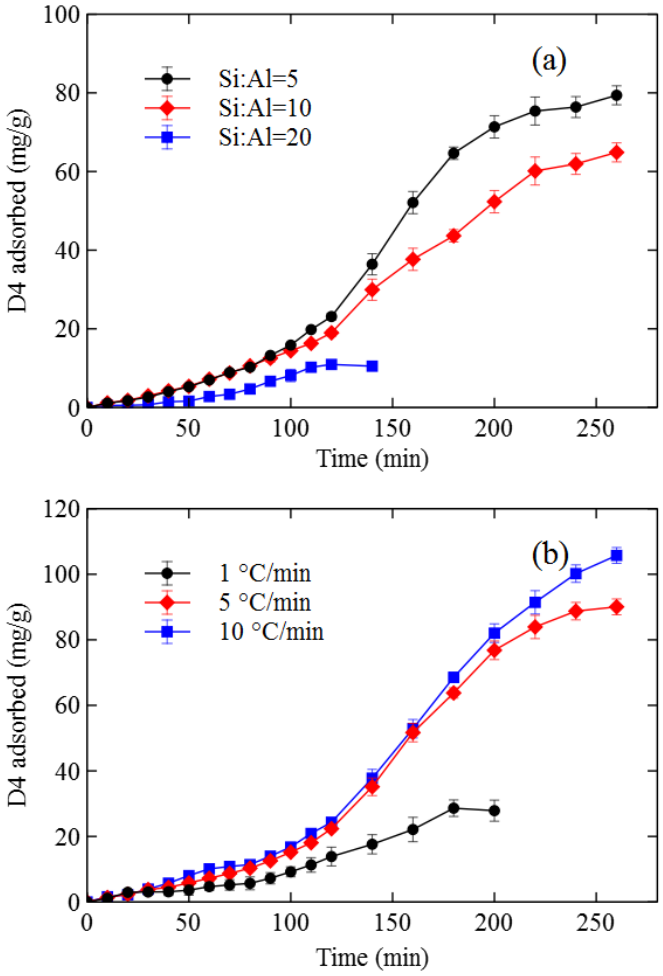

Figure 46: Adsorption curves on mesoporous aluminosilicates with (a) different aluminum dopant amounts and (b) different calcination heating rates.

6.2 Comparison of mesoporous aluminosilicate and ZSM-5 in Siloxane adsorption

In this study, we compared the adsorption performance of mesoporous aluminosilicate with that of microporous aluminosilicate (ZSM-5) to evaluate the effectiveness of utilizing mesostructured adsorbents on D4 adsorption. In order to recognize the true effect of the pore size distribution, we have chosen the mesoporous aluminosilicate (Si:Al=5 and 2 °C/min heating rate) with similar BET surface area, total pore volume, micropore volume, and mesopore volume to ZSM-5 for

comparison (shown in Table 9). The experiments with ZSM-5 have been conducted under the same conditions as those with the synthesized mesoporous aluminosilicates.

Table 9: Textural parameters of mesoporous aluminosilicate and ZSM-5 adsorbents.

	Aluminosilicate*	ZSM-5
BET surface area (m^2/g)	424	419
Total pore volume (cm^3/g)	0.209	0.214
Micropore surface area (m^2/g)	115	293
External surface area (m^2/g)	309	126
V_{micro} (cm^3/g)	0.151	0.145
V_{meso} (cm^3/g)	0.115	0.112

* The mesoporous aluminosilicate is synthesized under the conditions of Si:Al=5 and 2 °C/min heating rate.

Figure 47 shows the comparison of the nitrogen isotherms and adsorption curves of the selected mesoporous aluminosilicate and ZSM-5. Although the micropore and mesopore volumes of selected aluminosilicates and ZSM-5 are similar, the sizes of the pores in mesoporous aluminosilicate are mainly around 20 - 40 Å (Figure 47 (a)), overlapping with the range (17-30 Å) which has been proven to be crucial in the D4 adsorption process [75]. In the zoomed-in plot, the mesoporous aluminosilicate has more than twice the amount of pores with diameters of 17-30 Å than ZSM-5. In Figure 47 (b), ZSM-5 is saturated by D4 at around 160 min, 60 min faster than mesoporous aluminosilicate. The adsorption capacity of the aluminosilicate is 77.0 ± 3.70 mg/g, whereas the adsorption capacity of ZSM-5 is 40.9 ± 3.16 mg/g, is consistent with the one reported by Oshita et al. [86]. The better adsorption performance of the aluminosilicate is mainly attributed to its larger pore size. The majority of pores in the mesoporous aluminosilicate is in the range of 10-45 Å, much larger than the minimum projection diameter of D4 (9.8 Å, predicted by ChemAxon Marvin [161]). This can largely increase the possibility of adsorption of D4 inside the aluminosilicate during the adsorption process. Besides the larger pore size, the mesoporous

aluminosilicate has a larger external surface area than ZSM-5. The large external surface area of the mesoporous aluminosilicate is attributed to the fact that the UCT mesoporous materials are nanoparticle aggregates. The small particles of the mesoporous aluminosilicate can increase the adsorbent bed voidage and then increase the residence time of siloxanes. Overall, the good adsorption performance of mesoporous aluminosilicate is most likely due to the combined effects of large pore size and large external surface area.

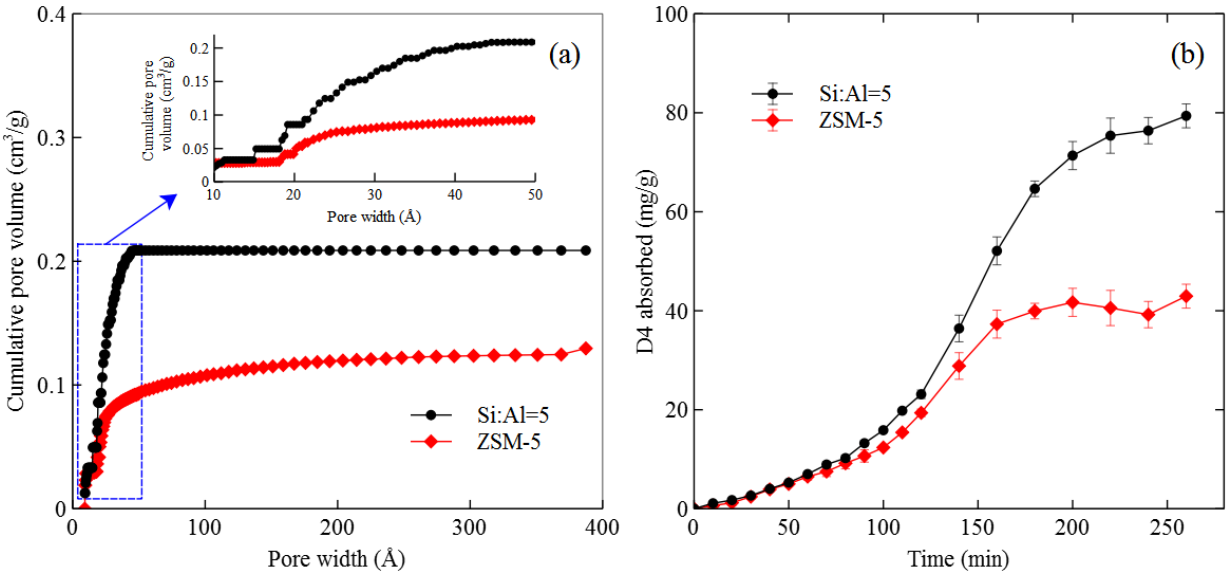

Figure 47: (a) Cumulative pore volume distributions (inserted is zoom-in area) and (b) adsorption curves of mesoporous aluminosilicate (Si:Al=5, 2 °C/min heating rate) and ZSM-5.

6.3 Influence of adsorbent textural parameters on D4 adsorption

Figure 48 shows the correlations between the D4 capacities and the textural parameters of mesoporous aluminosilicates. The data in Figure 48 have been fitted with both linear and parabolic equations. The fitted lines with highest R^2 values are shown. Generally speaking, there are good correlations between the D4 adsorption capacities and BET surface area, total pore volume, external surface area, and mesopore volume. Viewed by the different Si:Al ratios among the

synthesized materials and ZSM-5, the aluminum as acid sites might also contribute to D4 adsorption to some extent. However, in this study, the role of Al in siloxane adsorption was not clear, as the change of the Si:Al ratios was correlated with the change of the textual properties of the materials, such as BET surface area, external surface area, mesopore volume and total pore volume.

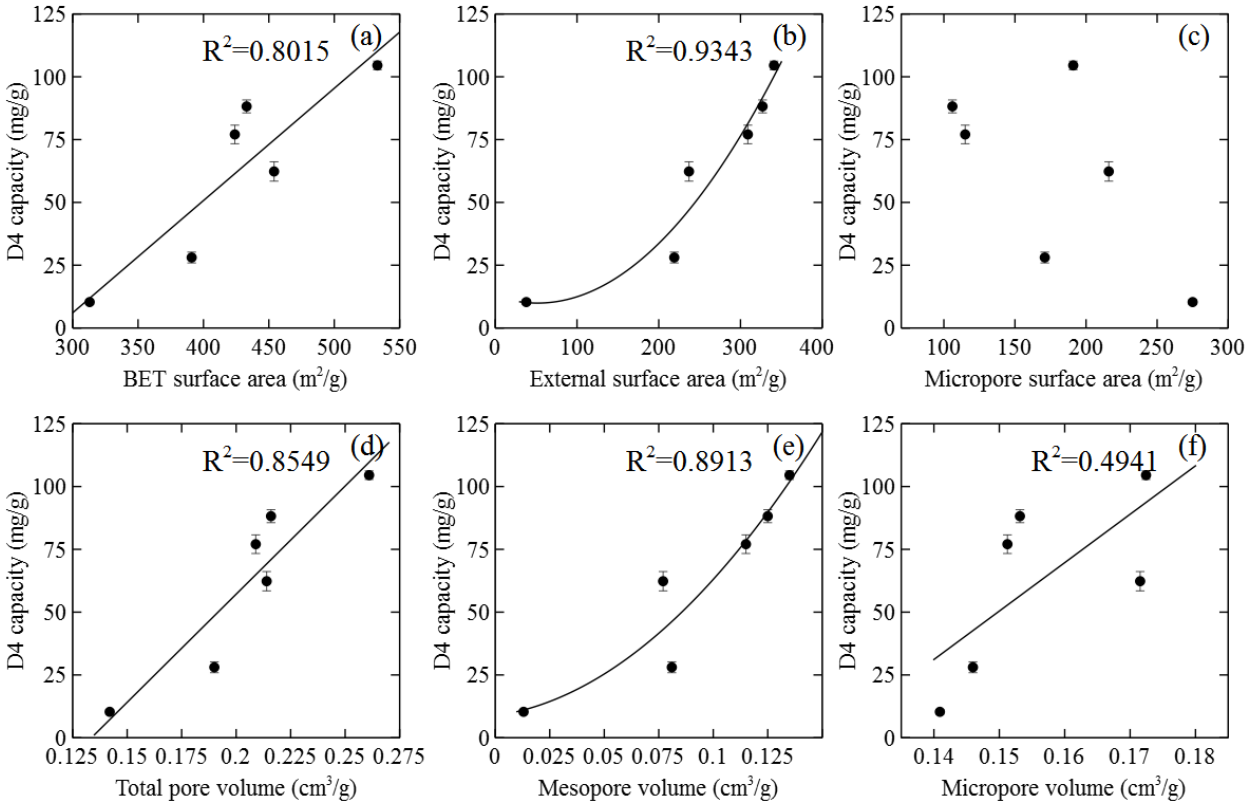

Figure 48: Correlation between D4 adsorption capacities and (a) BET surface area, (b) external surface area, (c) micropore surface area, (d) total pore volume, (e) mesopore volume (V_{meso}), and (f) micropore volume (V_{micro}) of mesoporous aluminosilicates.

To be specific, the BET surface area and the total pore volume of mesoporous aluminosilicates have a linear relation with the D4 adsorption capacities, whereas the external surface area and the mesopore volumes are related to the D4 adsorption capacities in a parabolic way. In contrast, the

micropore volume, micropore surface area, and averaged pore size (~20 Å for all the materials) of mesoporous aluminosilicates are not closely related to the D4 adsorption capacities. The parabolic relationship means some textual properties, such as mesopore volumes and external surface areas, have more impact on the adsorption capacity than other properties, such as micropore volume. The larger pore size of the adsorbents can provide larger possibility and wider pathways of adsorption (Figure 49), especially when the pore sizes of adsorbents (~20 Å) are close to the size of adsorbates (~10 Å). The larger mesopore volume will allow more D4 to remain in the adsorbents.

The correlations between the D4 adsorption capacities and BET surface area, total pore volume, and mesopore volume have been reported in the literature [75,76,86,162] and are in good agreement with this study. Moreover, this study further contributes to this research topic with the correlations between the D4 capacities and the external surface area and mesopore volume. The external surface area and mesopore volume have even better data regression than the BET surface area and the total pore volume. This means that the external surface area and mesopore volume of the mesoporous aluminosilicates have stronger impacts on the D4 adsorption than the other textual parameters. As has been mentioned before, the higher external surface area will promote the adsorption of D4 by increasing the residence time for the D4 bulk diffusion, while the larger pore size will affect the diffusion rate of D4.

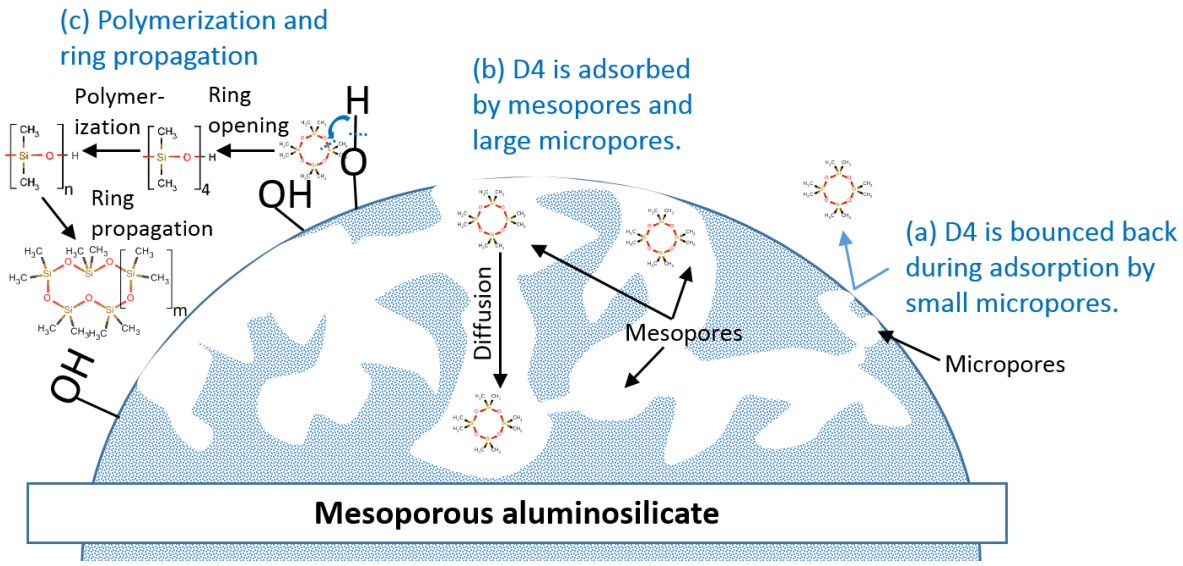

Figure 49: Fate of D4 during adsorption process: (a) D4 is repelled by small micropores; (b) D4 is adsorbed in mesopores and large micropores; (c) polymerization and ring propagation of D4 is catalyzed by hydroxyl groups.

6.4 Polymerization of D4 on mesoporous aluminosilicate adsorbents

Polymerization of adsorbed siloxane is considered to result in the ineffectiveness of the thermal regeneration of the adsorbents due to the formation of high-molecular-weight polymers [76,85,163]. Thus, the polymerization of D4 on the surface of the aluminosilicates was investigated in this study. We observed the D4 polymerization by dissolving the adsorbed species in hexane and analyzing the extracted solution by GC-MS. A typical GC-MS spectrum of extracted solution is shown in Figure 52 (a), where the signals from D5, D6, and D7, products of D4 polymerization, are all observed. Another typical GC-MS spectrum of pure D4 in solution is shown in

Figure **50**. The structure of regenerated adsorbent doesn't change too much after regenerated by dissolving the adsorbed species in hexane (Figure 51).

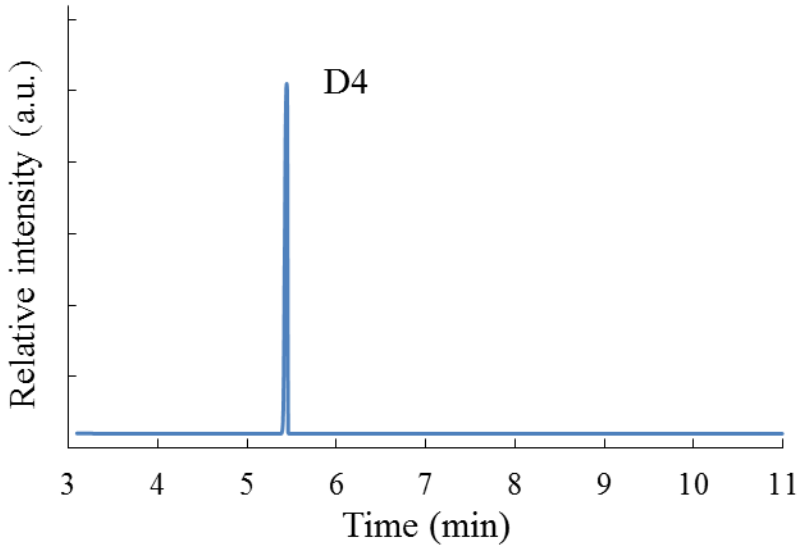

Figure 50: A GC spectrum of pure D4 in hexane. (No D5, D6, or D7 were shown in this spectrum.)

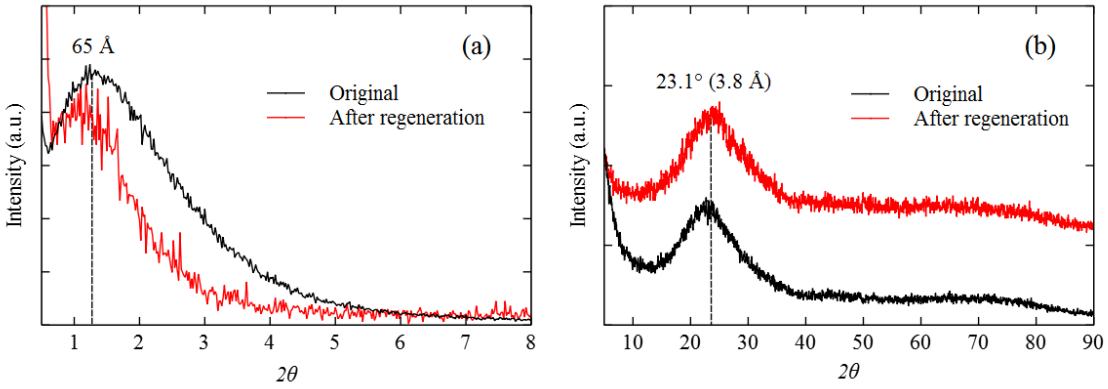

Figure 51: (a) Low-angle and (b) high-angle XRD patterns of original and after-regeneration mesoporous aluminosilicate (Si:Al=5, 10 °C/min calcination heating rate).

D4 polymerization has been attributed to the hydroxyl groups on the adsorbents (Figure 49). Soreanu et al. [79] and Sigot et al. [163] pointed out that siloxane molecules (D4) could interact with hydroxyl groups on the adsorbent surface by H bridges (hydrogen bonds). More specifically, Cabrera-Codony [76] claimed that the surface hydroxyl groups could work as catalytic active centers for cyclosiloxane ring-opening polymerization [76,163]. In this study, we performed the

TG-MS analyses on all of the synthesized mesoporous aluminosilicates to verify the existence of the hydroxyl groups on the adsorbents. As shown in Figure 52 (b), the dehydroxylation of mesoporous aluminosilicate takes place at around 200 °C. Since hydroxyl (water) species is the only species detected by MS, the amount of hydroxyl groups can be quantified based on the weight loss determined by thermogravimetric analysis. The quantity of the hydroxyl group on the mesoporous aluminosilicates increases with the amount of aluminum dopant, whereas the 1 °C/min and 5 °C/min heating rates during calcination produce the highest and lowest amount of hydroxyl groups on the mesoporous aluminosilicates, respectively. The reason for this phenomenon was not clear. One possible explanation is given here. The formation of hydroxyl groups is mainly affected by calcination and rehydroxylation steps. In the calcination step, the as-synthesized mesoporous aluminosilicates undergo dehydration (the removal of physically adsorbed water) and dehydroxylation (the removal of silanol groups from the silica surface) [164,165]. In the rehydroxylation step, the hydroxyl groups are restored on the silica surface under ambient conditions. As mentioned before, different calcination heating rates can change the atomic ordering of the SiO_2 structure. This implies that the surface area of a specific oriented face of the SiO_2 nanoparticles may also be changed during synthesis [166]. This results in the increase of the surface area of some relatively hydrophobic faces in the material [167]. The mesoporous aluminosilicate synthesized under medium calcination heating rate (5 °C/min) is suspected to possess higher surface area of the hydrophobic faces than those under slower and faster calcination heating rates (1 °C/min and 10 °C/min). This makes it difficult to restore the hydroxyl groups in the subsequent rehydroxylation step, leading to the lowest amount of hydroxyl groups on the material.

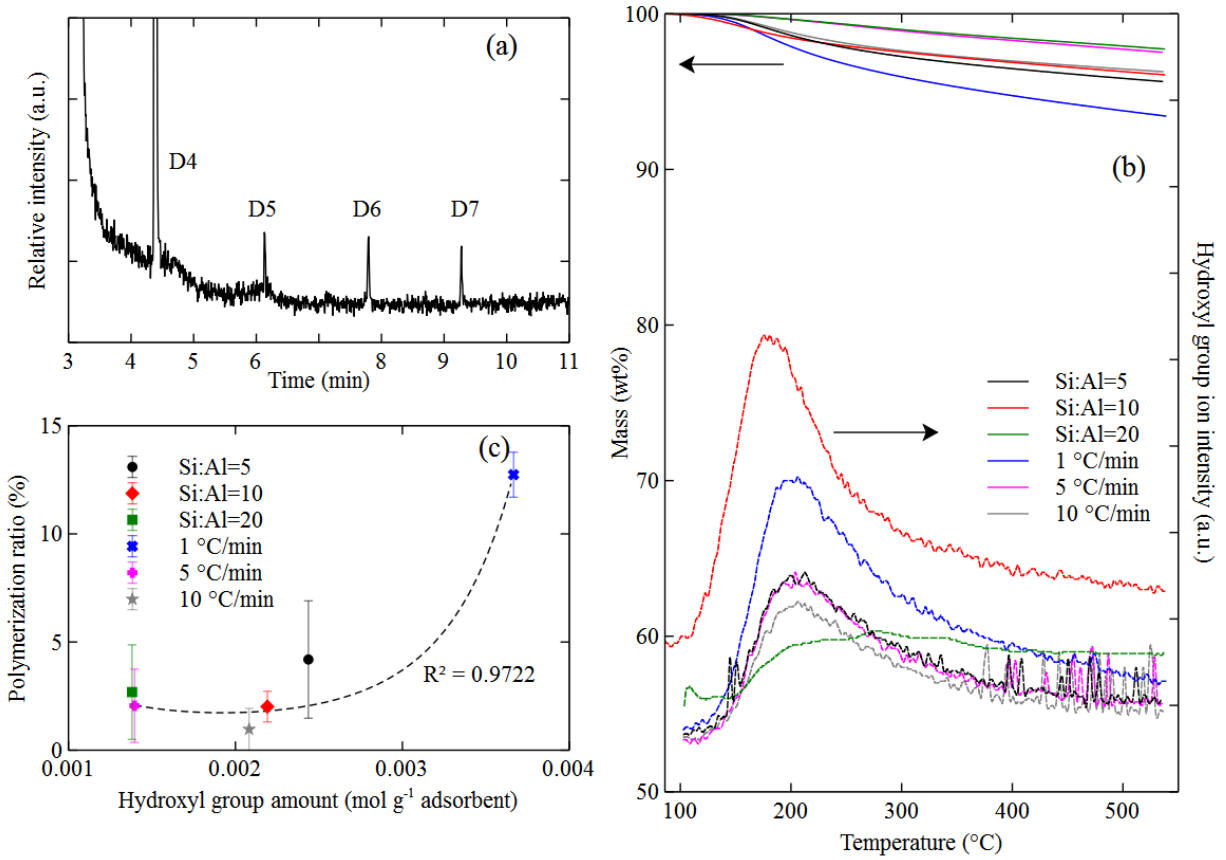

Figure 52: (a) A typical GC spectrum from the washed-out solution of adsorbent, (b) TG-MS profiles of mesoporous aluminosilicates, and (c) correlation between polymerization ratio and hydroxyl group amount. The polymerization ratio was calculated as the total amount of extracted D5, D6, and D7 over the amount of extracted D4.

A correlation between polymerization ratio and the hydroxyl group amount is shown in Figure 52 (c). Generally, polymerization of the siloxane D4 is enhanced by the hydroxyl groups on the surface of the mesoporous aluminosilicate. This observation agrees well with the observation made by Cabrera-Codony et al., [76] who used active carbons as siloxane adsorbents and found that the polymerization ratios were higher for the active carbons with relatively high surface oxygen concentrations. In order to promote the recyclability of the adsorbent, future work about the

development of the adsorbent with a neutral surface (minimal amount of hydroxyl group) to prevent undesired polymerization reaction will be of interest. Based on the findings in this study, balancing the D4 adsorption capacity and polymerization of the adsorbed D4, it is suggested that relatively low aluminum dopant amount and a fast heating rate should be implemented for the synthesis of mesoporous aluminosilicate as excellent D4 adsorbents.

7. CONCLUSIONS

7.1 Dye degradation

Mesoporous γ-Fe_2O_3 and Fe_3O_4 have been successfully synthesized by changing the reaction temperature of a sol-gel based on the inverse micelle method to a higher temperature (100 °C) and heating at 150 °C for 12 hours and 250 °C for 4 hours under an air atmosphere and nitrogen atmosphere respectively. The mesoporous structures of mesoporous iron oxides are confirmed by low-angle XRD, BET, and TEM. Phases of mesoporous iron oxides are confirmed by high-angle XRD, Raman spectroscopy, and XANES. All the synthesized materials show vacancies in their own structure. The higher reaction temperature (100 °C) forms Fe(II) species. If as-made samples are heated under a nitrogen atmosphere, Fe(II) species can be preserved to form the Fe_3O_4 phase. If as-made samples are heated under air atmosphere, Fe(II) species will be oxidized to form the γ-Fe_2O_3 phase. Mesoporous γ-Fe_2O_3 and Fe_3O_4 have larger pore sizes and smaller surface areas, compared with mesoporous 2-line ferrihydrite and α-Fe_2O_3. The sintering of nanoparticles will cause the expansion in pore size and decrease the surface area. The greatest adsorption capability of orange II is found in 2-line ferrihydrite (49.3 mg orange II/g cat.) which is two times larger than that of commercial Fe_2O_3. The trend of adsorption capacities of orange II on mesoporous iron oxides roughly follows the trend of surface area. The photocatalytic performances of mesoporous iron oxides are all better than that of commercial Fe_2O_3. The apparent rate constants clearly show that the best catalyst 2-line ferrihydrite has 6 times better activity than that of commercial Fe_2O_3. All the reaction solutions catalyzed by mesoporous iron oxides have pH drops during the reactions. In particular, the pH of the solutions catalyzed by 2-line ferrihydrite drops to 4.4, the largest drop among mesoporous iron oxides. The stability test shows the mesoporous iron oxides can maintain the performance until the 4^{th} cycle. The meso-structure of the catalyst is reserved after the 4^{th} run

of reaction. According to reaction intermediates monitored by ESI/MS, 2-line ferrihydrite catalyst can start degrading aromatic rings to smaller species at the beginning of the reaction whereas in the solution catalyzed by commercial Fe_2O_3 a large amount of aromatic species remain until the end of reaction.

7.2 Nitrobenzene hydrogenation

Magnetically recyclable Pd/meso-γ-Fe_2O_3 catalysts have been successfully synthesized by impregnation and one-step sol-gel methods. The catalysts are designed to have large surface areas, pore sizes, and pore volumes, which promote the dispersion of Pd nanoparticles. All of the synthesized catalysts have very high selectivity for the aniline product in the nitrobenzene hydrogenation reaction. Higher Pd loading accelerates the reaction catalyzed by Pd/meso-γ-Fe_2O_3 catalysts using the impregnation and one-step sol-gel methods. Among all the synthesized catalysts using the impregnation method, the 1% Pd/meso-γ-Fe_2O_3-im catalyst has the highest activity and highest TOF number due to its large surface area, pore size, pore volume, and interconnected network of the iron oxide support. The 2% Pd/meso-γ-Fe_2O_3-im catalyst has similar reaction rate with the 1% Pd/meso-γ-Fe_2O_3-im catalyst due to Pd nanoparticle aggregation. The 1% Pd/meso-γ-Fe_2O_3-im catalyst has a higher activity than 1% Pd/meso-γ-Fe_2O_3-os catalyst because of more accessible Pd nanoparticles on the surface of the mesoporous Fe_2O_3 support in the Pd/meso-γ-Fe_2O_3-im catalyst. The one-step sol-gel synthesis method can help improve the recyclability of the Pd/meso-γ-Fe_2O_3 catalysts by preventing leaching, compared to the impregnation method.

7.3 Siloxane adsorption

Aluminum dopant amount and calcination heating rate can be varied to tune the textural properties of mesoporous aluminosilicates. Higher aluminum dopant increases the external surface area and

mesopore volume of the mesoporous aluminosilicates, whereas higher calcination heating rate increases the BET specific surface area, external surface area, total pore volume, micropore volume, and mesopore volume of the mesoporous aluminosilicates. The mesoporous aluminosilicates synthesized with a larger amount of aluminum dopant and under a faster calcination heating rate has a better adsorption performance. The best adsorbent for D4 adsorption is found to be mesoporous aluminosilicate synthesized with Si:Al=5 and under a 10 °C/min calcination heating rate. The mesoporous aluminosilicate adsorbent with similar BET surface area and total pore volume for ZSM-5 works more than twice as well as a commercial ZSM-5, mainly because of the larger pore size and external surface area of the aluminosilicate. The adsorption capacities of mesoporous aluminosilicates are linearly related to the BET specific surface area and total pore volume and related to the external surface area and mesopore volume in a parabolic way. The polymerization of D4 is found to increase with the amount of hydroxyl groups on the surface of the aluminosilicates.

8. OUTLOOK

8.1 Introduction

Photocatalytic water splitting has become an active research area and a promising way to capture and store energy [168], since a TiO_2 and Pt based catalytic system was discovered in 1972 by Fujishima and Honda [169,170]:

$$H_2O(l) \rightarrow \frac{1}{2}O_2(g) + H_2(g); \Delta G = +237kJ/mol\ (1.3eV/e)$$

The catalyst efficiency in photocatalytic water splitting reaction can be evaluated by the quantum yield (QY), which is defined as

$$QY = \frac{number\ of\ reacted\ electrons}{number\ of\ incident\ photons} \times 100\%$$

The quantum yield of photocatalytic water splitting reaction can be affected by several factors. The good light adsorption, long hole diffusion distance (hence long recombination distance), low charge recombination in the bulk, fast charge transfer across the surface, and high density of active sites contribute to higher quantum yield.

Over the past three decades, over 130 inorganic materials have been found able to either catalyze the overall splitting of water, or induce water oxidation/reduction in the presence of external redox agents [171]. Under 270 nm UV light irradiation, the NiO-modified $La/KTaO_3$ photocatalyst reported by Kato et al. [172] has 56% apparent quantum yield in water splitting, producing H_2 and O_2 in a stoichiometric amount. However, under simulated sunlight irradiation, the nanocrystalline CoO catalyst reported by Liao et al. [173] has only 5% quantum yield in water splitting, producing H_2 and O_2 stoichiometrically. Under 420 nm to 440 nm visible light irradiation, the $(Ga_{1-x}Zn_x)(N_{1-}$

$_xO_x$) photocatalyst modified with Rh-Cr mixed oxide nanoparticle has 2.5% quantum yield for overall water splitting [174,175]. So far, the limited quantum efficiency (<10%) in water splitting reaction with solar light or simulated sunlight has not satisfied the requirement of the process commercialization. No material is capable of catalyzing overall water splitting reaction with solar light or simulated sunlight with >10% quantum yield and long term stability [176]. Therefore, researches on catalysis, especially design of photocatalysts, are of great interest. This proposed research aims to develop new materials that can promote the water splitting efficiency.

8.2 Main process of water splitting

Figure 53 shows the main process of photocatalytic water splitting [177]. The first step is the adsorption of photons to form electron-hole pairs. If the energy of incident light is larger than that of a band gap of the catalyst, the electrons on the valence band will be excited to the conduction band and holes will be generated on the valence band. The photogenerated electrons and holes cause redox reactions, similar to electrolysis. The width of band gaps and energy levels of conduction and valence bands are important for this step. The second step includes charge separation and migration of photogenerated carriers to surface reaction sites. Catalysts with a small amount of defects and large particle sizes are preferred in this step since these characters will slow down the recombination rate of electrons and holes. The third step involves the surface chemical reaction for H_2 and O_2 evolution. The number of surface active sites, i.e., surface area of the catalyst, is crucial for this step.

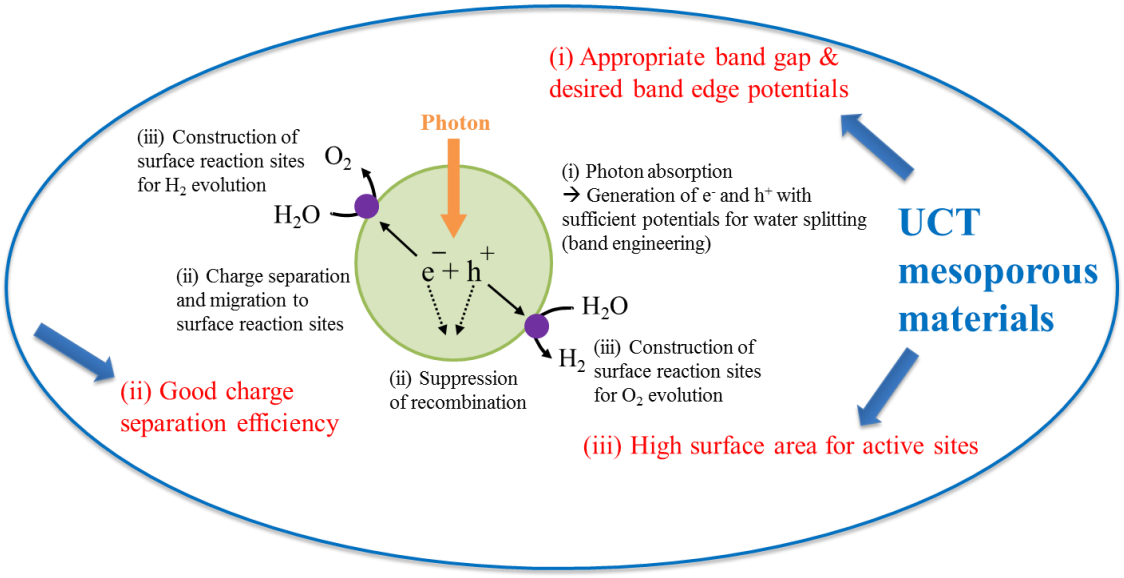

Figure 53: Main process of photocatalytic water splitting. (Reproduced from ref [177] with permission of The Royal Society of Chemistry).

8.3 Potentials of mesoporous materials in water splitting

UCT mesoporous materials have a lot of advantages which make them promising for photocatalytic water splitting. These advantages are illustrated in Figure 53 and described as follows.

i. Appropriate band gap (good light adsorption)

The band gap of photocatalysts can be modified by adding dopant into the intrinsic materials. The semiconductor materials have a wide range of band gap energies.

ii. Desired band edge potential

The desired band edges of catalysts are as follows: (a) the potential of the conduction band is higher than the potential of proton reduction and (b) the potential of the valence band is lower than the potential of water oxidation.

iii. Good charge separation efficiency

The charge separation efficiency depends on intrinsic electronic and structural properties of the catalyst. To improve this efficiency, on one hand, we need to suppress the electron-hole recombination rate (long diffusion distance); on the other hand, we need to increase the surface charge carrier transfer rate.

iv. High surface area for active sites

The high surface area of the catalysts offers enough active sites for generating electrons and holes to produce H_2 and O_2.

v. Chemical stability

Mesoporous materials are chemically stable, which makes the catalysts robust under both reducing and oxidizing environments.

8.4 Catalyst design strategy

The proposed catalyst design strategy include three steps for photocatalyst design. The first step is to screen catalysts by band gaps and energy levels of valence band and conduction band in order to find suitable materials with good light adsorption property and suitable thermodynamic potential. The second step is to optimize the properties of the suitable materials, such as surface area and charge transfer efficiency. The third step is to synthesize composite catalyst which includes the most suitable material with each function in the reaction, such as light harvest and oxygen evolution sites, in order to improve overall quantum yield of photocatalytic water splitting reaction.

8.4.1 *Screening the catalysts by band gaps and energy levels of the semiconductors*

The photocatalytic properties of semiconductor catalysts strongly depend on the electronic band structure, i.e, band gaps and energy levels of valence and conduction bands. For occurrence of water reduction, the potential of conduction band edge must exceed the proton reduction potential of 0.0 V vs NHE at pH=0 (-0.41 V at pH=7). To facilitate water oxidation, the potential of the valence band edge must exceed the oxidation potential of water of +1.23 V vs NHE at pH=0 (+0.82 V at pH=7). A diagram about potential energy for water splitting [171] is shown in Figure 54. In Figure 54, type I catalyst has the suitable thermodynamic potentials for both water reduction and water oxidation reaction. Type II and type III catalysts can only work for half of the water splitting reaction. Type IV catalyst is the combination of type II and type III catalysts and the electron acceptor and donor couples work at the interface of type II and type III catalysts in order to transfer the electrons. The band gaps and energy levels of valence and conduction bands of some common semiconductors [177] are shown in Figure 55. Table 10 summarizes some reported catalysts in photocatalysis for water splitting reaction.

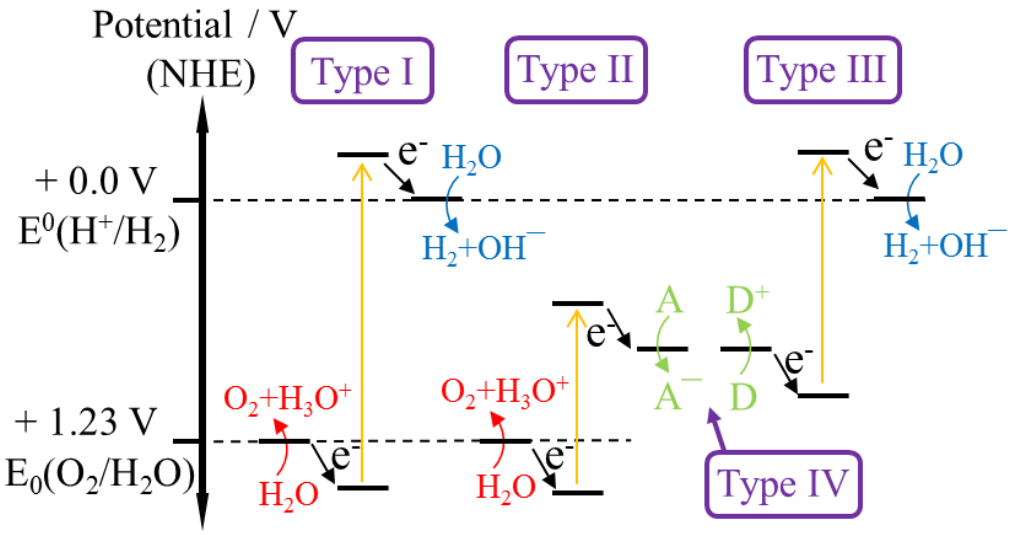

Figure 54: Potential Energy diagrams for water splitting at pH=0: (a) single semiconductor (Type I); (b) O_2 evolution (water oxidation) (Type II); (c) H_2 evolution (water reduction) (Type III); (d) dual semiconductor system (Type IV, A represents the electron acceptor and D represents the electron donor). (Reprinted with permission from ref [171], copyright (2008) American Chemical Society.)

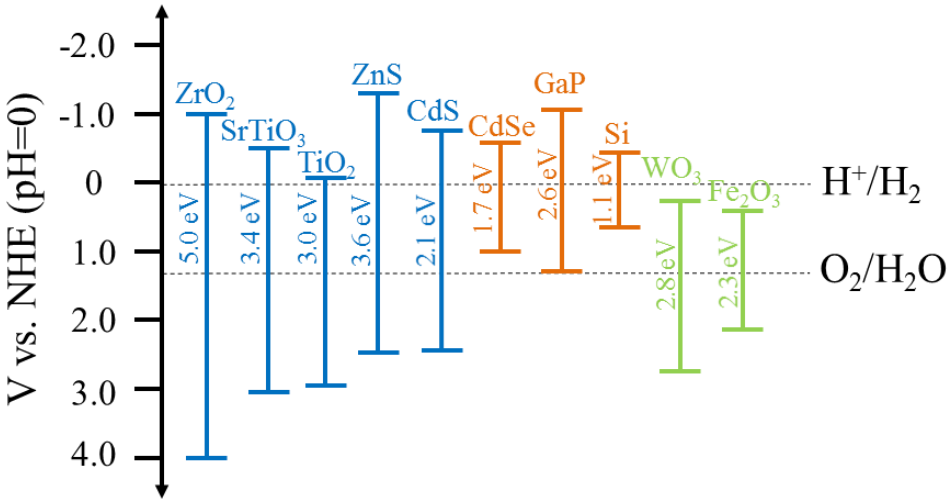

Figure 55: Band gaps and energy levels of valence and conduction bands of semiconductors for water splitting. (Reproduced from ref [177] with permission of The Royal Society of Chemistry).

Table 10: Selected oxide photocatalysts for water splitting from the literature.

Catalyst type	Photocatalyst	Band gap / eV	Co-catalyst	Light source	Reaction solution	H_2 production (μmol/h)	O_2 production (μmol/h)
I	TiO_2	3.2	Pt	UV	pure water	106	53
II	Fe_2O_3	2.1	none	sunlight	oxidizing reagent	-	15
III	Co_3O_4	2.1	none	UV	pure water	6	-
I	CoO	2.6	none	sunlight	pure water	11	5.5
I, III	Ta_2O_5	4.0	NiO_x	UV	pure water	1154	529
I, III	Ga_2O_3	4.6	NiO	UV	pure water	46	23
III	$SrTiO_3$:Cr/Ta	2.3	Pt	visible	reducing reagent	70	-

II	$PbMoO_4$:Cr	2.3	none	visible	oxidizing reagent	-	71.5
IV	Cr/Ta:$SrTiO_3$-Pt & Pt-WO_3	2.7	Pt	visible	$NaI/NaIO_3$ redox couple	0.8	84.0

- Reducing reagent is CH_3OH aq; Oxidizing reagent is $AgNO_3$. -not available
(reproduced from ref [177] with permission of The Royal Society of Chemistry).

8.4.2 *Optimization of the properties of the suitable materials*

UCT mesoporous materials can provide large surface area, controllable pore size, and controllable morphology and crystallinity by changing the synthesis conditions [177]. From the dye degradation application of mesoporous iron oxide, it proved that phases, surface area, crystallinity, and pore size of mesoporous iron oxide can be tuned by the reaction temperature and calcination atmosphere. Usually when the calcination temperature increases, the crystallinity of mesoporous metal oxides increases and surface areas of mesoporous metal oxides decrease. For photocatalytic water splitting reaction, catalysts with high degree of crystallinity is often preferred. Because the high crystallinity will reduce the number of boundaries and defects, which work as recombination centers between photogenerated electrons and holes [177]. Then the electrons and holes with prolonged life time caused by slow recombination rate can improve the photocatalytic activity of catalysts. However, increase of crystallinity of catalysts will make a compromise with high surface area, which is directly related to the amount of active sites for the surface hydrogen and oxygen evolution reactions. Figure 56 shows the how the synthesis conditions can affect the crystallinity and surface area of photocatalysts in the case of TiO_2. There is an optimum point to balance these two structural parameters for photocatalysts. The tunable structural properties of UCT mesoporous materials provide the opportunity to find the optimum synthesis conditions for the best photocatalysts.

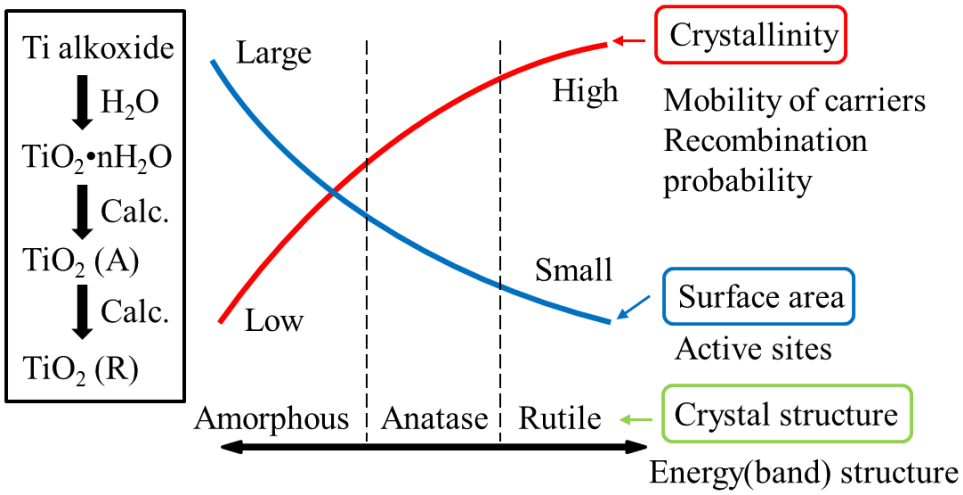

Figure 56: Synthesis conditions affecting photocatalytic activity of TiO_2. (Reproduced from ref [177] with permission of The Royal Society of Chemistry).

Furthermore, the interconnected mesoporous network of UCT mesoporous materials can help with the dispersion of nanoparticle active sites. From the application of nitrobenzene hydrogenation, it has been proved that the Pd nanoparticles in mesoporous iron oxide catalyst can be dispersed very well by the interconnected mesoporous network. Another results reported by Jiao et al. [178] also proved the importance of dispersion of active sites of the catalysts. The mesoporous silica was used to stabilize MnO_x nanoclusters and the oxygen evolution activity of manganese oxide catalysts could be improved. Since the active centers of the water oxidation reaction on manganese oxide is Mn^{3+}, the controllable synthesis of MnO_x with enriched Mn^{3+} species is therefore highly desired. Stabilization of Mn^{3+} active centers by mesoporous materials can prevent the aggregation of nanoparticles, improving the catalyst activity.

In addition, the large pore size (up to 24.5 nm) and the interconnected mesoporous network of the UCT mesoporous materials provide the opportunity for further modification of the catalysts in various ways. For example, the fast recombination rate is a common problem of semiconductors

in water splitting application. Improving the conductivity of the catalysts is an efficient way to separate electrons and holes, and thus suppress the recombination in the first step of water splitting. The electronic communication between the active center and redox species can be improved by adding conductive materials, such as Au nanoparticles [179] or conductive polymers. The big pore size and mesoporous network of mesoporous materials provide enough space to accommodate these conductive materials in the pore structure. Furthermore, since the mesopores of UCT mesoporous materials are interconnected, a connected chain-shape or tree-shape conductor can be formed inside the mesoporous metal oxides, which will possibly increase the photocatalytic activity of the catalysts.

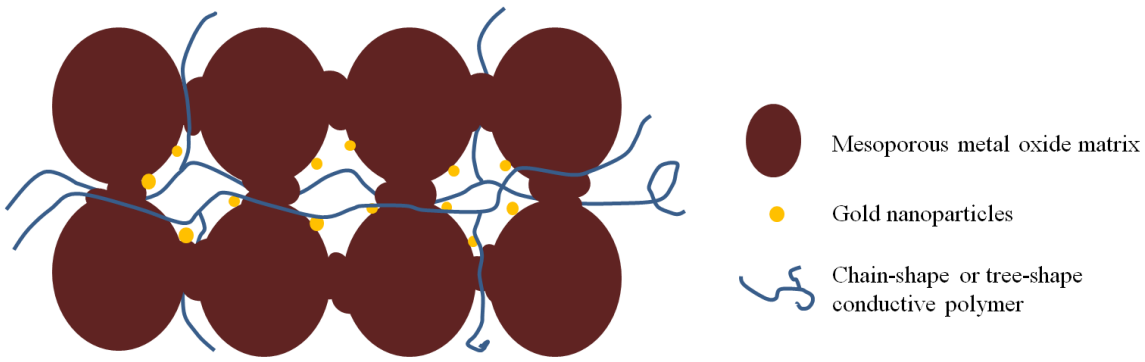

Figure 57: Schematic diagram of improving UCT mesoporous materials by adding gold nanoparticles and/or chain-shape or tree-shape conductive polymer.

8.4.3 *Composite catalyst with separate functions in each part*

The high quantum yield catalysts which can decompose pure water under sunlight irradiation without any sacrificial reagents are desirable for the photocatalytic water splitting reaction. As discussed before, the challenges for efficient photocatalysts of the water splitting reaction with high quantum yield are to develop a catalyst which has small band gap, suitable band edges, good charge transfer efficiency, and a large surface area at the same time. It is difficult to find a single

semiconductor which has so many merits. Therefore, one of the strategy to make efficient catalysts is to separate the desired functions of the catalyst by synthesize composite catalysts which can take the advantages of several different materials. A typical example is the catalyst synthesized by Maeda et al [180]. Figure 58 shows the schematic diagram of Rh-Cr mixed oxide nanoparticle promoted $(Ga_{1-x}Zn_x)(N_{1-x}O_x)$ photocatalyst. In their catalyst system, a solid solution of GaN and ZnO was used as the materials to harvest visible photons and Rh/Cr_2O_3 and Mn_3O_4 nanoparticles were used as a H_2 evolution catalyst and an O_2 evolution catalyst, respectively. Comparing with the catalysts without an efficient water oxidation center (Mn_3O_4), combination of the Rh/Cr_2O_3 and Mn_3O_4 will largely increase the overall performance of the catalyst.

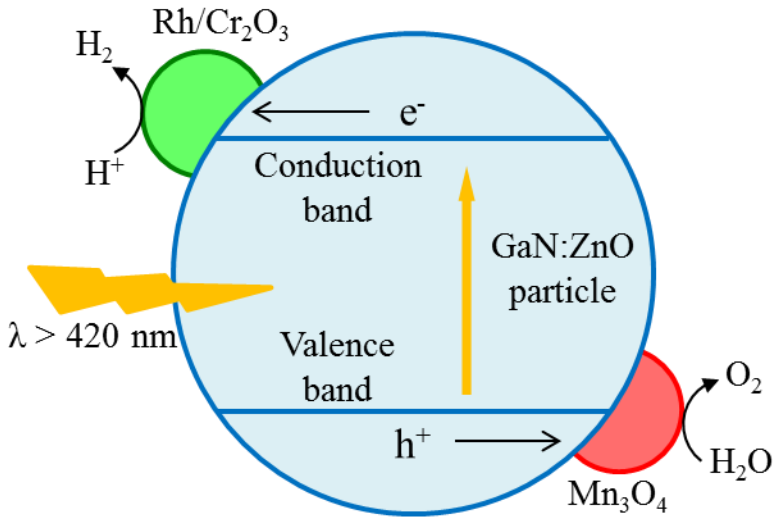

Figure 58: Schematic diagram of the Rh-Cr mixed oxide nanoparticle promoted $(Ga_{1-x}Zn_x)(N_{1-x}O_x)$ photocatalyst. (Reproduced from reference [180] with permission of Wiley)

8.5 Proposed catalysts for water splitting

8.5.1 *Mesoporous iron oxide based catalysts for O_2 evolution*

Iron oxide (α-Fe_2O_3) with low a band gap (~2.1eV, which absorbs light up to 600 nm wavelength), low cost, and high chemical stability is very promising for a water splitting catalyst. Due to the energy levels of conduction and valence band and the energy levels of water reduction and oxidation, iron oxide can be used as a water oxidation catalyst. However, its poor conductivity and high electron-hole combination rate are major challenges to be overcome [181]. The approaches to improve iron oxide are to introduce heteroatom as the dopant [182–184], to control morphology and crystallinity of iron oxide. Because introducing impurities can increase the carrier density and improve the conductivity of hematite. The morphology and crystallinity of iron oxide synthesized by the sol-gel method can be controlled by synthesis conditions, such as surfactant type and amount and calcination process. Nanorod or nanoarray morphology is preferred because light can be absorbed along the longitudinal direction and electrons and holes can be separated along the transverse direction.

8.5.2 *Catalysts for overall water splitting*

A multi-component composite catalyst (quantum dots promoted NiO_x-Fe_2O_3/Co_3O_4/graphene) is promising for overall water splitting under sunlight irradiation. Mesoporous cobalt oxide is chosen as the matrix of the catalyst since cobalt oxide has been widely reported to be an efficient catalyst for water oxidation and water reduction reactions. The high surface area of UCT mesoporous cobalt oxide will further help increase the performance of the catalyst. Graphene is used as the conductive materials to charge transfer between different components of the catalyst. Because graphene which has two-dimension sp^2 hybridized carbon atoms has extraordinary electrical

properties and an ultra large surface area. NiO is chosen as a water reduction catalyst. Because the NiO and NiO_x are not noble-metal oxides and have been used as co-catalysts by many researchers [177]. Since Fe_2O_3 has a small band gap (~2.1 eV), good light absorbability, and low-cost, Fe_2O_3 is used as a water oxidation catalyst. The light adsorption property of the proposed catalyst can be also improved by CdSe/CdS core-shell quantum dots which can absorb the lights below 500-600 nm wavelength. During the catalyst synthesis, fabrication of interfaces of semiconductors will be essential for the overall performance of the catalyst.

8.6 Proposed experimental strategy

8.6.1 *Experimental setup*

A schematic diagram of experimental setup for the photocatalytic water splitting is shown in Figure 59. Light irradiation is introduced from the top of the reactor. The opening of the quartz window can be used to control the area of light irradiation, and filters can be added on the top of the quartz window to examine the effect of wavelength of the light. Cooling system can be added outside the reactor which will help maintain the temperature of the reactor. The photoreactor should be a gastight system, having openings for gas inlet, gas outlet, and the sensor. The data from the sensor can be recorded by the computer.

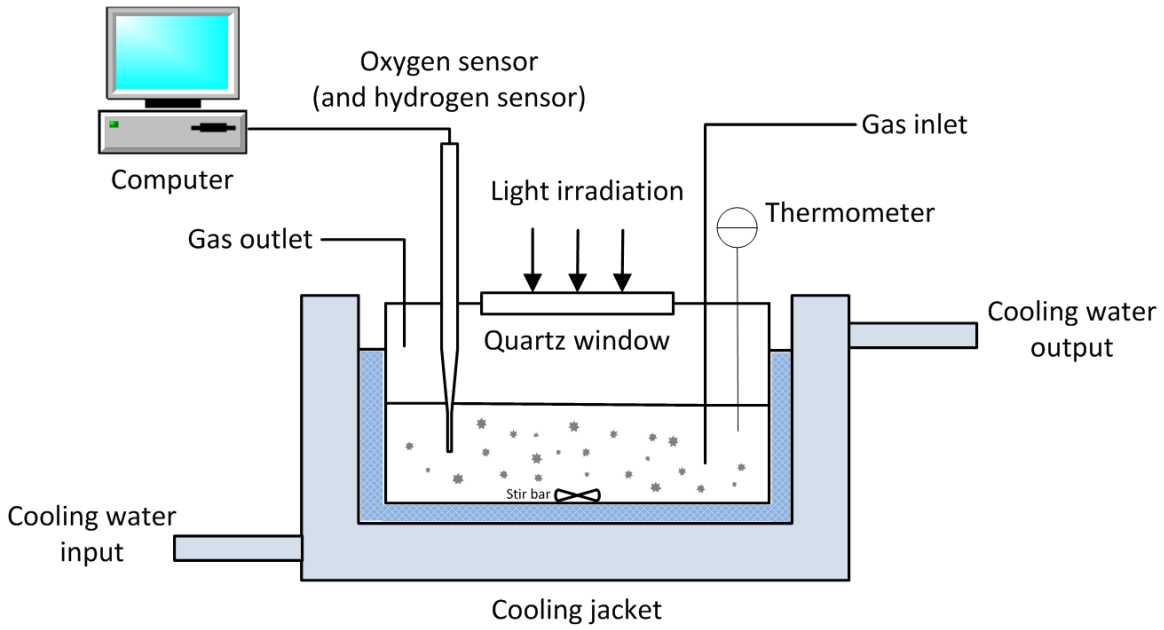

Figure 59: Experimental setup for the water oxidation reaction and overall water splitting.

8.6.2 *Experimental conditions*

Water oxidation reaction conditions

$Ru(bpy)_3^{2+}$ can be used as photon collector. $Na_2S_2O_8$ and Na_2SO_4 will be used as sacrificial agents. Simulated sunlight will be used as a light source. Dissolved oxygen sensor can be used as the oxygen meter. Na_2SiF_6–$NaHCO_3$ can be used as buffer solution.

Overall water splitting conditions

Visible light or simulated sunlight (Xenon lamp) will be used as the light source. No additional oxidizing agent of reducing agent will be used. It is also possible to use D_2O and H_2O^{18} isotopes to reveal the rate determining step of the reaction on the newly developed catalyst. Because the reaction rate of the reaction can be affected by the isotopes.

APPENDIX I LIST OF PUBLICATIONS AND CONFERENCE PRESENTATIONS

Publications

- Ting Jiang, Wei Zhong, Tahereh Jafari, Shoucheng Du, Junkai He, You-Jun Fu, Steven L. Suib. Adsorption of siloxane by mesoporous aluminosilicates (UCT-15) for biogas cleanup. *Chemical Engineering Journal*, **2016**, 289, 356–364.
- Ting Jiang, Shoucheng Du, Tahereh Jafari, Wei Zhong, Yu Sun, Wenqiao Song, Zhu Luo, William A. Hines, Steven L. Suib. Synthesis of mesoporous γ-Fe_2O_3 supported palladium nanoparticles and investigation of their roles as magnetically recyclable catalysts for nitrobenzene hydrogenation. *Applied Catalysis A: General*, **2015**, 502, 105–113.
- Ting Jiang, Altug S. Poyraz, Aparna Iyer, Yashan Zhang, and Steven L. Suib. Synthesis of mesoporous iron oxides by an inverse micelle method and their application in the degradation of orange II under visible light at neutral pH. *J. Phys. Chem. C*, **2015**, 119, 10454−10468.
- Tahereh Jafari, Ting Jiang, Wei Zhong, Nasser Khakpash, Bahareh Deljoo, Mark Aindow, Prabhakar Singh, Steven L. Suib. Modified mesoporous silica for efficient siloxane capture. *Langmuir*, **2016**, 32, 2369−2377
- Zhu Luo, Shaylin A. Cetegen, Ran Miao, Ting Jiang, Sheng-Yu Chen, Tahereh Jafari, Yashan Zhang, Steven L. Suib. Structure-property relationships of copper modified mesoporous TiO_2 materials on alkyne homocoupling reactions. *Journal of Catalysis*, **2016**, 338, 94–103

- Stephen O. Hay, Timothy Obee, Zhu Luo, Ting Jiang, Yongtao Meng, Junkai He, Steven C. Murphy, Steven Suib. The viability of photocatalysis for air purification. *Molecules*, **2015**, 20, 1319-1356.
- Ran Miao, Zhu Luo, Wei Zhong, Sheng-Yu Chen, Ting Jiang, Biswanath Dutta, Youmna Nasr, Yashan Zhang, Steven Suib. Mesoporous TiO_2 modified with carbon quantum dots as a high-performance visible light photocatalyst. *Applied catalysis B: environmental*, **2016**, 189, 26–38.
- Yashan Zhang, Lei Jin, Kevin Sterling, Zhu Luo, Ting Jiang, Ran Miao, Curtis Guild, Steven L. Suib. Potassium modified layered $Ln_2O_2CO_3$ (Ln: La, Nd, Sm, Eu) materials: Efficient and stable heterogeneous catalysts for biofuel production. *Green Chemistry*, **2015**, 17, 3600–3608.
- Zhu Luo, Altug S. Poyraz, Chung-Hao Kuo, Ran Miao, Yongtao Meng, Sheng-Yu Chen, Ting Jiang, Chelsea Wenos, Steven L. Suib. Crystalline mixed phase (anatase/rutile) mesoporous titanium dioxides for visible light photocatalytic activity. *Chemistry of Materials*, **2015**, 27, 6−17.
- Ben Liu, Ting Jiang, Wenqiao Song, Haoquan Zheng, Jie He, Steven L. Suib. Nanoengineering of Aggregation-Free and Thermally-Stable Gold Nanoparticles in Mesoporous Oxide Frameworks. *Science Advance*, **2016**. Submitted.
- Wei Zhong, Ting Jiang, Tahereh Jafari, Altug Poyraz, Wei Wu, David Kriz, Sourav Biswas, Michael Pettes, Steven L. Suib, Facile inverse micelle synthesis for mesoporous alumina with adjustable pore sizes and an excellent D4 siloxane adsorption performance. *Microporous and mesoporous materials*, **2016**. Submitted.

- Wei Zhong, Chung-Hao Kuo, Ting Jiang, Sheng-Yu Chen, You-Jun Fu, Raymond Joesten, Yongtao Meng, David Kriz, Andrew Meguerdichian, Junkai He, Steven L. Suib. Efficient non-photocatalytic dye degradation by perovskite type $LaNiO_{3-\delta}$ material. *Applied catalysis B: Environmental*. **2015**. Submitted.
- Iman Noshadi, Baishali Kanjilal, Tahereh Jafari, Ehsan Moharreri, Nasser Khakpash, Ting Jiang, Steven L. Suib. Hydrophobic mesoporous adsorbent based on cyclic amine - divinylbenzene copolymer for highly efficient siloxane removal. *RSC Advances*. **2016**. Submitted.

Patents & disclosures

- Ting Jiang, Tahereh Jafari, Wei Zhong, Steven L. Suib. Advanced mesoporous aluminosilicate adsorbents for siloxane adsorption. Fraunhofer USA, Patent F0739.70004US01, application filed, **2015**.
- Ting Jiang, Tahereh Jafari, Wei Zhong, Steven L. Suib. Advanced mesoporous aluminosilicate adsorbents for siloxane adsorption. University of Connecticut office of economic development, invention disclosure, **2014**.
- Tahereh Jafari, Ting Jiang, Wei Zhong, Steven L. Suib. Advanced mesoporous carbon adsorbent for bio-fuel clean-up. Fraunhofer USA, Patent F0739.70003US01, application filed, **2014**.
- Tahereh Jafari, Ting Jiang, Wei Zhong, Steven L. Suib. Advanced mesoporous carbon adsorbent for bio-fuel clean-up. University of Connecticut office of economic development, invention disclosure, **2014**.

- Wei Zhong, Ting Jiang, Tahereh Jafari, Steven L. Suib, UCT Materials and other Manganese Materials for Competitive Organic Sulfur Adsorption. University of Connecticut office of economic development, invention disclosure, **2015**.

Book chapters

- Andrew Meguerdichian, Ting Jiang, Wei Zhong. Steven L. Suib. Chapter 8, All-oxides Nanoheterostructures (synthesis, characterization, and properties) in Hybrid Nanocrystal Architectures: Synthesis, Properties, and Applications. Imperial College Press. **2016**. In print.
- Tahereh Jafari, Andrew Meguerdichian, Ting Jiang, Abdelhamid El-Sawy, Steven L. Suib. Chapter, Non-precious metal oxide and metal-free catalysts for energy storage and conversion in Advanced Electrode Materials of Advanced Materials Book Series, WILEY-Scrivener Publisher, USA. **2016**. In print.

Conference presentations

- Ting Jiang, Shoucheng Du, and et al. Enhanced photocatalytic activity in dye degradation by UCT mesoporous iron oxides. *2015 AIChE annual meeting*, Nov. 2015, Salt Lake City, UT, USA.
- Ting Jiang, Wei Zhong, and et al. Removal of siloxane from biogas by adsorption on mesoporous aluminosilicate (UCT-15). *2015 AIChE annual meeting*, Nov. 2015, Salt Lake City, UT, USA.
- Ting Jiang, Shoucheng Du, and et al. Magnetically recyclable mesoporous iron oxide supported Pd nanoparticles for catalytic nitrobenzene hydrogenation. *250th ACS National Meeting*, August 2015, Boston, MA, USA.

- Ting Jiang, Tahereh Jafari, and et al. Adsorption of siloxane for biogas cleanup using UCT mesoporous adsorbents. *11th Internation Conference on Ceramic Materials and Components for Energy and Environmental Applications*, June 2015, Vancouver, Canada.
- Zhu Luo, Altug Poyraz, Chung-Hao Kuo, Ran Miao, Yongtao Meng, Sheng-Yu Chen, Ting Jiang, Steven Suib. Thermally stable, mixed phase (anatase/rutile) mesoporous titanium dioxide nanoparticles for visible light photocatalytic activity. *250th ACS National Meeting*, August 2015, Boston, MA, USA.
- Tahereh Jafari, Ting Jiang, Wei Zhong, Steven L. Suib. Modified mesoporous silica for efficient siloxane capture. *252nd ACS National Meeting*, Aug. 2016, Philadelphia, PA, USA.

REFERENCES

[1] L. Zhao, H. Qin, R. Wu, H. Zou, Recent advances of mesoporous materials in sample preparation, J. Chromatogr. A. 1228 (2012) 193–204. doi:10.1016/j.chroma.2011.09.051.

[2] Y. Ren, Z. Ma, P.G. Bruce, Ordered mesoporous metal oxides: synthesis and applications, Chem. Soc. Rev. 41 (2012) 4909–4927. doi:10.1039/c2cs35086f.

[3] A.S. Poyraz, C.-H. Kuo, S. Biswas, C.K. King'ondu, S.L. Suib, A general approach to crystalline and monomodal pore size mesoporous materials, Nat. Commun. 4 (2013) 2952. doi:10.1038/ncomms3952.

[4] P. Kumar, K.V. Agrawal, M. Tsapatsis, K.A. Mkhoyan, Quantification of thickness and wrinkling of exfoliated two-dimensional zeolite nanosheets, Nat. Commun. 6 (2015) 1–7. doi:10.1038/ncomms8128.

[5] C. Calvert, R. Joesten, K. Ngala, J. Villegas, A. Morey, X. Shen, et al., Synthesis, characterization, and rietveld refinement of tungsten-framework-doped porous manganese oxide (K-OMS-2) material, Chem. Mater. 20 (2008) 6382–6388. doi:10.1021/cm801146m.

[6] C.H. Chen, E.C. Njagi, S.Y. Chen, D.T. Horvath, L. Xu, A. Morey, et al., Structural Distortion of Molybdenum-Doped Manganese Oxide Octahedral Molecular Sieves for Enhanced Catalytic Performance, Inorg. Chem. 54 (2015) 10163–10171. doi:10.1021/acs.inorgchem.5b00906.

[7] F.C. Meldrum, R. Seshadri, Porous gold structures through templating by echinoid skeletal plates, Chem. Commun. (2000) 29–30. doi:10.1039/a907074e.

[8] Y. Ren, Z. Ma, P.G. Bruce, Ordered mesoporous metal oxides: synthesis and applications., Chem. Soc. Rev. 41 (2012) 4909–27. doi:10.1039/c2cs35086f.

[9] M. Niederberger, N. Pinna, Metal Oxide Nanoparticles in Organic Solvents: Synthesis, Formation, Assembly and Application, 2009. doi:10.1007/978-1-84882-671-7.

[10] A.S. Poyraz, Y. Meng, S. Biswas, S.L. Suib, Chapter 31 Mesoporous TM Oxide Materials by Surfactant-Assisted Soft Templating, in: Perovskites Relat. Mix. Oxides Concepts Appl., 2016: pp. 701–768.

[11] K.J. Klabunde, Nanoscale Materials in Chemistry, 2nd editio, Wiley-Interscience, 2001. doi:10.1002/0471220620.

[12] A. Taguchi, F. Schüth, Ordered mesoporous materials in catalysis, Microporous Mesoporous Mater. 77 (2005) 1–45. doi:10.1016/j.micromeso.2004.06.030.

[13] L. Lucarelli, V. Nadtochenko, J. Kiwi, Environmental photochemistry: quantitative adsorption and FTIR studies during the TiO2-photocatalyzed degradation of Orange II, Langmuir. 16 (2000) 1102–1108. doi:10.1021/la990272j.

[14] K. Rajeshwar, M.E. Osugi, W. Chanmanee, C.R. Chenthamarakshan, M.V.B. Zanoni, P. Kajitvichyanukul, et al., Heterogeneous photocatalytic treatment of organic dyes in air and aqueous media, J. Photochem. Photobiol. C Photochem. Rev. 9 (2008) 171–192. doi:10.1016/j.jphotochemrev.2008.09.001.

[15] C. a. Martínez-Huitle, E. Brillas, Decontamination of wastewaters containing synthetic organic dyes by electrochemical methods: A general review, Appl. Catal. B Environ. 87 (2009) 105–145. doi:10.1016/j.apcatb.2008.09.017.

[16] Y.H. Huang, S.T. Tsai, Y.F. Huang, C.Y. Chen, Degradation of commercial azo dye reactive Black B in photo/ferrioxalate system, J. Hazard. Mater. 140 (2007) 382–388. doi:10.1016/j.jhazmat.2006.10.083.

[17] S. Wang, A Comparative study of Fenton and Fenton-like reaction kinetics in decolourisation of wastewater, Dye. Pigment. 76 (2008) 714–720. doi:10.1016/j.dyepig.2007.01.012.

[18] E. Neyens, J. Baeyens, A review of classic Fenton's peroxidation as an advanced oxidation technique, J. Hazard. Mater. 98 (2003) 33–50. doi:10.1016/S0304-3894(02)00282-0.

[19] M.S. Lucas, J.A. Peres, Decolorization of the azo dye Reactive Black 5 by Fenton and photo-Fenton oxidation, Dye. Pigment. 71 (2006) 236–244. doi:10.1016/j.dyepig.2005.07.007.

[20] C.L. Hsueh, Y.H. Huang, C.C. Wang, C.Y. Chen, Degradation of azo dyes using low iron concentration of Fenton and Fenton-like system., Chemosphere. 58 (2005) 1409–1414. doi:10.1016/j.chemosphere.2004.09.091.

[21] J. Herney-Ramirez, M.A. Vicente, L.M. Madeira, Heterogeneous photo-Fenton oxidation with pillared clay-based catalysts for wastewater treatment: A review, Appl. Catal. B Environ. 98 (2010) 10–26. doi:10.1016/j.apcatb.2010.05.004.

[22] J. Ma, W. Song, C. Chen, W. Ma, J. Zhao, Y. Tang, Fenton degradation of organic compounds promoted by dyes under visible irradiation., Environ. Sci. Technol. 39 (2005) 5810–5815. http://www.ncbi.nlm.nih.gov/pubmed/16124319.

[23] X. Zhou, J. Lan, G. Liu, K. Deng, Y. Yang, G. Nie, et al., Facet-mediated photodegradation of organic dye over hematite architectures by visible light, Angew. Chemie - Int. Ed. 51 (2012) 178–182. doi:10.1002/anie.201105028.

[24] Y. Dong, W. Dong, Y. Cao, Z. Han, Z. Ding, Preparation and catalytic activity of Fe alginate gel beads for oxidative degradation of azo dyes under visible light irradiation, in: Catal.

Today, Elsevier B.V., 2011: pp. 346–355. doi:10.1016/j.cattod.2011.03.035.

[25] K. Wu, Y. Xie, J. Zhao, H. Hidaka, Photo-Fenton degradation of a dye under visible light irradiation, J. Mol. Catal. A Chem. 144 (1999) 77–84. doi:10.1016/S1381-1169(98)00354-9.

[26] H. Park, W. Choi, Visible light and Fe(III)-mediated degradation of Acid Orange 7 in the absence of H2O2, J. Photochem. Photobiol. A Chem. 159 (2003) 241–247. doi:10.1016/S1010-6030(03)00141-2.

[27] J. Fernandez, M.R. Dhananjeyan, J. Kiwi, Y. Senuma, J. Hilborn, Evidence for Fenton Photoassisted Processes Mediated by Encapsulated Fe ions at Biocompatible pH Values, J. Phys. Chem. B. 104 (2000) 5298–5301. doi:10.1021/jp9943777.

[28] T. Yuranova, O. Enea, E. Mielczarski, J. Mielczarski, P. Albers, J. Kiwi, Fenton immobilized photo-assisted catalysis through a Fe/C structured fabric, Appl. Catal. B Environ. 49 (2004) 39–50. doi:10.1016/j.apcatb.2003.11.008.

[29] S.J. Hug, O. Leupin, Iron-catalyzed oxidation of Arsenic(III) by oxygen and by hydrogen peroxide: pH-dependent formation of oxidants in the Fenton reaction, Environ. Sci. Technol. 37 (2003) 2734–2742. doi:10.1021/es026208x.

[30] M.L. Kremer, The fenton reaction. Dependence of the rate on pH, J. Phys. Chem. A. 107 (2003) 1734–1741. doi:10.1021/jp020654p.

[31] J. Feng, X. Hu, L.Y. Po, Discoloration and mineralization of Orange II using different heterogeneous catalysts containing Fe: A comparative study, Environ. Sci. Technol. 38 (2004) 5773–5778. doi:10.1021/es049811j.

[32] M. Cheng, W. Ma, J. Li, Y. Huang, J. Zhao, Y.X. Wen, et al., Visible-Light-Assisted

Degradation of Dye Pollutants over Fe(III)-Loaded Resin in the Presence of H2O2 at Neutral pH Values, Environ. Sci. Technol. 38 (2004) 1569–1575. doi:10.1021/es034442x.

[33] W. Du, Q. Sun, X. Lv, Y. Xu, Enhanced activity of iron oxide dispersed on bentonite for the catalytic degradation of organic dye under visible light, Catal. Commun. 10 (2009) 1854–1858. doi:10.1016/j.catcom.2009.06.014.

[34] T.W. Kim, H.W. Ha, M.J. Paek, S.H. Hyun, I.H. Baek, J.H. Choy, et al., Mesoporous iron oxide-layered titanate nanohybrids: Soft-chemical synthesis, characterization, and photocatalyst application, J. Phys. Chem. C. 112 (2008) 14853–14862. doi:10.1021/jp805488h.

[35] N. Panda, H. Sahoo, S. Mohapatra, Decolourization of Methyl Orange using Fenton-like mesoporous Fe(2)O(3)-SiO(2) composite., J. Hazard. Mater. 185 (2011) 359–365. doi:10.1016/j.jhazmat.2010.09.042.

[36] P. Sangeetha, K. Shanthi, K.S.R. Rao, B. Viswanathan, P. Selvam, Hydrogenation of nitrobenzene over palladium-supported catalysts-Effect of support, Appl. Catal. A Gen. 353 (2009) 160–165. doi:10.1016/j.apcata.2008.10.044.

[37] C.H. Li, Z.X. Yu, K.F. Yao, S.F. Ji, J. Liang, Nitrobenzene hydrogenation with carbon nanotube-supported platinum catalyst under mild conditions, J. Mol. Catal. A Chem. 226 (2005) 101–105. doi:10.1016/j.molcata.2004.09.046.

[38] N. Bouchenafa-Saïb, P. Grange, P. Verhasselt, F. Addoun, V. Dubois, Effect of oxidant treatment of date pit active carbons used as Pd supports in catalytic hydrogenation of nitrobenzene, Appl. Catal. A Gen. 286 (2005) 167–174. doi:10.1016/j.apcata.2005.02.022.

[39] M. Turáková, M. Králik, P. Lehocký, Ľ. Pikna, M. Smrčová, D. Remeteiová, et al.,

Influence of preparation method and palladium content on Pd/C catalysts activity in the liquid phase hydrogenation of nitrobenzene to aniline, Appl. Catal. A Gen. 476 (2014) 103–112. doi:10.1016/j.apcata.2014.02.025.

[40] L.B. Okhlopkova, A.S. Lisitsyn, V.A. Likholobov, M. Gurrath, H.P. Boehm, Properties of Pt/C and Pd/C catalysts prepared by reduction with hydrogen of adsorbed metal chlorides Influence of pore structure of the support, Appl. Catal. A Gen. 204 (2000) 229–240. doi:0926-860X/00/$.

[41] X.X. Han, Q. Chen, R.X. Zhou, Study on the hydrogenation of p-chloronitrobenzene over carbon nanotubes supported platinum catalysts modified by Mn, Fe, Co, Ni and Cu, J. Mol. Catal. A Chem. 277 (2007) 210–214. doi:10.1016/j.molcata.2007.07.052.

[42] Z. Sun, Y. Zhao, Y. Xie, R. Tao, H. Zhang, C. Huang, et al., The solvent-free selective hydrogenation of nitrobenzene to aniline: an unexpected catalytic activity of ultrafine Pt nanoparticles deposited on carbon nanotubes, Green Chem. 12 (2010) 1007–1011. doi:10.1039/c002391d.

[43] Y.-M. Lu, H.-Z. Zhu, W.-G. Li, B. Hu, S.-H. Yu, Size-controllable palladium nanoparticles immobilized on carbon nanospheres for nitroaromatic hydrogenation, J. Mater. Chem. A. 1 (2013) 3783–3788. doi:10.1039/C3TA00159H.

[44] P. Rodriguez, F. Simescu-Lazar, V. Meille, T. Bah, S. Pallier, I. Fournel, Carbon-coated structured supports. Preparation and use for nitrobenzene hydrogenation, Appl. Catal. A Gen. 427-428 (2012) 66–72. doi:10.1016/j.apcata.2012.03.031.

[45] F. Simescu-Lazar, V. Meille, S. Pallier, E. Chaînet, C. De Bellefon, Regeneration of deactivated catalysts coated on foam and monolith: Example of Pd/C for nitrobenzene

hydrogenation, Appl. Catal. A Gen. 453 (2013) 28–33. doi:10.1016/j.apcata.2012.11.044.

[46] D. Cropek, P.A. Kemme, O. V. Makarova, L.X. Chen, T. Rajh, Selective photocatalytic decomposition of nitrobenzene using surface modified TiO2 nanoparticles, J. Phys. Chem. C. 112 (2008) 8311–8318. doi:10.1021/jp712137x.

[47] H. Mangal, A. Saxena, A.S. Rawat, V. Kumar, P.K. Rai, M. Datta, Adsorption of nitrobenzene on zero valent iron loaded metal oxide nanoparticles under static conditions, Microporous Mesoporous Mater. 168 (2013) 247–256. doi:10.1016/j.micromeso.2012.10.006.

[48] H.U. Blaser, H. Steiner, M. Studer, Selective catalytic hydrogenation of functionalized nitroarenes: An update, ChemCatChem. 1 (2009) 210–221. doi:10.1002/cctc.200900129.

[49] S. Banerjee, V. Balasanthiran, R.T. Koodali, G.A. Sereda, Pd-MCM-48: a novel recyclable heterogeneous catalyst for chemo- and regioselective hydrogenation of olefins and coupling reactions., Org. Biomol. Chem. 8 (2010) 4316–4321. doi:10.1039/c0ob00183j.

[50] J.R. Chang, H.M. Lin, S.W. Cheng, C.K. Tseng, D.L. Tzou, S.G. Shyu, EXAFS investigation of the morphology of immobilized Rh(PPh 3)3Cl on phosphinated MCM-41, J. Mol. Catal. A Chem. 329 (2010) 27–35. doi:10.1016/j.molcata.2010.06.013.

[51] N.R. Champness, The future of metal–organic frameworks, Dalt. Trans. 40 (2011) 10638–10642. doi:10.1039/c1dt11184a.

[52] J. Liu, S. Zou, L. Xiao, J. Fan, Well-dispersed Bimetallic Nanoparticls confined in Mesoporous Metal Oxides and Their Optimized Catalytic Activity for Nitrobenzene Hydrogenation, Catal. Sci. Technol. 4 (2013) 441–446. doi:10.1039/C3CY00689A.

[53] X. Yu, M. Wang, H. Li, Study on the nitrobenzene hydrogenation over a Pd-B / SiO 2

amorphous catalyst, Appl. Catal. A Gen. 202 (2000) 17–22. doi:0926-860X/00/$.

[54] L.H. Reddy, J.L. Arias, J. Nicolas, P. Couvreur, Magnetic nanoparticles: design and characterization, toxicity and biocompatibility, pharmaceutical and biomedical applications., Chem. Rev. 112 (2012) 5818–5878. doi:10.1021/cr300068p.

[55] A.H. Lu, E.L. Salabas, F. Schüth, Magnetic nanoparticles: Synthesis, protection, functionalization, and application, Angew. Chemie - Int. Ed. 46 (2007) 1222–1244. doi:10.1002/anie.200602866.

[56] D.K. Yi, S.S. Lee, J.Y. Ying, Synthesis and applications of magnetic nanocomposite catalysts, Chem. Mater. 18 (2006) 2459–2461. doi:10.1021/cm052885p.

[57] Y. Zhu, L.P. Stubbs, F. Ho, R. Liu, C.P. Ship, J.A. Maguire, et al., Magnetic Nanocomposites: A New Perspective in Catalysis, ChemCatChem. 2 (2010) 365–374. doi:10.1002/cctc.200900314.

[58] L. Aschwanden, B. Panella, P. Rossbach, B. Keller, A. Baiker, Magnetically separable gold catalyst for the aerobic oxidation of amines, ChemCatChem. 1 (2009) 111–115. doi:10.1002/cctc.200900085.

[59] H. Woo, K. Lee, K.H. Park, Optimized Dispersion and Stability of Hybrid Fe 3 O 4 /Pd Catalysts in Water for Suzuki Coupling Reactions: Impact of Organic Capping Agents, ChemCatChem. 6 (2014) 1635–1640. doi:10.1002/cctc.201400067.

[60] J.M. Thomas, B.F.G. Johnson, R. Raja, G. Sankar, P. a Midgley, High-performance nanocatalysts for single-step hydrogenations, Acc. Chem. Res. 36 (2003) 20–30. doi:10.1021/ar990017q.

[61] A. Roucoux, J. Schulz, H. Patin, Reduced transition metal colloids: A novel family of

reusable catalysts?, Chem. Rev. 102 (2002) 3757–3778. doi:10.1021/cr010350j.

[62] G.C. Torres, E.L. Jablonski, G.T. Baronett, A.A. Castro, S.R. De Miguel, O.A. Scelza, et al., Effect of the carbon pre-treatment on the properties and performance for nitrobenzene hydrogenation of Pt/C catalysts, Appl. Catal. A Gen. 161 (1997) 213–226. doi:0926-860X/97/.

[63] L.S. Ferreira, J.O. Trierweiler, Modeling and simulation of the polymeric nanocapsule formation process, in: IFAC Proc. Vol., 2009: pp. 405–410. doi:10.1002/aic.

[64] J. Hill, E. Nelson, D. Tilman, S. Polasky, D. Tiffany, Environmental, economic, and energetic costs and benefits of biodiesel and ethanol biofuels, Proc. Natl. Acad. Sci. 103 (2006) 11206–11210. doi:10.1073/pnas.0604600103.

[65] N.S. Lewis, D.G. Nocera, Powering the planet: Chemical challenges in solar energy utilization, Proc. Natl. Acad. Sci. 103 (2006) 15729–15735. doi:10.1073/pnas.0603395103.

[66] S. Du, Y. Sun, D.P. Gamliel, J.A. Valla, G.M. Bollas, Catalytic pyrolysis of miscanthus×giganteus in a spouted bed reactor, Bioresour. Technol. 169 (2014) 188–197. doi:10.1016/j.biortech.2014.06.104.

[67] S. Du, J.A. Valla, G.M. Bollas, Characteristics and origin of char and coke from fast and slow, catalytic and thermal pyrolysis of biomass and relevant model compounds, Green Chem. 15 (2013) 3214. doi:10.1039/c3gc41581c.

[68] Y. Zhang, L. Jin, K. Sterling, Z. Luo, T. Jiang, R. Miao, et al., Potassium modified layered Ln2O2CO3 (Ln: La, Nd, Sm, Eu) materials: efficient and stable heterogeneous catalysts for biofuel production, Green Chem. 17 (2015) 3600–3608. doi:10.1039/C4GC02429J.

[69] A. Fischer, S. Du, J.A. Valla, G.M. Bollas, The effect of temperature, heating rate, and

ZSM-5 catalyst on the product selectivity of the fast pyrolysis of spent coffee grounds, RSC Adv. 5 (2015) 29252–29261. doi:10.1039/C5RA00212E.

[70] I. Noshadi, B. Kanjilal, S. Du, G.M. Bollas, S.L. Suib, A. Provatas, et al., Catalyzed production of biodiesel and bio-chemicals from brown grease using Ionic Liquid functionalized ordered mesoporous polymer, Appl. Energy. 129 (2014) 112–122. doi:10.1016/j.apenergy.2014.04.090.

[71] J.B. Holm-Nielsen, T. Al Seadi, P. Oleskowicz-Popiel, The future of anaerobic digestion and biogas utilization, Bioresour. Technol. 100 (2009) 5478–5484. doi:10.1016/j.biortech.2008.12.046.

[72] C. Cornejo, A.C. Wilkie, Greenhouse gas emissions and biogas potential from livestock in Ecuador, Energy Sustain. Dev. 14 (2010) 256–266. doi:10.1016/j.esd.2010.09.008.

[73] D. Papadias, S. Ahmed, Biogas impurities and cleanup for fuel cells, Argonne Natl. Lab Biogas Fuel Cells Work. (2012).

[74] R. Dewil, L. Appels, J. Baeyens, Energy use of biogas hampered by the presence of siloxanes, Energy Convers. Manag. 47 (2006) 1711–1722. doi:10.1016/j.enconman.2005.10.016.

[75] M. Yu, H. Gong, Z. Chen, M. Zhang, Adsorption characteristics of activated carbon for siloxanes, J. Environ. Chem. Eng. 1 (2013) 1182–1187. doi:10.1016/j.jece.2013.09.003.

[76] A. Cabrera-Codony, M.A. Montes-Morán, M. Sánchez-Polo, M.J. Martín, R. Gonzalez-Olmos, Biogas upgrading: optimal activated carbon properties for siloxane removal, Environ. Sci. Technol. 48 (2014) 7187–7195. doi:10.1021/es501274a.

[77] M. Schweigkofler, R. Niessner, Removal of siloxanes in biogases., J. Hazard. Mater. B83

(2001) 183–96. doi:0304-3894/01/$.

[78] S.C. Popat, M.A. Deshusses, Biological removal of siloxanes from landfill and digester gases: opportunities and challenges., Environ. Sci. Technol. 42 (2008) 8510–5. http://www.ncbi.nlm.nih.gov/pubmed/19068840.

[79] G. Soreanu, M. Béland, P. Falletta, K. Edmonson, L. Svoboda, M. Al-Jamal, et al., Approaches concerning siloxane removal from biogas - a review, Can. Biosyst. Eng. / Le Genie Des Biosyst. Au Canada. 53 (2011) 8.1–8.18.

[80] M. Ajhar, M. Travesset, S. Yüce, T. Melin, Siloxane removal from landfill and digester gas – a technology overview, Bioresour. Technol. 101 (2010) 2913–2923. doi:10.1016/j.biortech.2009.12.018.

[81] N. de Arespacochaga, C. Valderrama, C. Mesa, L. Bouchy, J.L. Cortina, Biogas deep clean-up based on adsorption technologies for solid oxide fuel cell applications, Chem. Eng. J. 255 (2014) 593–603. doi:10.1016/j.cej.2014.06.072.

[82] S. Giraudet, B. Boulinguiez, P. Le Cloirec, Adsorption and electrothermal desorption of volatile rrganic compounds and siloxanes onto an activated carbon fiber cloth for biogas purification, Energy & Fuels. 28 (2014) 3924–3932. doi:10.1021/ef500600b.

[83] S. Nam, W. Namkoong, J.-H. Kang, J.-K. Park, N. Lee, Adsorption characteristics of siloxanes in landfill gas by the adsorption equilibrium test, Waste Manag. 33 (2013) 2091–2098. doi:10.1016/j.wasman.2013.03.024.

[84] D.R. Ortega, A. Subrenat, Siloxane treatment by adsorption into porous materials, Environ. Technol. 30 (2009) 1073–1083. doi:10.1080/09593330903057540.

[85] T. Montanari, E. Finocchio, I. Bozzano, G. Garuti, A. Giordano, C. Pistarino, et al.,

Purification of landfill biogases from siloxanes by adsorption: a study of silica and 13X zeolite adsorbents on hexamethylcyclotrisiloxane separation, Chem. Eng. J. 165 (2010) 859–863. doi:10.1016/j.cej.2010.10.032.

[86] K. Oshita, Y. Ishihara, M. Takaoka, N. Takeda, T. Matsumoto, S. Morisawa, et al., Behaviour and adsorptive removal of siloxanes in sewage sludge biogas, Water Sci. Technol. 61 (2010) 2003. doi:10.2166/wst.2010.101.

[87] S.-H. Lee, W. Cho, T.-Y. Song, H. Kim, W.-J. Lee, Y.-C. Lee, et al., Removal process for octamethylcyclotetrasiloxane from biogas in sewage treatment plant, J. Ind. Eng. Chem. 7 (2001) 276–280.

[88] E.P.A. Clean Air Technology, Choosing an adsorption system for VOC: carbon, zeolite or polymers?, 1999. http://www.epa.gov/ttn/catc.

[89] A. Cabrera-Codony, R. Gonzalez-Olmos, M.J. Martín, Regeneration of siloxane-exhausted activated carbon by advanced oxidation processes, J. Hazard. Mater. 285 (2015) 501–508. doi:10.1016/j.jhazmat.2014.11.053.

[90] R.G. Horn, J.N. Israelachvili, Direct measurement of structural forces between two surfaces in a nonpolar liquid, J. Chem. Phys. 75 (1981) 1400–1411. doi:0021-9606/81/151400-12$01.00.

[91] T. Jafari, I. Noshadi, N. Khakpash, S.L. Suib, Superhydrophobic and stable mesoporous polymeric adsorbent for siloxane removal: D4 super-adsorbent, J. Mater. Chem. A. 3 (2015) 5023–5030. doi:10.1039/C4TA06593J.

[92] S. Hay, T. Obee, Z. Luo, T. Jiang, Y. Meng, J. He, et al., The viability of photocatalysis for air purification, Molecules. 20 (2015) 1319–1356. doi:10.3390/molecules20011319.

[93] T. Jiang, A.S. Poyraz, A. Iyer, Y. Zhang, Z. Luo, W. Zhong, et al., Synthesis of mesoporous iron oxides by an inverse micelle method and their application in the degradation of orange II under visible light at neutral pH, J. Phys. Chem. C. 119 (2015) 10454–10468. doi:10.1021/acs.jpcc.5b02057.

[94] Z. Luo, A.S. Poyraz, C. Kuo, R. Miao, Y. Meng, S.-Y. Chen, et al., Crystalline mixed phase (anatase/rutile) mesoporous titanium dioxides for visible light photocatalytic activity, Chem. Mater. 27 (2015) 6–17. doi:10.1021/cm5035112.

[95] D.L.A. De Faria, S.V. Silva, M.T. de Oliveira, Raman Microspectroscopy of Some Iron Oxides and Oxyhydroxides, J. Raman Spectrosc. 28 (1997) 873–878. doi:0377È0486/97/110873È06.

[96] O.N. Shebanova, P. Lazor, Raman study of magnetite (Fe3O4): Laser-induced thermal effects and oxidation, J. Raman Spectrosc. 34 (2003) 845–852. doi:10.1002/jrs.1056.

[97] P. Sangeetha, P. Seetharamulu, K. Shanthi, S. Narayanan, K.S. Rama Rao, Studies on Mg-Al oxide hydrotalcite supported Pd catalysts for vapor phase hydrogenation of nitrobenzene, J. Mol. Catal. A Chem. 273 (2007) 244–249. doi:10.1016/j.molcata.2007.03.020.

[98] Y. Chen, J. Qiu, X. Wang, J. Xiu, Preparation and application of highly dispersed gold nanoparticles supported on silica for catalytic hydrogenation of aromatic nitro compounds, J. Catal. 242 (2006) 227–230. doi:10.1016/j.jcat.2006.05.028.

[99] C. Kartusch, M. Makosch, J. Sá, K. Hungerbuehler, J.A. VanBokhoven, The Dynamic Structure of Gold Supported on Ceria in the Liquid Phase Hydrogenation of Nitrobenzene, ChemCatChem. 4 (2012) 236–242. doi:10.1002/cctc.201100187.

[100] V.A. Drits, B.A. Sakharov, A.L. Salyn, A. Manceau, Structural MODEL FOR

FERRIHYDRITE, Clay Miner. 28 (1993) 185–207.

[101] U. Schwertmann, R.M. Cornell, Iron Oxides in the Laboratory. Preparation and Characterization, 2000. doi:10.1180/claymin.1992.027.3.14.

[102] F.M. Michel, L. Ehm, G. Liu, W.Q. Han, S.M. Antao, P.J. Chupas, et al., Similarities in 2- and 6-line ferrihydrite based on pair distribution function analysis of X-ray total scattering, Chem. Mater. 19 (2007) 1489–1496. doi:10.1021/cm062585n.

[103] A.S. Poyraz, W. Song, D. Kriz, C.H. Kuo, M.S. Seraji, S.L. Suib, Crystalline mesoporous K2-xMn8O16 and ε-MnO2 by mild transformations of amorphous mesoporous manganese oxides and their enhanced redox properties, ACS Appl. Mater. Interfaces. 6 (2014) 10986–10991. doi:10.1021/am502846e.

[104] M. Lübbe, A.M. Gigler, R.W. Stark, W. Moritz, Identification of iron oxide phases in thin films grown on Al2O3(0001) by Raman spectroscopy and X-ray diffraction, Surf. Sci. 604 (2010) 679–685. doi:10.1016/j.susc.2010.01.015.

[105] L. Bellot-Gurlet, D. Neff, S. Réguer, J. Monnier, M. Saheb, P. Dillmann, Raman Studies of Corrosion Layers Formed on Archaeological Irons in Various Media, J. Nano Res. 8 (2009) 147–156. doi:10.4028/www.scientific.net/JNanoR.8.147.

[106] L. Zhang, W. Wang, L. Zhou, M. Shang, S. Sun, Fe3O4 coupled BiOCl: A highly efficient magnetic photocatalyst, Appl. Catal. B Environ. 90 (2009) 458–462. doi:10.1016/j.apcatb.2009.04.005.

[107] W. Wang, Y. Xu, D.I.C. Wang, Z. Li, Recyclable nanobiocatalyst for enantioselective sulfoxidation: Facile fabrication and high performance of chloroperoxidase-coated magnetic nanoparticles with iron oxide core and polymer shell, J. Am. Chem. Soc. 131

(2009) 12892–12893. doi:10.1021/ja905477j.

[108] J. Ge, Q. Zhang, T. Zhang, Y. Yin, Core-satellite nanocomposite catalysts protected by a porous silica shell: Controllable reactivity, high stability, and magnetic recyclability, Angew. Chemie - Int. Ed. 47 (2008) 8924–8928. doi:10.1002/anie.200803968.

[109] T. Jiang, S. Du, T. Jafari, W. Zhong, Y. Sun, W. Song, et al., Synthesis of mesoporous γ-Fe2O3 supported palladium nanoparticles and investigation of their roles as magnetically recyclable catalysts for nitrobenzene hydrogenation, Appl. Catal. A Gen. 502 (2015) 105–113. doi:10.1016/j.apcata.2015.05.013.

[110] W. Song, A.S. Poyraz, Y. Meng, Z. Ren, S.-Y. Chen, S.L. Suib, Mesoporous Co3O4 with controlled porosity: inverse micelle synthesis and high-performance catalytic CO oxidation at −60 °C, Chem. Mater. 26 (2014) 4629–4639. doi:10.1021/cm502106v.

[111] S.A. Bagshaw, I.J. Bruce, Rapid calcination of high quality mesostructured MCM-41, MSU-X, and SBA-15 silicate materials: a step towards continuous processing?, Microporous Mesoporous Mater. 109 (2008) 199–209. doi:10.1016/j.micromeso.2007.04.042.

[112] R. Schmidt, M. Stöcker, E. Hansen, D. Akporiaye, O.H. Ellestad, MCM-41: a model system for adsorption studies on mesoporous materials, Microporous Mater. 3 (1995) 443–448. doi:10.1016/0927-6513(94)00055-Z.

[113] J.C. Groen, L.A.A. Peffer, J. Pérez-Ramírez, Pore size determination in modified micro- and mesoporous materials. Pitfalls and limitations in gas adsorption data analysis, Microporous Mesoporous Mater. 60 (2003) 1–17. doi:10.1016/S1387-1811(03)00339-1.

[114] P. Klobes, K. Meyer, R.G. Munro, Porosity and specific surface area measurements for solid

materials, National Institute of Standards and Technology, Washington, 2006.

[115] S. Storck, H. Bretinger, W.F. Maier, Characterization of micro- and mesoporous solids by physisorption methods and pore-size analysis, Appl. Catal. A Gen. 174 (1998) 137–146. doi:10.1016/S0926-860X(98)00164-1.

[116] L. Pasqua, P. Frontera, F. Testa, R. Aiello, Preparation of mesoporous silica using low cost green reactants, Stud. Surf. Sci. Catal. 154 (2004) 511–518. doi:10.1016/S0167-2991(04)80844-9.

[117] M.T. Bore, M.P. Mokhonoana, T.L. Ward, N.J. Coville, A.K. Datye, Synthesis and reactivity of gold nanoparticles supported on transition metal doped mesoporous silica, Microporous Mesoporous Mater. 95 (2006) 118–125. doi:10.1016/j.micromeso.2006.05.007.

[118] Y. Xia, R. Mokaya, On the hydrothermal stability of mesoporous aluminosilicate MCM-48 materials, J. Phys. Chem. B. 107 (2003) 6954–6960. doi:10.1021/jp0270147.

[119] Z. El verrichi, L. Cherif, O. Orsen, J. Fraissard, J. Tessonnier, E. Vanhaecke, et al., Ga doped SBA-15 as an active and stable catalyst for Friedel–Crafts liquid-phase acylation, Appl. Catal. A Gen. 298 (2006) 194–202. doi:10.1016/j.apcata.2005.10.005.

[120] K. Bendahou, L. Cherif, S. Siffert, H.L. Tidahy, H. Benaïssa, A. Aboukaïs, The effect of the use of lanthanum-doped mesoporous SBA-15 on the performance of Pt/SBA-15 and Pd/SBA-15 catalysts for total oxidation of toluene, Appl. Catal. A Gen. 351 (2008) 82–87. doi:10.1016/j.apcata.2008.09.001.

[121] X. Yang, W. Dai, H. Chen, Y. Cao, H. Li, H. He, et al., Novel efficient and green approach to the synthesis of glutaraldehyde over highly active W-doped SBA-15 catalyst, J. Catal.

229 (2005) 259–263. doi:10.1016/j.jcat.2004.10.009.

[122] C. Gérardin, J. Reboul, M. Bonne, B. Lebeau, Ecodesign of ordered mesoporous silica materials, Chem. Soc. Rev. 42 (2013) 4217. doi:10.1039/c3cs35451b.

[123] F. Kleitz, W. Schmidt, F. Schüth, Evolution of mesoporous materials during the calcination process: structural and chemical behavior, Microporous Mesoporous Mater. 44-45 (2001) 95–109. doi:10.1016/S1387-1811(01)00173-1.

[124] J.M. Thomas, W.J. Thomas, Principles and Practice of Heterogeneous Catalysis, 1997.

[125] L.-S. Zhong, J.-S. Hu, H.-P. Liang, A.-M. Cao, W.-G. Song, L.-J. Wan, Self-Assembled 3D Flowerlike Iron Oxide Nanostructures and Their Application in Water Treatment, Adv. Mater. 18 (2006) 2426–2431. doi:10.1002/adma.200600504.

[126] H. Cui, Y. Liu, W. Ren, Structure switch between α-Fe2O3, γ-Fe2O3 and Fe3O4 during the large scale and low temperature sol-gel synthesis of nearly monodispersed iron oxide nanoparticles, Adv. Powder Technol. 24 (2013) 93–97. doi:10.1016/j.apt.2012.03.001.

[127] W. Du, Y. Xu, Y. Wang, Photoinduced degradation of orange II on different iron (Hydr)oxides in aqueous suspension: Rate enhancement on addition of hydrogen peroxide, silver nitrate, and sodium fluoride, Langmuir. 24 (2008) 175–181. doi:10.1021/la7021165.

[128] F. Herrera, A. Lopez, G. Mascolo, P. Albers, J. Kiwi, Catalytic combustion of Orange II on hematite Surface species responsible for the dye degradation, Appl. Catal. B Environ. 29 (2001) 147–162. doi:0926-3373/01/$.

[129] B. Saha, S. Das, J. Saikia, G. Das, Preferential and enhanced adsorption of different dyes on iron oxide nanoparticles: A comparative study, J. Phys. Chem. C. 115 (2011) 8024–8033. doi:10.1021/jp109258f.

[130] J. Joseph, E.D. Jemmis, Red-, blue-, or no-shift in hydrogen bonds: A unified explanation, J. Am. Chem. Soc. 129 (2007) 4620–4632. doi:10.1021/ja067545z.

[131] J. Bandara, J.A. Mielczarski, J. Kiwi, 1. Molecular Mechanism of Surface Recognition. Azo Dyes Degradation on Fe, Ti, and Al Oxides through Metal Sulfonate Complexes, Langmuir. 15 (1999) 7670–7679. doi:10.1021/la9900270.

[132] J. Bandara, J. a. Mielczarski, J. Kiwi, 2. Photosensitized Degradation of Azo Dyes on Fe, Ti, and Al Oxides. Mechanism of Charge Transfer during the Degradation, Langmuir. 15 (1999) 7680–7687. doi:10.1021/la990030j.

[133] A. Iyer, J. Del-Pilar, C.K. King'ondu, E. Kissel, H.F. Garces, H. Huang, et al., Water Oxidation Catalysis using Amorphous Manganese Oxides, Octahedral Molecular Sieves (OMS-2), and Octahedral Layered (OL-1) Manganese Oxide Structures, J. Phys. Chem. C. 116 (2012) 6474–6483. doi:10.1021/jp2120737.

[134] M. Perez, F. Torrades, J.A. Garcia-Hortal, X. Domenech, J. Peral, Removal of organic contaminants in paper pulp treatment effluents under Fenton and photo-Fenton conditions, Appl. Catal. B Environ. 36 (2002) 63–74. doi:0926-3373/02/$.

[135] J. Bandara, C. Morrison, J. Kiwi, C. Pulgarin, P. Peringer, Degradation/decoloration of concentrated solutions of Orange II. Kinetics and quantum yield for sunlight induced reactions via Fenton type reagents, J. Photochem. Photobiol. A Chem. 99 (1996) 57–66. doi:10.1016/1010-6030(96)04339-0.

[136] a. Gutowska, J. Kałuzna-Czaplińska, W.K. Jóźwiak, Degradation mechanism of Reactive Orange 113 dye by H2O2/Fe2+ and ozone in aqueous solution, Dye. Pigment. 74 (2006) 41–46. doi:10.1016/j.dyepig.2006.01.008.

[137] L.C. Abbott, S.N. Batchelor, J.R. Lindsay Smith, J.N. Moore, Reductive reaction mechanisms of the Azo Dye Orange II in aqueous solution and in cellulose: From radical intermediates to products, J. Phys. Chem. A. 113 (2009) 6091–6103. doi:10.1021/jp9021147.

[138] A. Rahmani, M. Zarrabi, Degradation of Azo Dye Reactive Black 5 and Acid Orange 7 by Fenton-Like Mechanism, Iran. J. …. 7 (2010) 87–94. http://www.sid.ir/en/VEWSSID/J_pdf/102420100106.pdf.

[139] M. Stylidi, D.I. Kondarides, X.E. Verykios, Visible light-induced photocatalytic degradation of Acid Orange 7 in aqueous TiO2 suspensions, Appl. Catal. B Environ. 47 (2004) 189–201. doi:10.1016/j.apcatb.2003.09.014.

[140] X. Chen, J. Chen, X. Qiao, D. Wang, X. Cai, Performance of nano-Co3O4/peroxymonosulfate system: Kinetics and mechanism study using Acid Orange 7 as a model compound, Appl. Catal. B Environ. 80 (2008) 116–121. doi:10.1016/j.apcatb.2007.11.009.

[141] S. Bilgi, C. Demir, Identification of photooxidation degradation products of C.I. Reactive Orange 16 dye by gas chromatography-mass spectrometry, Dye. Pigment. 66 (2005) 69–76. doi:10.1016/j.dyepig.2004.08.007.

[142] R. Yan, J. Xu, Y. Zhang, D. Wang, M. Zhang, W. Zhang, Simultaneous Pd catalyst immobilization during synthesis of mesoporous silica, Chem. Eng. J. 200-202 (2012) 559–568. doi:10.1016/j.cej.2012.06.112.

[143] J. Fan, C. Yu, F. Gao, J. Lei, B. Tian, L. Wang, et al., Cubic mesoporous silica with large controllable entrance sizes and advanced adsorption properties, Angew. Chemie - Int. Ed.

42 (2003) 3146–3150. doi:10.1002/anie.200351027.

[144] J. Ge, Z. Zeng, F. Liao, W. Zheng, X. Hong, S.C.E. Tsang, Palladium on iron oxide nanoparticles: the morphological effect of the support in glycerol hydrogenolysis, Green Chem. 15 (2013) 2064–2069. doi:10.1039/C3GC40712H.

[145] X. Gu, Z. Sun, S. Wu, W. Qi, H. Wang, X. Xu, et al., Surfactant-free hydrothermal synthesis of sub-10 nm γ-Fe2O3-polymer porous composites with high catalytic activity for reduction of nitroarenes., Chem. Commun. 49 (2013) 10088–10090. doi:10.1039/c3cc44523b.

[146] S. Kim, E. Kim, B.M. Kim, Fe3O4 nanoparticles: A conveniently reusable catalyst for the reduction of nitroarenes using hydrazine hydrate, Chem. - An Asian J. 6 (2011) 1921–1925. doi:10.1002/asia.201100311.

[147] J. Liu, B. Sun, J. Hu, Y. Pei, H. Li, M. Qiao, Aqueous-phase reforming of ethylene glycol to hydrogen on Pd/Fe 3O4 catalyst prepared by co-precipitation: Metal-support interaction and excellent intrinsic activity, J. Catal. 274 (2010) 287–295. doi:10.1016/j.jcat.2010.07.014.

[148] G.W. Huber, J.W. Shabaker, S.T. Evans, J.A. Dumesic, Aqueous-phase reforming of ethylene glycol over supported Pt and Pd bimetallic catalysts, Appl. Catal. B Environ. 62 (2006) 226–235. doi:10.1016/j.apcatb.2005.07.010.

[149] A. V. Gaikwad, A. Holuigue, M.B. Thathagar, J.E. Ten Elshof, G. Rothenberg, Ion- and atom-leaching mechanisms from palladium nanoparticles in cross-coupling reactions, Chem. - A Eur. J. 13 (2007) 6908–6913. doi:10.1002/chem.200700105.

[150] I.W. Davies, L. Matty, D.L. Hughes, P.J. Reider, Are heterogeneous catalysts precursors to homogeneous catalysts?, J. Am. Chem. Soc. 123 (2001) 10139–10140.

doi:10.1021/ja016877v.

[151] J.-L. Malleron, J.-C. Fiaud, J.-Y. Legros, Handbook of Palladium-catalyzed organic reactions, 1st ed., Academic Press, London, UK, 1997.

[152] M. Makosch, J. Sá, C. Kartusch, G. Richner, J.A. VanBokhoven, K. Hungerbühler, Hydrogenation of Nitrobenzene Over Au/MeO x Catalysts-A Matter of the Support, ChemCatChem. 4 (2012) 59–63. doi:10.1002/cctc.201100299.

[153] A. Corma, P. Concepción, P. Serna, A different reaction pathway for the reduction of aromatic nitro compounds on gold catalysts., Angew. Chem. Int. Ed. Engl. 46 (2007) 7266–7269. doi:10.1002/anie.200700823.

[154] M.M. Sprung, A summary of the reactions of aldehydes with amines., Chem. Rev. 26 (1940) 297–338. doi:10.1021/cr60085a001.

[155] L.D. Pachón, G. Rothenberg, Transition-metal nanoparticles: Synthesis, stability and the leaching issue, Appl. Organomet. Chem. 22 (2008) 288–299. doi:10.1002/aoc.1382.

[156] J.D. Webb, S. MacQuarrie, K. McEleney, C.M. Crudden, Mesoporous silica-supported Pd catalysts: An investigation into structure, activity, leaching and heterogeneity, J. Catal. 252 (2007) 97–109. doi:10.1016/j.jcat.2007.09.007.

[157] F. Su, L. Lv, Y.L. Fang, T. Liu, A.I. Cooper, S.Z. Xiu, Thermally reduced ruthenium nanoparticles as a highly active heterogeneous catalyst for hydrogenation of monoaromatics, J. Am. Chem. Soc. 129 (2007) 14213–14223. doi:10.1021/ja072697v.

[158] J. Ge, Q. Zhang, T. Zhang, Y. Yin, Core-satellite nanocomposite catalysts protected by a porous silica shell: Controllable reactivity, high stability, and magnetic recyclability, Angew. Chemie - Int. Ed. 47 (2008) 8924–8928. doi:10.1002/anie.200803968.

[159] Z. Jin, M. Xiao, Z. Bao, P. Wang, J. Wang, A general approach to mesoporous metal oxide microspheres loaded with noble metal nanoparticles, Angew. Chemie - Int. Ed. 51 (2012) 6406–6410. doi:10.1002/anie.201106948.

[160] A. Chica, K.G. Strohmaier, E. Iglesia, Effects of zeolite structure and aluminum content on thiophene adsorption, desorption, and surface reactions, Appl. Catal. B Environ. 60 (2005) 223–232. doi:10.1016/j.apcatb.2005.02.031.

[161] ChemAxon Marvin, https://www.chemaxon.com/products/marvin/, Https://www.chemaxon.com/products/marvin/. (2015).

[162] T. Matsui, S. Imamura, Removal of siloxane from digestion gas of sewage sludge, Bioresour. Technol. 101 (2010) S29–S32. doi:10.1016/j.biortech.2009.05.037.

[163] L. Sigot, G. Ducom, P. Germain, Adsorption of octamethylcyclotetrasiloxane (D4) on silica gel (SG): retention mechanism, Microporous Mesoporous Mater. 213 (2015) 118–124. doi:10.1016/j.micromeso.2015.04.016.

[164] L.T. Zhuravlev, Concentration of hydroxyl groups on the surface of amorphous silicas, Langmuir. 3 (1987) 316–318. doi:10.1021/la00075a004.

[165] L.T. Zhuravlev, The surface chemistry of amorphous silica. Zhuravlev model, Colloids Surfaces A Physicochem. Eng. Asp. 173 (2000) 1–38. doi:10.1016/S0927-7757(00)00556-2.

[166] P. Linton, J.-C. Hernandez-Garrido, P.A. Midgley, H. Wennerström, V. Alfredsson, Morphology of SBA-15-directed by association processes and surface energies, Phys. Chem. Chem. Phys. 11 (2009) 10973. doi:10.1039/b913755f.

[167] Y.-Y. Fahn, A.-C. Su, P. Shen, Towerlike SBA-15: base and (10)-specific coalescence of a

silicate-encased hexagonal mesophase tailored by nonionic triblock copolymers, Langmuir. 21 (2005) 431–436. doi:10.1021/la0362021.

[168] Y. Wu, M.K.Y. Chan, G. Ceder, Prediction of semiconductor band edge positions in aqueous environments from first principles, Phys. Rev. B - Condens. Matter Mater. Phys. 83 (2011). doi:10.1103/PhysRevB.83.235301.

[169] A. Fujishima, K. Honda, Electrochemical Evidence for the Mechanism of the Primary Stage of Photosynthesis, Bull. Chem. Soc. Jpn. 44 (1971) 1148–1150. doi:10.1246/bcsj.44.1148.

[170] a Fujishima, K. Honda, Electrochemical photolysis of water at a semiconductor electrode., Nature. 238 (1972) 37–38. doi:10.1038/238037a0.

[171] F.E. Osterloh, Inorganic materials as catalysts for photochemical splitting of water, Chem. Mater. 20 (2008) 35–54. doi:10.1021/cm7024203.

[172] H. Kato, K. Asakura, A. Kudo, Highly efficient water splitting into H2 and O2 over lanthanum-doped NaTaO3 photocatalysts with high crystallinity and surface nanostructure, J. Am. Chem. Soc. 125 (2003) 3082–3089. doi:10.1021/ja027751g.

[173] L. Liao, Q. Zhang, Z. Su, Z. Zhao, Y. Wang, Y. Li, et al., Efficient solar water-splitting using a nanocrystalline CoO photocatalyst., Nat. Nanotechnol. 9 (2014) 69–73. doi:10.1038/nnano.2013.272.

[174] K. Maeda, K. Teramura, D. Lu, T. Takata, N. Saito, Y. Inoue, et al., Characterization of Rh-Cr mixed-oxide nanoparticles dispersed on (Ga 1-xZnx)(N1-xOx) as a cocatalyst for visible-light-driven overall water splitting, J. Phys. Chem. B. 110 (2006) 13753–13758. doi:10.1021/jp061829o.

[175] K. Maeda, K. Teramura, D. Lu, T. Takata, N. Saito, Y. Inoue, et al., Photocatalyst releasing

hydrogen from water., Nature. 440 (2006) 295. doi:10.1038/440295a.

[176] J. Nowotny, C.C. Sorrell, T. Bak, L.R. Sheppard, Solar-hydrogen: Unresolved problems in solid-state science, Sol. Energy. 78 (2005) 593–602. doi:10.1016/j.solener.2005.01.008.

[177] A. Kudo, Y. Miseki, Heterogeneous photocatalyst materials for water splitting., Chem. Soc. Rev. 38 (2009) 253–278. doi:10.1039/b800489g.

[178] F. Jiao, H. Frei, Nanostructured manganese oxide clusters supported on mesoporous silica as efficient oxygen-evolving catalysts, Chem. Commun. 46 (2010) 2920. doi:10.1039/b921820c.

[179] C.-H. Kuo, W. Li, L. Pahalagedara, A.M. El-Sawy, D. Kriz, N. Genz, et al., Understanding the Role of Gold Nanoparticles in Enhancing the Catalytic Activity of Manganese Oxides in Water Oxidation Reactions, Angew. Chemie Int. Ed. 54 (2015) 2345–2350. doi:10.1002/anie.201407783.

[180] K. Maeda, A. Xiong, T. Yoshinaga, T. Ikeda, N. Sakamoto, T. Hisatomi, et al., Photocatalytic overall water splitting promoted by two different cocatalysts for Hydrogen and Oxygen evolution under visible light, Angew. Chemie - Int. Ed. 49 (2010) 4096–4099. doi:10.1002/anie.201001259.

[181] S.K. Mohapatra, S.E. John, S. Banerjee, M. Misra, Water photooxidation by smooth and ultrathin a-Fe2O3 nanotube arrays, Chem. Mater. 21 (2009) 3048–3055. doi:10.1021/cm8030208.

[182] C. Jorand Sartoretti, B.D. Alexander, R. Solarska, I. a Rutkowska, J. Augustynski, R. Cerny, Photoelectrochemical oxidation of water at transparent ferric oxide film electrodes., J. Phys. Chem. B. 109 (2005) 13685–13692. doi:10.1021/jp051546g.

[183] T.-Y. Yang, H.-Y. Kang, K. Jin, S. Park, J.-H. Lee, U. Sim, et al., An iron oxide photoanode with hierarchical nanostructure for efficient water oxidation, J. Mater. Chem. A. 2 (2014) 2297. doi:10.1039/c3ta13830e.

[184] Y. Cong, M. Chen, T. Xu, Y. Zhang, Q. Wang, Tantalum and aluminum co-doped iron oxide as a robust photocatalyst for water oxidation, Appl. Catal. B Environ. 147 (2014) 733–740. doi:10.1016/j.apcatb.2013.10.009.